Photonic Integrated Circuits Challenges & Solutions: Homogenization, Polarization Management and Coupling

Parya Samadian

Thesis submitted to the Faculty of Graduate and Postdoctoral Studies in partial fulfillment for the requirements for the degree of

Master of Applied Science

School of Electrical Engineering and Computer Science

University of Ottawa

Ottawa, Canada

Abstract

In recent years much effort has been carried out to make integrated photonics a wide-spread technology to be exploited in current optical communication industry. It is hoped by substituting microelectronics by photonic chips and keeping the light carried by optical fibers in light domain for further processing, the cost and speed of communications will be vastly improved. Although this transition is challenging in various aspects, here in this thesis some of these issues are discussed and addressed.

In this thesis firstly the limitations of current simulation tools for analysis of wide range of photonic devices is pointed out. Structures based on photonic crystals are taken into consideration at this point which because of finely detailed structures have shown to be challenging to be analyzed by conventional tools. In this regard three different common structures based on photonic crystals in both resonant and non-resonant regimes have been considered: lamellar gratings, metamaterials for Lüneburg lens and Bragg gratings in a LC-DFB laser. For each structure, an analytical method or homogenization approach is proposed which is claimed to be faster for analysis of such components than numerical methods. Comparisons of the results with conventional numerical methods prove accuracies of each approach.

Furthermore, fiber-to-chip coupling and polarization management are discussed as other important issues in the field of integrated photonics. Concerning polarization management, stepped waveguide approach will be introduced as the most promising approach for SOI and III-V substrates and designs based on this structure reported in literature are reproduced and inaccuracies are pointed out and corrected accordingly. Also regarding fiber-to-chip coupling, a critical appraisal of the most recent proposed structures for edge coupling will be offered and the results will be reproduced by simulation tools. At the end, based on detailed comparisons, the most encouraging approach with low insertion loss and easy fabrication steps is introduced and novel platform for easy butt coupling single mode fibers to the coupler structure is proposed.

Acknowledgments

I would first like to express my most sincere gratitude to Prof. Trevor Hall, my supervisor, for his continuous support in all aspects in the past two years to make a peaceful environment for me to study and also to experience a new life style in Ottawa and furthermore for his motivation and passion in research work and also his immense knowledge which was very inspiring for me to continue my educational path. Also I want to thank all my colleagues and friends in PTLab at University of Ottawa for their intellectual and friendly supports. And last but not least I want to thank my family that although faraway, their warm encouragement and support have always been with me.

.

Table of Contents

List of Tables

List of Figures

List of Abbreviations

BPM	Beam Propagation Method
CMOS	Complementary Metal-Oxide-Semiconductor
DFB	Distributed FeedBack
EME	Eigen Mode Expansion
FDM	Finite Difference Mode
FDTD	Finite-Difference Time-Domain
FEM	Finite Element Method
FP	Fabry-Perot
LC-DFB	Laterally-Coupled Distributed Feed-Back
MFD	Mode Field Diameter
PDM	Polarization division Multiplexing
PIC	Photonic Integrate Circuit
PR	Polarization Rotator
PSR	Polarization Rotator and Splitter
PWE	Plane Wave Expansion
QD	Quantum dot
S matrix	Scattering Matrix
SMF	Single Mode Fiber
SOI	Silicon On Isolator
TE	Transverse Electric
TM	Transverse Magnetic
T matrix	Transmission Matrix
WDM	Wavelength Division Multiplexing
1D	1 Dimensional
2D	2 Dimensional
3D	3 Dimensional

Chapter 1. Introduction

1.1. Background

Exploiting optical beams carried by optical fibers for data transmission as a substitute for radio waves or electrical current has attracted much attention since the development of laser in 1960s providing a source for coherent light [1]. High data rate capabilities, low loss, electrical isolation and noise rejection are just a few of the significant features that make fiber optics an ideal and promising technology for communication networks [2].

Currently the optical fibers used in telecom networks are only installed in the backbone and backhaul to transport the information in the form of light, whereas copper wire is still commonly used for last mile links and also electronic circuitry is used for signal processing and routing in network nodes. In other words, the network equipment mostly consists of electronic circuitry and it is solely the transportation of data that is in the optical domain. In the network nodes, the optical signal is converted to electrical signal for routing and further processing and then converted back into light to be transferred towards the next node via optical fibers. These opto-electronic conversions result in an increase to the delay of the whole transport network which wastes the advantage of high band-width capabilities that optical fibers have to offer.

An optical fiber is capable of transmitting light having a range of wavelengths (~1530-1570 nm) with little attenuation across large distances. If one were able to utilize this complete wavelength range for the modulation of a signal, the data rate that would be obtained is more than 4 Tb/s. However this cannot be reached directly considering current technologies since conventional electronics are not capable of operating at this high speed and also the copper wires are unable to operate at frequencies higher than several 10 GHz.

Since nowadays the demand for data traffic is increasing exponentially, the necessity of exploiting components capable of operating at high data rates becomes more significant.

To enable fiber optic technologies with higher speeds up to terabit per second, it is desired that the signal remains in the optical domain throughout the path. For this purpose laser beams can be manipulated for signal processing, however it requires various optical components such as lenses, prisms, mirrors, detectors and electro-optic modulators. This equipment must be suspended on a vibration-proof mount and would occupy a table with dimensions of tens of feet which are not convenient for practical applications. Therefore the concept of miniaturized optical circuits has emerged to replace the conventional integrated electronic circuits [3,4]. In 1969 Miller and Marcatili proposed to build a photonic integrated circuit (PIC) consisting of different optical components on a planar substrate [5,6]. These basic elements can be also used as building blocks to realize more complicated photonic devices performing variety of functions.

Although integrating multiple optical components in a single chip is desired, it is just recently that the proper conditions for the development of such technology have emerged due to the tremendous enhancements in the fabrication and processing technologies. Microtechnology, which involves fabricating components with dimensions on the order of micrometers, has evolved into nanotechnology, in which features in nanometer are routinely produced which encouraged the development of new integrated photonic devices.

Developing promising methods towards processing and miniaturization of integrated photonic devices has attracted attention of industry [7]. Initially technologies based on alloys of III-V compounds, such as Gallium Arsenide (GaAs) or Indium Phosphyde (InP) had a stronger impact in the development of PICs. These materials due to their direct energy bandgap at telecom wavelengths can be exploited as light emitting sources. [8,9]. Also the energy bandgap of the III–V (or II–VI) ternary or quaternary compounds can be changed by altering the relative concentrations of elements resulting in changing the wavelength of emitted light which is very significant feature in PICs.

Similar to what happened to silicon microelectronics, photonic technology will find mass market only if high volume manufacturing can be realized with low cost. As a result the main goal in III-V photonics research has been to find a technology in which a variety of photonic devices can be easily fabricated in a generic process. This concept is well-

known in silicon microelectronics because the developed integration process supports the integration of basic building blocks to build more complex circuits by simple interconnection. However this process is new in III-V photonics and is initially a difficult task which leads to a high cost technology development. So the idea of using silicon and its mature platform for developing integrated photonics has emerged by the increasing demand for low-cost mass-production [10].

Silicon photonics based on the silicon-on-insulator (SOI) platform has proved to be a promising technology in optoelectronic integration for communication, computing and sensing [11-13]. Initially SOI substrates, having a buried SiO2 layer were applied to the microelectronics industry to reduce the parasitic capacitances in the electronic integrated circuits [14]. In silicon photonics this silicon's high quality native oxide offers a significant advantage. Soref et al. was the first to exploit the high index contrast between silicon and SiO2 in such platforms to enable high confinement of light and hence dense circuit integration [15].In a conventional planar waveguide light is confined in the core (Silicon) which has a higher refractive index than the cladding material (Silica). However in silicon photonics the high index contrast in the waveguides causes scattering at the core-cladding boundary imperfections [16]. Different methods have been developed to minimize this effect [17-20].

Photonic crystals on the other hand use a different mechanism for guiding light [21-23]. The photonic devices that are comprised of photonic crystals having dielectric materials arranged periodically can confine light by an effect different from the total internal reflection which is called the photonic bandgap effect. Propagation of light in periodic devices faces multiple scattering and interference at the dielectric lattice which develops frequency bands where the propagation of wave is allowed and bandgaps where waves with certain wavelengths are not able to propagate as a result of destructive interference. One-dimensional photonic crystals used in multi-layer stack or Bragg mirrors have been studied since 1920th, however the scientific interest in photonic crystals started in1970's when Bykov proposed generalization of 1D-stacks to higher dimensions (24). The practical applications of photonic crystal devices that were able to work at optical

wavelength emerged only 20 years later due to the improvements in the nanoscale fabrication technology.

Although integrated photonics has gained a great deal of interest from the industry and academia and has progressed tremendously since its emergence, this technology has a long way to go to compete with its counterparts in well-established and standardized micro and nanoelectronic industry. Some of the obstacles in this area will be discussed here.

1.2. Concerns in Integrated Photonic

1.2.1. Simulation Tools

For designing different integrated photonic devices, it is essential to be able to analyze how optical waves behave in these small structures. In such devices the wave-like character of the light plays an important role as all the dimensions are on the order of the wavelength. Analytical tools such as coupled mode theory, perturbation theory, transfer matrix, etc. can be applied to study behavior of light in very simple devices, but not in integrated level. As soon as the structures become more complicated such as when the device dimensions becomes smaller than wavelength or the coupling between different components becomes non-linear the mentioned analytical techniques lose their accuracy and one needs more accurate numerical analysis of the behavior of the light.

Professional commercial tools for integrated photonics industry are a new concept and even 20 years ago most R&D laboratories tended to use their own codes for each particular application. Although photonic simulation tools have improved a lot since then and currently there is a good choice of tools available to researchers, photonic modeling still faces considerable challenges. Although a wide variety of technologies have been developed for integrated photonics, there exists no simulation tool or algorithm capable of dealing with all sorts of photonics circuits.

Various algorithms have been developed for modeling photonic devices. Although for a modeling method the ideal algorithm must meet the specific criteria. These aspects include speed of calculation, memory usage, tolerable index contrast, reflections,

boundary conditions and etc. [27] Here we quickly review the most common algorithms used for numerical analysis of integrated photonic devices.

BPM

The Beam Propagation Method, BPM, is the first commonly used technique [28]. In BPM the propagation of light is assumed to be approximately only in one single direction. Examples of such devices are Mach-Zehnder interferometers. By making this approximation one can transform the equations needed to be solved from a boundary value problem to an initial value problem. The idea in algorithms used in this method is to omit the fast varying term in the wave equation, exp (jβz) and solve the slower varying field. This approximation works for the case of waveguide components such as tapers having modest index contrast, but it goes inaccurate dealing with silicon photonics devices having high index contrast and tight light confinement. Opti-BPM tool is used in our laboratory for BPM analysis.

EME

Another method used in variety of algorithms is Eigenmode Expansion Method, EME [29]. In this technique the electromagnetic field is decomposed to sum of local eigenmodes. The principle of this method can be summarized in the following wave equations [27]:

$$E(x,y,z) = \sum_m E_m(x,y).(c_m^+.e^{i\beta_m z} + c_m^-.e^{-i\beta_m z})$$
$$H(x,y,z) = \sum_m H_m(x,y).(c_m^+.e^{i\beta_m z} + c_m^-.e^{-i\beta_m z})$$

Equation 1.1

Where $E_m(x,y)$ and β_m are respectively the electric field profile and propagation constant of the m^{th} mode and c_m^+ and c_m^- are the mode amplitudes in +z and –z directions. Using Equation 1.1, a scattering matrix as below can be developed for the component under study:

$$\begin{bmatrix} v_{lhs} \\ v_{rhs} \end{bmatrix} = S \begin{bmatrix} u_{lhs} \\ u_{rhs} \end{bmatrix}$$

Equation 1.2

Where the V matrix represents the vector amplitudes entering the component in the left and right side and U matrix represents amplitude of the vectors exiting the component.
On the advantages of this method we can note that it is fully bidirectional algorithm and also fully vectorial, which helps making no approximation on the light polarization. This method can be considered a rigorous method using Maxwell's equation with the main approximation of finite number of modes. And also it can be used for modeling periodic structures in a fast way since the scattering matrix for just one period can be used to find the behavior for whole device. FimmWave and FimmProp included in Photon Design Suite are used in this thesis for EME analysis.

FDTD

On the contrary to the methods we reviewed earlier, there are certain types of photonic devices that the simulation tools for modeling them must be able to deal with light propagation in all directions in the plane. In such structures light is reflected back in the direction it originally came from or propagates perpendicularly to the original direction as a result of travelling around a tight bend. Photonic crystals and cylindrical micro-cavities are examples of such structures. In this case, one can consider the time dependence of the fields and simulate the full time-dependent Maxwell's equations. This technique is called Finite Difference Time Domain (FDTD) method [30].
FDTD is a powerful tool that solves Maxwell's equations discretized in time and space in a brute-force way. Theoretically algorithms based on FTDT are capable of modeling any kind of structures although the simulating based on FDTD is still a process of trial-and-error for many cases. FTDT can be very time-consuming and also it demands enormous amount of computation power and memory when various coupling and resonance issues have to be taken into account in case of structures comprised of putting together several devices. CrystalWave included in Photon Design Suite is used in our laboratory for FTDT analysis.

FEM

FEM , Finite Element Method, is a mathematical method capable of finding field solutions operating in frequency domain [31]. Although aforementioned methods use rectangular grids for numerical analysis such that nodes are placed at intersections of

orthogonal straight lines, the symmetric generality of FEM allows dividing the region to elements with different shapes such as triangular, curvilinear, etc. This feature enables this method to deal with structures with curved boundaries or arbitrary cross sections. It is also suitable for problems having large index difference and steep field variations; The features which were missing in other numerical methods. In this thesis Comsol Multiphysics has been used for FEM analysis of photonic structures.

1.2.2. Polarization Management

Polarization management in photonic integrated circuits is an essential issue in order to achieve a high-speed and long-haul optical communications [26]. Although polarization of light would not harm the quality of signal in the traditional long distance data transmission through optical fibers, in case of on-chip photonics polarization of light plays an important role. In this technology, using high refractive index materials such as silicon in the waveguides with a rectangular shape generates a large birefringence for TE and TM modes. In other words the two polarizations modes will behave differently and will not couple to each other unless the symmetry of the structure is broken.

Since most of the structures in integrated photonics, including on-chip lasers, modulators and filters only operate at a certain polarization, TE and TM modes should be separated and one of the them needs to be converted to another. As a result polarization of light in integrated photonics must be closely controlled which forces a further study of integrated components to separate, combine or convert polarizations. Furthermore polarization of light can be considered as an additional degree of freedom and hence polarization management methods besides traditional techniques such as dual polarization modulation can be applied to double the data rate of transmission.

Although various on-chip polarization manipulation devices including polarization convertors and polarization splitters have been demonstrated, there are still different aspects to improve their performance. The key parameters in polarization management devices are the insertion loss, extinction ratio, bandwidth and fabrication tolerance and footprint.

1.2.3. Fiber-to-Chip Coupling

The concept of integrated photonics involves transmission of light through optical fibers and also signal processing and routing using photonic chips to keep the data in the optical domain throughout the path. However the injection of light from optical fibers to planar waveguides and also moving the optical signal between planar waveguides on different substrates is not a negligible issue.

Conventional singlemode SOI strip waveguides have 220 nm thickness and 500nm width. While the standard singlemode fibers (SMF) have a much larger size compared to nanophotonic SOI waveguides with a core diameter size of about 8 um. This high difference in the dimensions of these light carriers results in a huge mismatch between the optical modes and hence a huge amount of power will obviously be lost when trying to move the signal directly from fiber to the waveguide.

The common wavelength range used for photonics is the C band, which spans from 1530nm to 1565nm. In case of operation at 1550nm, the middle of the C band, a typical single mode optical fiber confines the optical signal to a 10.43 um mode field diameter (MFD) [25]. Typically a direct butt coupling of a singlemode fiber to a nanophotonic waveguide leads to more than 20dB coupling loss. The high loss definitely is not tolerable in photonics systems since it is directly linked with performances such as the signaling rate, the link reach, the receiver sensitivity, etc. Therefore many various solutions for the coupling problem have been proposed and implemented.

1.3. Objectives

In this thesis it is aimed to address and study several bottlenecks in integrated photonics field. The issues concerned here are polarization management in PICs, the coupling of fiber to photonic chip and also the numerical methods used to model and simulate photonic devices as discussed earlier.

In case of numerical methods, specific structures based on photonic crystals in different regimes have been considered with particular applications. These structures have proved that conventional numerical methods are not appropriate for their simulations; they are either too slow or not accurate enough. In these thesis analytical approaches is proposed

in order to homogenize the nano-structured device which not only leads to accurate results but also offers a high analysis speed.

Also on polarization management, it is aimed to discuss most recent and popular approaches from a critical perspective and validate the proposed structures by reproducing the simulations using different tools and at the end emendate where the reported models are not correct.

On the fiber-to-chip coupling front, an optimized approach to coupling is desired which offers low loss as well as easy fabrication. A critical appraisal is required for reported structures in literature to be able to come up with an efficient and promising method.

1.4. Organization of the Thesis

To achieve the above mentioned objectives the thesis is structured as below:

Chapter 1 introduces integrated photonics as an advancing field to replace current micro-electronics industry. It also points out some of the main concerns and obstacles in this field of research that this thesis is going to tackle with.

Chapter 2 gives an introduction to photonic crystals and their significant properties and also their different regions of operation, resonant and non-resonant regime. Then the non-resonant region is considered and studying light propagation in two different applications using 1D and 2D photonic crystals is taken into account. Considering complexity of the structures to be modeled with simulation tools different analytical approaches are proposed for each specific structure with particular application. For the case of lamellar gratings in vertical coupling applications, the plane wave expansion method is extended to take account for this application. The results are compared to the results from Kronig-Penny analytical method developed for this structure to ensure validity. Also in this chapter metamaterials used in Lüneburg Lens are considered as a 2D photonic crystal to study. A robust homogenization method based on band diagram calculation is developed to release the need for complicated and time consuming 3D numerical analysis. The results are compared to 3D numerical analysis from Crystal Wave which shows a good agreement.

Chapter 3 on the other hand deals with structures comprised of photonic crystals near resonance. LC-DFB lasers are taken into consideration as an example of such structures. Bragg resonance in this structure is described by detail and coupled mode theory is introduced as an analytical approach to study behavior light in such structures. Although reflections at each junction and large device lengths make complications in numerical simulations of these devices, a homogenization method is proposed to accurately estimate coupling coefficient and resonance frequency of these semiconductor lasers using Matlab coding. Results are compared with the results obtained from EME simulations using FimmWave which shows a good agreement.

Chapter 4 deals with different approaches to polarization management in integrated photonics. Firstly different polarization modes are introduced and then birefringence and its effect on light polarization of planar waveguides are described. The solution to this issue and the idea behind that is discussed. The most promising approach which offers high efficiency and very small device dimensions is introduced to be a single section stepped- waveguide. EME simulations validate the functionality of the structure. Different devices based on this structure reported on InP substrates including polarization convertors and polarization splitter and rotators (PSR) are taken into consideration for validation. Aside from critical appraisal of the methods, reproducing simulations reveals some inaccuracies in the reported literature which are corrected here.

Chapter 5 focuses on fiber-to-chip coupling issue in integrated photonics. At the beginning the problem is discussed thoroughly and different approaches to solve this matter presented in literature and the theory behind them is introduced. By comparison of different approaches, edge coupling will be considered as the more promising method. Then new enhancements in this field will be reviewed along with reproduction of results reported using simulation tools. Besides a critical appraisal of the methods with best performances, an specific structure is introduced as the most promising approach and a novel platform for exploiting the structure in communication systems is suggested which not only promises a reasonable insertion loss for both polarizations but also is easy to fabricate and implement.

Chapter 6 at the end summarizes the significant points discussed in the thesis and states the main findings and recommends further perspectives.

1.5. Original Contributions

This thesis is aimed to contribute to advancement of integrated photonics industry by both original contributions and critical appraisal of literature. These contributions include:

1. A novel analytical approach for analyzing lamellar gratings in vertical coupling applications. In this method, plane wave expansion method is extended to take account for light excitement from outside of the device. This technique offers a simple, quick and yet accurate modeling of light behavior in such structures.

2. A novel analytical approach for homogenization of 2D metamaterials in planar Lüneburg lens applications. Here corrections in 2D band structure calculations will replace conventional 3D band structure calculations which offers much faster and yet accurate modeling of such devices.

3. A novel analytical approach to homogenization of photonic crystals near resonance for the case of Bragg gratings used in LC-DFB lasers. This method release the need for time and memory consuming numerical simulations using commercial tools and uses simple Matlab coding. Using this technique the resonance frequency and coupling coefficient of the device can be estimated with negligible errors.

4. A critical analysis of polarization management approaches in literature. Reported results are reproduced to validate the accuracy. Furthermore corrections have been made in case of imprecise claims.

5. A critical analysis of coupling approaches for the case of fiber to chip coupling. Reported results are reproduced to validate the accuracy and finding the most

promising structure. A novel platform for a highly efficient edge coupler device is proposed.

Following publications related to this thesis were published:

1. P. Samadian, T. J. Hall, 'Homogenization of nanostructure waveguides in resoanace and non-resonance regimes', Photonics North, Ottawa, June 2015 (to appear)
2. P. Samadian, T. J. Hall, ' Performance Analysis of polarization transformation waveguide structures for planar light circuits', NUSOD, Taipei, September 2015 (to appear)
3. P. Samadian, T. J. Hall, ' Cylindrical Talbot effect in tapered MMIs',(drafted)

Chapter 2. Homogenization in Non-Resonance

2.1. Introduction

Since their appearance, photonic crystals have attracted much attention and have been applied to enhance many photonic devices. However due to their complex structure, researchers have been looking for methods to summarize their properties to a simplified format for computational convenience. In the current chapter we will review extraordinary properties of photonic crystals comprehensively. Also new methods for homogenization of 1D lamellar gratings and 2D metamaterials as common applications of photonic crystals in silicon photonics are proposed. These new approaches offer methods to relief from complex calculations of such structures, which are sufficiently rigorous and can be applied to wide range of designs.

2.2. Photonic crystals and Bloch-Floquet Theorem

A crystal is a periodic arrangement of macroscopic media with differing dielectric constants, repeated in space by a pattern called crystal lattice. Photonic Crystals (PC) are periodically structured electromagnetic media which present periodic refractive index to the light propagating through them. Based on the crystal and geometry parameters, these structures will have different conduction properties, each suitable for different applications.

Three different kinds of photonic crystals are defined depending on the axes in which there is periodicity or asymmetry. If periodicity is just along one axis we have 1-dimensional photonic crystal such as lamellar gratings which are the simplest kind of photonic crystals to analyze. Then we have photonic crystals with periodicities in 2 and 3 axes, respectively 2-dimensioanl and 3-dimensional photonic crystals that are more complicated to analyze light propagation through them.

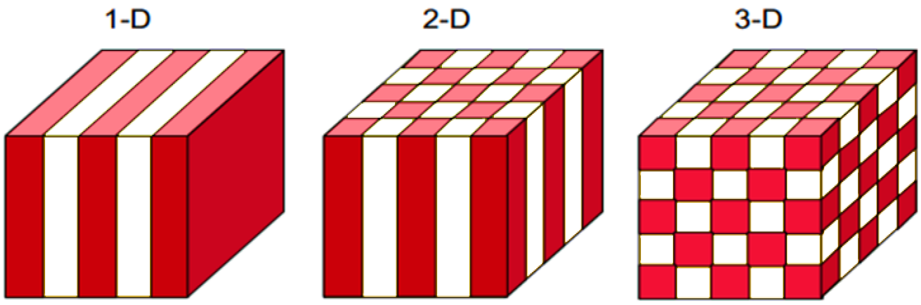

Fig. 2.1. Schematic of 1-deminesional, 2-dimensional and 3-dimentional photonic crystals.

Lord Rayleigh did the first studies on propagation of electromagnetic waves in periodic media in 1887 [32]. In his research reflective properties of a crystalline mineral with periodic “twinning” planes was studied which corresponds to a one-dimensional photonic crystal. Through his investigations he observed a narrow band gap preventing propagation of light with some wavelengths through the planes. Since then multilayer films attracted much attention until 100 years later Yablonovitch [33] and John [34] in 1987 introduced concepts of photonic band gaps in two and three dimensions. The studies to describe structures with band gap for electromagnetic waves were followed by many developments in photonic crystal’s theory, fabrication, and also applications mostly in integrated photonics and fiber optics.

Bloch-Floquet theorem governs over light propagation in photonic crystals. This theory was first introduced by Floquet in 1883 [35]. In 1929, Bloch [36] applied this theory to solid-state physics to study electrons on a potentially periodic lattice. This description rules over to any kind of wave in a periodic medium, thus is adapted to apply to light propagation in photonic crystals.

Assuming one-dimensional photonic crystal as the simplest structure, it presents periodic modulation of refractive index only in one direction and is homogeneous in other directions. In such structure $n(z) = n(z + \Lambda) = n(z + m\,\Lambda)$, Λ being the lattice constant and m is an integer, as shown in Fig. 2.2.

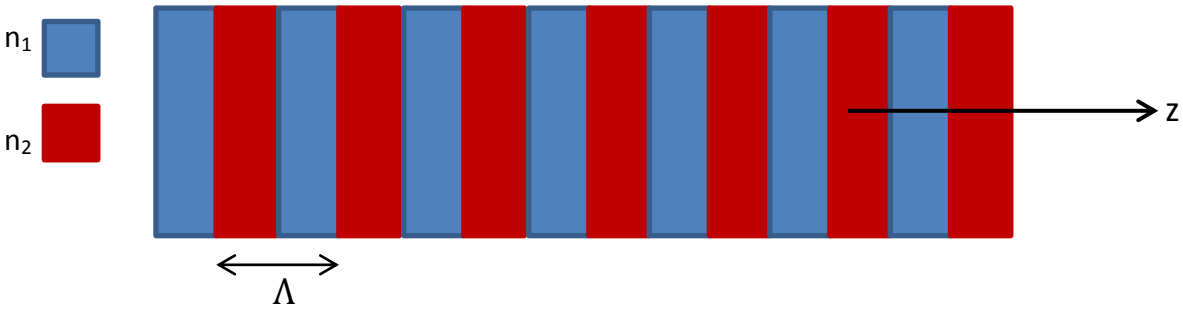

Fig. 2.2. Schematic of a 1D photonic crystal realized by modulation of refractive index in one direction.

According to Bloch-Floquet theorem, Maxwell's equations solutions for such structure are in the form of plane waves propagating along z modulated by a function, $U_\xi(z)$, which is periodic with the same period as lattice constant,

$$E_\xi(z) = E_0 e^{i\xi z} U_\xi(z)$$

Equation 2.1

ξ being the Bloch wave number in z direction which is equal to:

$$\xi = \frac{2\pi}{\lambda}$$

Equation 2.2

The optical frequency of the wave,ω, and ξ are related by dispersion relation as below:

$$\omega = \xi \frac{c}{n_z}$$

Equation 2.3

Where c is the speed of light and n_z is the refractive index of the medium at point z along propagation direction.

A significant consequence of the Bloch theorem is that because of the periodicity of the wave solutions by period Λ, in frequency regime the eigen modes with wavenumber ξ and ξ +m2π/ Λ are identical and based on Equation 2.3 so are the optical frequencies, $\omega(\xi) = \omega(\xi + 2\pi m/\Lambda)$. This means the dispersion diagram for this structure is periodic where reciprocal vector of the lattice, 2π/ Λ, is the period. Typically the essential properties of photonic crystal is derived from only one period, $-\pi/\Lambda < \xi < \pi/\Lambda$, called the first Brillouin zone.

In case of a constant refractive index along z direction the wave number and optical frequency will have a linear relation. Mirroring all the dispersion curves into the first Brillouin zone, Fig.2.3.a is achieved with straight lines crossing each other at the boundaries of the zone. This is the dispersion curve corresponding to a homogenous medium.

As shown in Fig.2.3.b, when a refractive index contrast is introduced in propagation direction z, the dispersion curve folds. In this case, the propagating light is diffracted continuously at each junction of altering refractive index. This diffracted light from forward propagating light ($\xi = \pi/\Lambda$) will couple to counter propagating light ($\xi = -\pi/\Lambda$) at Brillouin zone boundaries or at the center. This coupling results in splitting the state into two other states at frequencies ω_1 and ω_2. As a result there will be no states that exist between these frequencies and the so called "photonic band gap" will open in the dispersion diagram. The width of the band gap directly relates to the index contract of multi-layer medium.

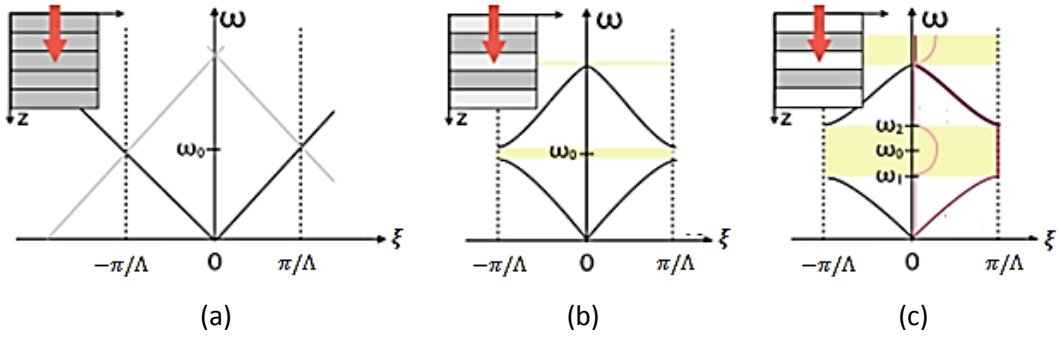

Fig. 2.3. Dispersion curves corresponding to photonic crystals with different index contrasts. (a) a constant refractive index along the propagation direction; the dispersion curve consists of straight lines, b) with index contrast introduced to the structure; different modes of propagation starting to couple to each other at boundaries and the center, resulting in folding the bands and opening a bandgap, (c) the index contrast is increased; the band gap increases as well.

The dispersion curves derived from Bloch-Floquet theorem reveals significant features in photonic crystals. As can be observed in Fig.2.3, for some specific wavelength there is a linear relation with optical frequency just as there is for homogenous mediums. Hence for a medium with periodic refractive index with a certain lattice constant, if one obtains appropriate wavelength where the operating state coincides with linear section of the curve, propagating light will happen without any scattering. Fig.2.4 well illustrates light

propagation in this regime. In this case, as light propagates through the medium reflection of light will happen at each junction. However, since reflected lights are out of phase, they will have a destructive interference and cancel each other and that is how the light will propagate only in forward direction, although slightly attenuated along the structure.

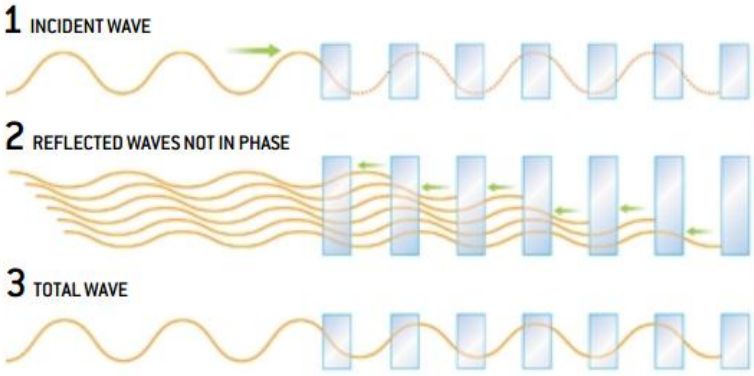

Fig. 2.4. (1) A wave incident at a wavelength outside the band gap, (2) the wave reflected at each period are out of phase and cancel each other, (3) The total wave propagates through the material with a slight attenuation, (Copyright Scientific American 2001, reproduced with permission from reference [37])

To be able to operate at this regime and use propagation of light with no scattering through photonic crystals, one must use propagating light with wavelengths much larger than the crystal lattices. This amount has been calculated to be $\Lambda < \frac{\lambda}{2}$. That is why this regime is called "sub-wavelength domain".

Currently, developments in lithography technology allow manufacturing structures with sub-wavelength lattice constants and producing "artificial media" or "Metamaterials". Metametials are photonic crystals operating at long wavelength limit and are typically used to develop materials having arbitrary refractive indices using the effective medium theory [38]. Analyzing light propagation in metamaterials will be discussed later in this chapter.

On the other hand, if an electromagnetic wave is propagating along a photonic crystal and the wavelength falls into the band gap region, resonance will take place. In such case the reflected light waves at each layer junction will be in phase and make a constructive interference. These waves combine with the propagating light and produce a standing wave. Fig.2.5 indicates this phenomenon. This means any forward propagating wave

having a wavelength in the band gap, will cause a backward propagating wave which based on coupled mode theory (will be discussed later) their energy will be exchanged along the structure leading to having no light travelling through the material. Photonic crystals in this regime will act as a perfect lossless insulator of light which can be applied to many uses such as nano-scopic lasers, higher capacity optical fibers and different photonic integrated circuit devices. Light propagation in this regime will be further discussed in next chapter.

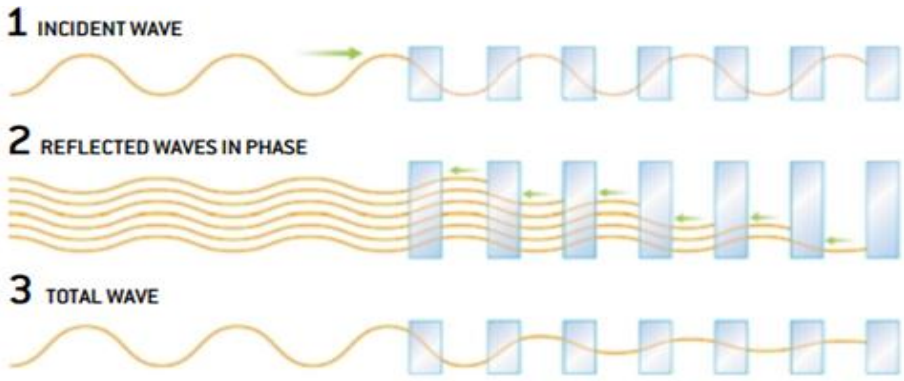

Fig. 2.5. (1) A wave incident at a wavelength inside the band gap, (2) the reflected waves at each period are in phase and combine with the incident wave and make a standing wave, (3) the wave cannot propagate through the structure. (Copyright Scientific American 2001, reproduced with permission from reference [37])

Different operational regions of a photonic crystal are summarized in Fig.2.6. This diagram shows how by having a constant wavelength, operation regimes can be altered by changing the lattice constant of the photonic crystal. Where Λ is chosen relatively smaller than $\frac{\lambda}{2}$, the media is in sub-wavelength region and no resonance will happen. However having a lattice with Λ comparable to $\frac{\lambda}{2}$ the structure will operate at resonant regime.

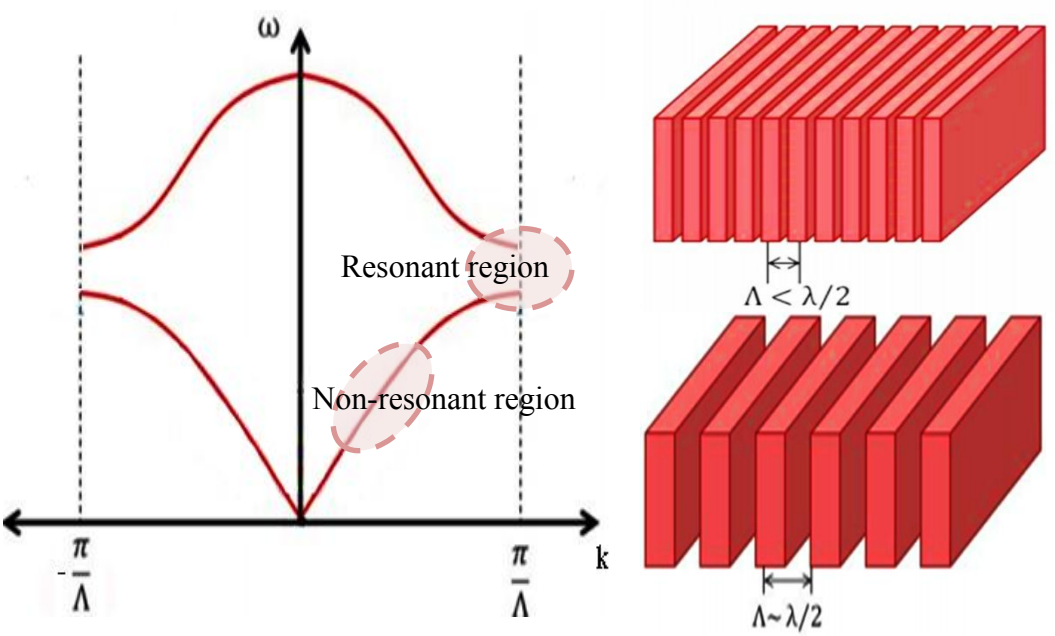

Fig. 2.6. The first Brillouin zone of a 1-D photonic crystal, having two main regimes; resonant region for gratings with ($\Lambda \sim \lambda/2$) and non-resonant region for gratings with ($\Lambda < \lambda/2$).

Having discussed the basics of photonic crystals and its different operational states, following we study light propagation in 1D lamellar gratings and 2D metamaterials. Homogenization methods also will be proposed to summarize properties of such photonic crystals and simplify their analysis and computations.

2.3. Homogenization of 1D lamellar gratings

ID photonic crystals in sub-wavelength domain, presenting periodicity in one direction have been applied to many applications among which grating couplers are good examples. In such components, while the fibers are mounted nearly perpendicular to the chip surface, optical gratings are exploited in order to diffract the out of plane light propagation from optical fibers to in-plane light waves in on-chip waveguides or vice versa.

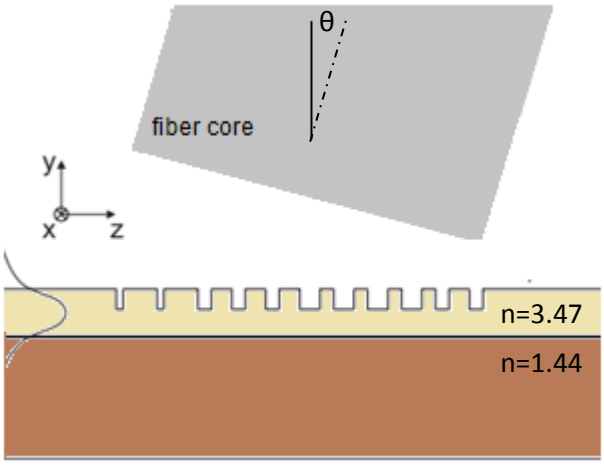

Fig. 2.7. Schematic of an optical fiber coupling to an on-chip waveguide using 1D photonic crystal as a grating coupler.

Although 1D photonic crystal slab waveguides and lamellar gratings are formally identical but their analysis differs by perspective. The analysis of lamellar gratings considers excitation of a plane-wave from exterior incident at an angle to the normal of the grating plane. Lamellar grating is treated as of infinite extent so as not to break its perfect periodic symmetry in the plane. Whereas the analysis of 1D photonic crystal slab waveguides considers the modes of the grating structure propagating in the grating plane. Therefore that oblique incidence in the grating perspective is not equivalent to the end-fire launch of a waveguide grating mode in the photonic crystal slab geometry.

In order to design such structures, it is necessary to analyze light propagation through the specific crystal and find the permitted frequencies and calculate the field distribution in the crystal for any frequency of light. Band diagram stores this important information for photonic crystals. As a result we need to derive the band diagram of the device presenting the relation between the Bloch wave numbers and frequencies of the propagating light for the 1D gratings. Plane Wave Expansion (PWE) method is a conventional means to derive this relation for photonic crystals. PWE is a numerical technique to solve the Maxwell's equations by transferring it to an eigenvector- eigenvalue problem using Fourier series expansions of the field components. The achieved eigenvalues give the band diagram and the eigenvectors can be plugged back into the Fourier expansion to find the field distribution at each frequency.

Here we discuss an extension to this method to calculate the band diagram of lamella gratings having an out of plane incident light by an angle to the normal of the wafer. This technique will help to understand the reflection and transmission of external waves at surface of a lamella grating, yielding to a homogenization method summarizing behaviors of such structures.

2.3.1. Plane Wave Expansion Method

Consider a plane wave incident at an angle θ to the normal of a deep lamellar dielectric grating with period Λ as illustrated in fFig.2.8. In this periodic medium a piecewise binary modulation of the refractive index is assumed such that within each period there are two intervals of width d_1 and d_2 of refractive index n_1 , n_2 respectively where $d_1+d_2= \Lambda$. In general, the reflected and transmitted fields will consist of a sum of multiple plane waves comprising the diffraction orders.

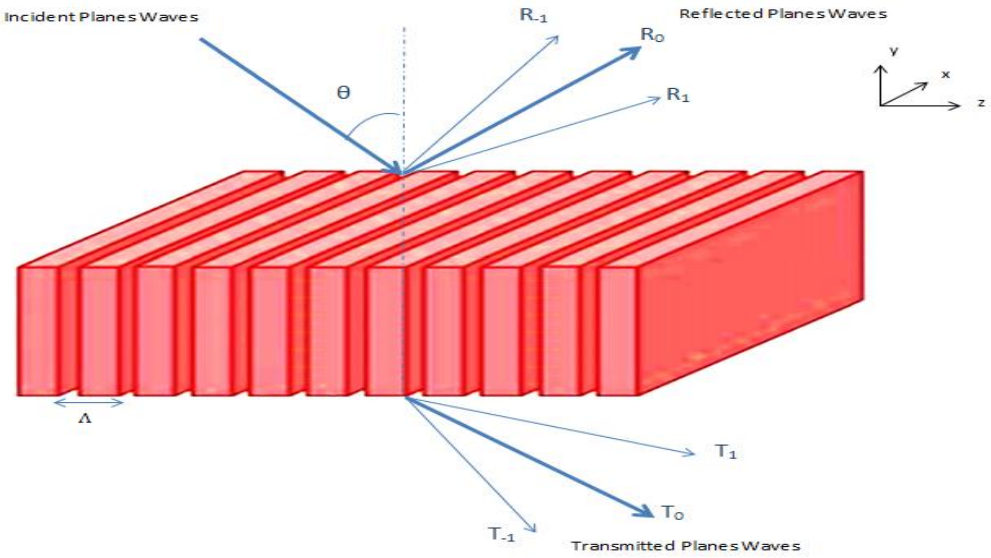

Fig. 2.8. Schematic of an out-of-plane wave incident to a 1D lamellar gratings; the reflected and transmitted fields consist of the sum of multiple plane waves comprising the diffraction orders.

The directions of propagation of these diffraction orders is simply determined by adding a multiple of the grating wave vector K, to the transverse component (z- direction) of the incident wave vector, κ_0:

$$\kappa_p = \kappa_0 + pK$$

Equation 2.4

Where

$$K = \frac{2\pi}{\Lambda}$$

Equation 2.5

The longitudinal component of the wave-vector, β_p (y-direction) is determined by the requirement that the plane wave must satisfy the Helmholtz equation in the ambient medium.

$$\beta_p^2 + \kappa_p^2 = n_0^2 k_0^2$$

Equation 2.6

Thus,

$$\beta_p = \pm\sqrt{n_0^2 k_0^2 - \kappa_p^2} \qquad \kappa_p^2 \le n_0^2 k_0^2$$

$$\beta_p = \pm i\gamma_p = \pm i\sqrt{n_0^2 k_0^2 - \kappa_p^2} \qquad \kappa_p^2 \le n_0^2 k_0^2$$

Equation 2.7

Where

$$k_0 = \frac{2\pi}{\lambda_0}$$

Equation 2.8

where λ_0 is the vacuum wavelength. Mentioned relations can be illustrated in Fig.2.9.

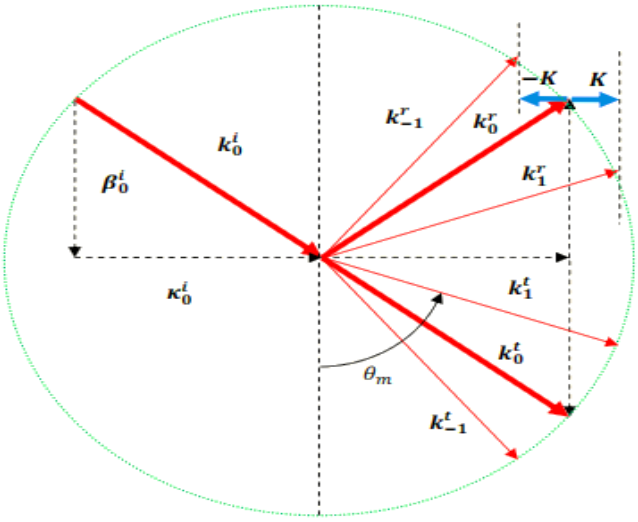

Fig. 2.9. An illustration of the wave vectors of the incident and diffracted plane waves. The transverse component of the wave vectors of diffraction orders can be found by adding multiples of grating wave vector, K, to the transverse component of incident wave vector, κ_0.

Referring to Fig.2.9, the relation between transverse components of diffracted waves can be rewritten as:

$$n_0 k_0 \sin(\theta_m) = n_0 k_0 \sin(\theta_0) + mK$$

Equation 2.9

which is equivalent to the well-known grating equation:

$$\sin(\theta_m) = \sin(\theta_0) + m\frac{\lambda}{\Lambda} \quad , \quad \lambda = \frac{1}{n_0}\lambda_0$$

Equation 2.10

The equation implies that the angle corresponding to diffracted plane waves only depend on the period of the grating. However, it is necessary to solve for the internal fields to determine the amplitudes of the diffraction orders which also depend on the details of the grating structure. In this regard, PWE method will be used to derive the band structure of the lamellar gratings having light incident by an angle to the normal of the surface.

Starting with Maxwell's equations for electric and magnetic fields, we have:

$$\nabla \times \boldsymbol{H} = \frac{\partial \boldsymbol{D}}{\partial t}$$
$$\nabla \times \boldsymbol{E} = -\frac{\partial \boldsymbol{B}}{\partial t}$$

Equation 2.11

Where the material constitutive equations are:

$$\boldsymbol{B} = \mu_0 \boldsymbol{H}$$
$$\boldsymbol{D} = \varepsilon \varepsilon_0 \boldsymbol{E}$$

Equation 2.12

and applying an implicit $exp(-i\omega t)$ time dependence to convert to frequency domain we obtain:

$$\nabla \times \boldsymbol{H} = -i\omega\varepsilon\varepsilon_0 \boldsymbol{E}$$
$$\nabla \times \boldsymbol{E} = i\omega\mu_0 \boldsymbol{H}$$

Equation 2.13

For simplicity, it is assumed that there is no variation in the x-direction and the propagation direction of the incident light is constrained to a plane through the optical axis perpendicular to the x −direction,

$$\frac{\partial \boldsymbol{F}}{\partial x} = 0$$

Equation 2.14

F being the plane wave under consideration. From here on, distinct problems for TE & TM polarization may be distinguished. For TE modes, field components may be written as below:

$$\boldsymbol{E} = \begin{bmatrix} E_x \\ 0 \\ 0 \end{bmatrix} \quad \boldsymbol{H} = \begin{bmatrix} 0 \\ H_y \\ H_z \end{bmatrix}$$

Equation 2.15

Hence we will obtain Maxwell's equations as:

$$\frac{\partial H_z}{\partial y} - \frac{\partial H_y}{\partial z} = -i\omega\varepsilon\varepsilon_0 E_x$$
$$\frac{\partial E_x}{\partial z} = i\omega\mu_0 H_y$$
$$-\frac{\partial E_x}{\partial y} = i\omega\mu_0 H_z$$

Equation 2.16

which implies:

$$\frac{\partial^2 E_x}{\partial y^2} + \frac{\partial^2 E_x}{\partial z^2} + \omega^2 \mu_0 \varepsilon_0 \varepsilon E_x = 0$$

Equation 2.17

Same procedure is applied for TM modes with field components of:

$$\boldsymbol{E} = \begin{bmatrix} 0 \\ E_y \\ E_z \end{bmatrix} \quad \boldsymbol{H} = \begin{bmatrix} H_x \\ 0 \\ 0 \end{bmatrix}$$

Equation 2.18

And equation below is obtained:

$$\frac{\partial}{\partial y}\left[\frac{1}{\varepsilon}\frac{\partial H_x}{\partial y}\right] + \frac{\partial}{\partial z}\left[\frac{1}{\varepsilon}\frac{\partial H_x}{\partial z}\right] + \frac{\omega^2}{c^2} H_x = 0$$

Equation 2.19

where:

$$c = \frac{1}{\sqrt{\varepsilon_0 \mu_0}}$$

Equation 2.20

Since the propagation medium has a relative permittivity $\varepsilon = n^2(z)$ which is periodic with period Λ, it may be expanded as a Fourier series:

$$\varepsilon = \sum_{p=-\infty,\infty} \varepsilon_p exp(ipKz)$$

Equation 2.21

where:

$$\varepsilon_p = \frac{1}{\Lambda} \int_{-\Lambda/2}^{\Lambda/2} \varepsilon(z) exp(-ipKz) dz$$

Equation 2.22

In a lamellar grating the refractive index distribution is as follows:

$$n^2(x) = \begin{cases} n_1^2 & 0 \le |x| \le d_1 \\ n_2^2 & d_1 < |x| \le d_1 + d_2 \end{cases}$$

Equation 2.23

In such structure the Fourier coefficients are derived as:

$$\varepsilon_0 = f n_1^2 + (1-f) n_2^2$$

$$\varepsilon_p = f(n_1^2 - n_2^2) \frac{sin(\pi p f)}{(\pi p f)}$$

Equation 2.24

Where

$$f = \frac{d_1}{d_1 + d_2}$$

Equation 2.25

Also in case of $\boldsymbol{\eta} = \frac{\mathbf{1}}{\mathbf{n^2(z)}}$ we have:

$$\eta_0 = f \frac{1}{n_1^2} + (1-f) \frac{1}{n_2^2}$$

$$\eta_p = f \left(\frac{1}{n_1^2} - \frac{1}{n_2^2} \right) \frac{sin(\pi p f)}{(\pi p f)}$$

Equation 2.26

Considering the Fourier expansion of the periodic medium, the periodic part of the Bloch mode may also be similarly expanded:

$$u(z) = \sum_{p=-\infty,\infty} a_p exp(ipKz)$$

Equation 2.27

where:

$$a_p = \frac{1}{\Lambda} \int_{-\Lambda/2}^{\Lambda/2} u(z) exp(-ipKz) dx$$

Equation 2.28

Therefore the Bloch mode is represented by the set of plane waves defined as:

$$F(x,z) = exp(i\xi z) \left[\sum_{p=-\infty,\infty} a_p exp(ipKz) \right] exp\left(\pm i\beta_p y\right)$$

Equation 2.29

Where ξ is the Bloch wave vector. It is clear that the electromagnetic boundary conditions will enforce equality of the transverse components of the plane waves at the interfaces between the interior and exterior regions. Thus the Bloch wave number is set by the angle of incidence of the incident plane wave.

$$\xi = \kappa_0$$

Equation 2.30

Therefore the equation for Bloch modes is re-written as Equation 2.31. Note that in consistence with relations mentioned earlier, the transverse wavenumber is dependent to the grating wavenumber:

$$F(x,z) = \left[\sum_{p=-\infty,\infty} a_p exp\left(ik_p z\right) \right] exp\left(\pm i\beta_p y\right) \quad , \qquad k_p = k_0 + pK$$

Equation 2.31

Assigning a positive sign for longitudinal component of incident and transmitted orders and a negative sign for the reflected orders we have forms for each set of plane wave:

$F^{(i)}(x,z) = \exp[i(k_0 z - \beta_0 y)]$, The incident field

$F^{(r)}(x,z) = \sum_{p=-\infty,\infty} b_p \exp\left[i\left(k_p z - \beta_p y\right)\right]$, The reflected field

$F^{(r)}(x,z) = \sum_{p=-\infty,\infty} b_p \exp\left[i\left(k_p z + \beta_p y\right)\right]$, The transmitted field

Equation 2.32

Hence, in all regions the plane waves will have partial waves with transverse variation governed by partial waves of the form:

$$a_p(x)\exp[i\left(\kappa_p z\right)]$$

Equation 2.31

Substituting the derived Fourier expansions into the Maxwell's equation obtained for TE modes and equating terms with the same spatial frequencies yields:

$$\frac{\partial^2 E_x}{\partial y^2} + \frac{\partial^2 E_x}{\partial z^2} + \frac{\omega^2}{c^2}\varepsilon E_x = 0$$

$$(\boldsymbol{\kappa^2} + \beta^2\mathbf{I})\boldsymbol{a} = \frac{\omega^2}{c^2}\mathbf{E}\boldsymbol{a}$$

Equation 2.32

Also for TM modes we have:

$$\frac{\partial^2}{\partial y^2}H_x + \varepsilon\,\frac{\partial}{\partial z}\left[\frac{1}{\varepsilon}\frac{\partial}{\partial z}H_x\right] + \frac{\omega^2}{c^2}\varepsilon H_x = 0$$

$$(\mathbf{E\kappa H\kappa} + \beta^2\mathbf{I})\boldsymbol{a} = \frac{\omega^2}{c^2}\mathbf{E}\boldsymbol{a}$$

Equation 2.33

Equations 2.32 and 2.33 are the desired eigenvector-eigenvalue problems, solving which will result in deriving the dispersion diagram of the lamella grating. For both TE & TM modes, problem have been reduced to generalized eigenvector problems with ω^2/c^2 nominally playing the role of an eigenvalue parameterized by the wavevector $\left(\kappa_p, \beta_p\right)$.

Here β being the longitudinal wavevector, $\beta^2\mathbf{I}$ is the action of $-i\frac{\partial^2}{\partial y^2}$ in real space. Also matrix $\boldsymbol{\kappa}$ is a diagonal matrix of $k_p = \xi + pK$, which $\boldsymbol{\kappa^2}$ will be the action of $-i\frac{\partial^2}{\partial z^2}$. Also vector "a" is defined as:

$$\boldsymbol{a} = \begin{bmatrix} \vdots \\ a_{-2} \\ a_{-1} \\ a_0 \\ a_1 \\ a_2 \\ \vdots \end{bmatrix}$$

Equation 2.34

Which is an infinite dimensional column vector of Fourier coefficients describing the Bloch mode in the partial wave basis. And finally matrices E and H defined as

$$\mathbf{E} = \begin{bmatrix} \ddots & \ddots & \ddots & \ddots & \ddots & \ddots & \ddots \\ \ddots & \varepsilon_0 & \varepsilon_{-1} & \varepsilon_{-2} & \varepsilon_{-3} & \varepsilon_{-4} & \ddots \\ \ddots & \varepsilon_1 & \varepsilon_0 & \varepsilon_{-1} & \varepsilon_{-2} & \varepsilon_{-3} & \ddots \\ \ddots & \varepsilon_2 & \varepsilon_1 & \varepsilon_0 & \varepsilon_{-1} & \varepsilon_{-2} & \ddots \\ \ddots & \varepsilon_3 & \varepsilon_2 & \varepsilon_1 & \varepsilon_0 & \varepsilon_{-1} & \ddots \\ \ddots & \varepsilon_4 & \varepsilon_3 & \varepsilon_2 & \varepsilon_1 & \varepsilon_0 & \ddots \\ \ddots & \ddots & \ddots & \ddots & \ddots & \ddots & \ddots \end{bmatrix}$$

$$\mathbf{H} = \begin{bmatrix} \ddots & \ddots & \ddots & \ddots & \ddots & \ddots & \ddots \\ \ddots & \eta_0 & \eta_{-1} & \eta_{-2} & \eta_{-3} & \eta_{-4} & \ddots \\ \ddots & \eta_1 & \eta_0 & \eta_{-1} & \eta_{-2} & \eta_{-3} & \ddots \\ \ddots & \eta_2 & \eta_1 & \eta_0 & \eta_{-1} & \eta_{-2} & \ddots \\ \ddots & \eta_3 & \eta_2 & \eta_1 & \eta_0 & \eta_{-1} & \ddots \\ \ddots & \eta_4 & \eta_3 & \eta_2 & \eta_1 & \eta_0 & \ddots \\ \ddots & \ddots & \ddots & \ddots & \ddots & \ddots & \ddots \end{bmatrix}$$

Equation 2.35

are infinite dimensional Toeplitz matrices representing the reciprocal space with the partial wave basis which perform the action of multiplication by $\varepsilon(z)$ and $\eta(z) = \varepsilon^{-1}(z)$ respectively in real space.

Building defined matrices and solving the eigenvector-eigenvalue problem the dispersion diagram in terms of relation between frequencies and transverse wavevector will be obtained.

To validate this extended numerical method an analytical approach is applied. The Kronig-Penny model of 1D gratings introduced by Mishra [39] is an alternative approach to PWE. Following we discuss how this method will be compatible to the problem of lamellar gratings. We first drive the Kronig-penny model dispersion equation from

transfer matrix of a grating period and then compare the resulted dispersion curves to the ones obtained from PWE method.

2.3.2. Kronig-Penney model

The propagating Bloch modes of lamellar gratings may be found from the quasi-analytical Kronig-Penny model [39]. This method treats a 1D piece-wise periodic structure of infinite extent and constructs the Bloch modes from plane waves components that solve the wave equation in the uniform regions. To adapt this model to the structure under study in this chapter which is a lamellar grating with an angled out of plane incident light, additional components must be included in the wave-vector of the component plane waves to allow for oblique incidence when the structure extends infinitely in other directions. This addition to the original model allows comparison eigenvectors and eigenvalues returned with the result from PWE method. A single interface of different refractive indices in a lamellar grating can be illustrated as Fig.2.10:

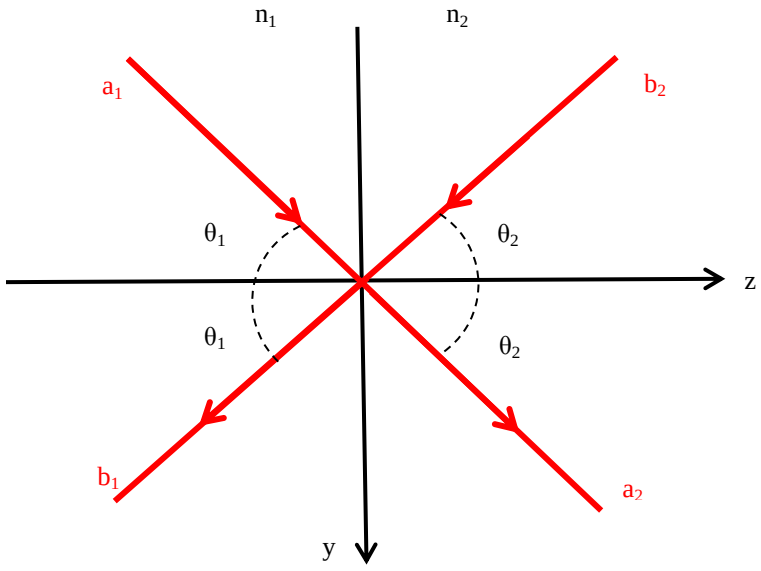

Fig. 2.10. Incident plane waves at an interface with different refractive indices at each side.

The relation between fields in two sides can be simply defined as:

$$\begin{bmatrix} a_2 \\ b_2 \end{bmatrix} = \Gamma \begin{bmatrix} a_1 \\ b_1 \end{bmatrix}$$

Equation 2.36

Where Γ is the transmission matrix for this interface. According to the Bloch-Floquet theory in this 1D periodic medium, wave propagation will be of form of

$$E_\xi(z,y) = E_\xi(z)e^{i\xi z}e^{i\beta y}$$

Equation 2.37

Where ξ is the Bloch wavenumber and $E_\xi(x)$ is a periodic function with period Λ ,

$$E_\xi(x+\Lambda) = E_\xi(x)$$

Equation 2.38

This periodic condition simply yields to:

$$\begin{bmatrix} a_2 \\ b_2 \end{bmatrix} = e^{i\xi\Lambda}\begin{bmatrix} a_1 \\ b_1 \end{bmatrix}$$

Equation 2.39

Which brings us to the eigenvector-eigenvalue problem to be able to solve for the band structure;

$$\Gamma\begin{bmatrix} a_1 \\ b_1 \end{bmatrix} = e^{i\xi\Lambda}\begin{bmatrix} a_1 \\ b_1 \end{bmatrix}$$

Equation 2.40

The transmission matrix Γ relating filed distribution in two sides of the interface with a grating period of $d_1+d_2= \Lambda$ is defined by Yeh and Yariv [40]:

$$\Gamma = \begin{bmatrix} \left[\cos(\kappa_1 d_1) + i\frac{1}{2}(\chi^{-1}+\chi)\sin(\kappa_1 d_1)\right]\exp(i\,\kappa_2 d_2) & -i\frac{1}{2}(\chi^{-1}-\chi)\sin(\kappa_1 d_1)\exp(i\,\kappa_2 d_2) \\ -i\frac{1}{2}(\chi^{-1}-\chi)\sin(\kappa_1 d_1)\exp(-i\,\kappa_2 d_2) & \left[\cos(\kappa_1 d_1) - i\frac{1}{2}(\chi^{-1}+\chi)\sin(\kappa_1 d_1)\right]\exp(-i\,\kappa_2 d_2) \end{bmatrix}$$

Equation 2.41

Where

$$\chi = \eta\frac{\kappa_1}{\kappa_2} \quad , \quad \eta = \begin{cases} 1 & TE \\ \frac{n_2^2}{n_1^2} & TM \end{cases}$$

Equation 2.42

And as mentioned earlier, according to Helmholtz equation in the ambient medium:

$$\kappa_1 = \sqrt{n_1^2 k_0^2 - {\beta_1}^2}$$

$$\kappa_2 = \sqrt{n_2^2 k_0^2 - {\beta_2}^2}$$

Equation 2.43

Where $\kappa_1$and κ_2 are the transverse wave vectors and $\beta_1$and $\beta_2$are longitudinal wavevectors in two sides of the interface. Obtaining the trace of the matrix we have:

$$\frac{1}{2}Tr(\Gamma) = \cos(\kappa_1 d_1)\cos(\kappa_2 d_2) + \frac{1}{2}(\chi^{-1} + \chi)\sin(\kappa_1 d_1)\sin(\kappa_2 d_2)$$

Equation 2.44

considering that the trace of a matrix is equal to the sum of its eigen values, in our case $e^{i\xi\Lambda}$ is the eigen value of the matrix. Hence:

$$Tr(\Gamma) = 2\cos(\xi\Lambda)$$

Equation 2.45

Therefore one obtains the Kronig-Penney model dispersion equation:

$$\cos(\xi\Lambda) = \cos(k_1 d_1)\cos(k_2 d_2) + \frac{1}{2}(\chi^{-1} + \chi)\sin(k_1 d_1)\sin(k_2 d_2)$$

Equation 2.46

For both TE and TM modes, by solving the equation above for different ξ s in different frequencies, the dispersion diagram is achieved.

Fig.2.11 provides a comparison between dispersion curves obtained by solving the eigenvector-eigenvalue problems derived from the discussed two methods for TE modes. The blue lines show the dispersion bands achieved from analytical Kronig-Penney method for a lamellar gratings of pitch 250 nm and fill factor of 0.5. Also in the same figure the red signs on the diagram show the data obtained by Plane Wave Expansion method. As can be observed a good agreement is achieved verifying the extended PWE method for lamellar gratings with out-of-plane light incident.

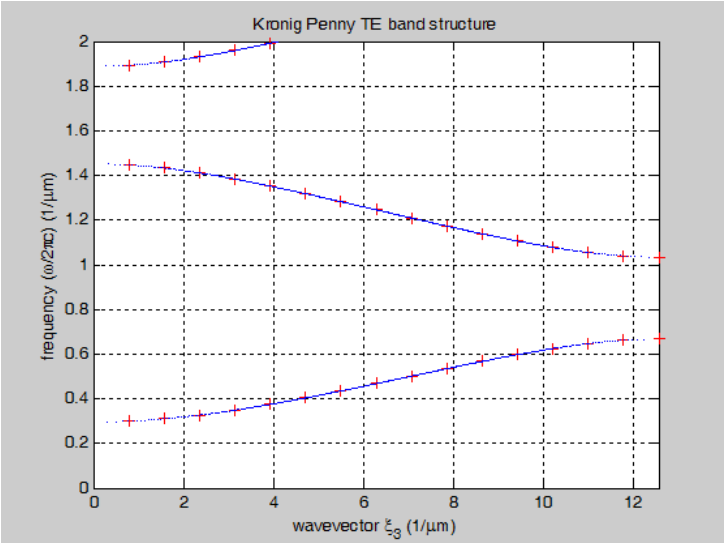

Fig. 2.11. Comparison between dispersion curves calculated by PWE and Kronig-Penney method for TE modes in a lamellar grating with a pitch of 250 nm and fill factor of 0.5. Blue lines correspond the data obtained from Kronig-Penney method and red signs correspond to data obtained from PWE.

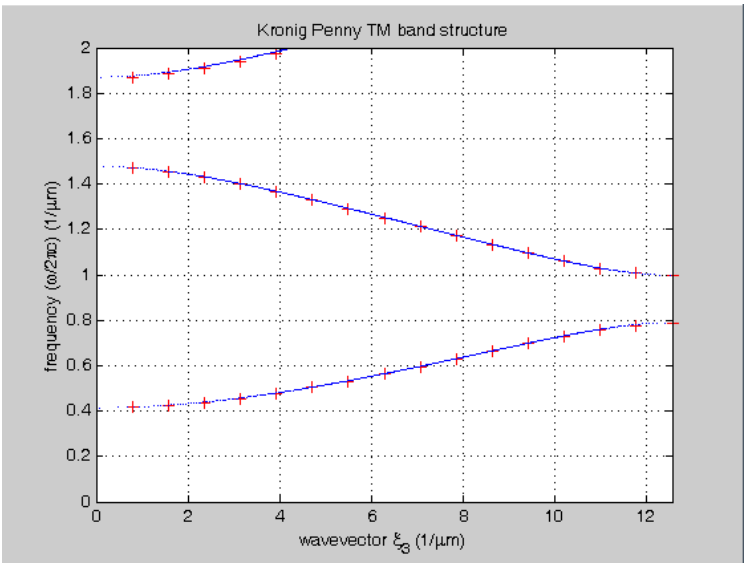

Fig. 2.12. Comparison between dispersion curves calculated by PWE and Kronig-Penney method for TM modes in a lamellar grating with a pitch of 250 nm and fill factor of 0.5. Blue lines correspond the data obtained from Kronig-Penney method and red signs correspond to data obtained from PWE.

The method discussed in this section simplifies analysis of light propagation in lamellar gratings by introducing a simple eigenvector-eigenvalue problem for any kind of design parameters. In the next section we discuss propagation analysis in a 2D metamaterial and

introduce a new approach towards homogenization of such structures to summarize their properties to be able to treat them as a homogenous medium.

2.4. Homogenization of 2D Metamaterials

Earlier we discussed different kinds of photonic crystals and their different properties in different regimes, non-resonant and resonant. In non-resonant or sub-wavelength regime, light propagation in the structure will have no scattering and the medium can be considered as a homogenous medium possessing a certain refractive index. Here we will show how this property can bring significant application as refractive index engineering for this kind of structures.

Consider a planar slab waveguide with a solid core as an example. Assuming silicon and silica as materials used for core and substrate respectively and air upper cladding, the structure will compose a 1D asymmetric slab waveguide. Because of the index contrast between core and claddings, light will be confined in the structure in the direction normal to the plane. Here for simplicity we assume that only the fundamental mode is supported in the waveguide. The effective index that the fundamental mode realizes is different from that of the core and the refractive index of the substrate also has an influence on that. Hence this effective refractive index will be somewhere between n_{core} and $n_{substrate}$. This effective index realized by the fundamental mode depends on waveguide parameters such as the thickness and width of the core and the refractive indices of different layers and also the vacuum wavelength. This means by changing waveguide parameters we can adjust the effective refractive index experienced by the fundamental mode. This adjusting can be performed by altering waveguide dimensions or it can be done by introducing nanosturturing to the waveguide.

Imagine patterning the core of slab waveguide, by inclusions of one material within another material as a host. Assuming that the lattice constant is smaller than $\lambda/2$, the sub-wavelength scale nanostructuring will act like a homogenous medium with no scattering of light. In this case the effective index seen by the mode will also depend on the nanostructure parameter. It means by nanostructuring the core, we have increased the degrees of freedom for altering the effective index. Here not only height or refractive

index of the core layer can be changed, also the fill factor of inclusions in host material will be a significant parameter in determining the effective index. This kind of materials called “artificial materials” or “Metamaterials” are used vastly to obtain desired local effective index in standard waveguides or so called “refractive index engineering”.Rodgar M. Walser [41] who used the word “Metamaterials” defines such structures as follows[42]:

“Metamaterials are defined as macroscopic composites having a man-made, three dimensional, periodic cellular architecture designed to produce an optimized combination, not available in nature, of two or more responses to a specific excitation.”

In a metamaterial structure, if the parameters, say the fill factor, changes slowly enough so that the fundamental mode can adapt to the new environment adiabatically and the local effective index can be derived from the dispersion diagram [43,44], a “graded index” structure will be obtained which have many applications in light manipulation such as in imaging and cloaking configurations [45-48], Eaton Lens[49] and Lüneburg Lens[50]. Here we focus on a metamaterial structure that is used to design Lüneburg Lenses. A Lüneburg lens focuses incoming plane waves with arbitrary directions to focal points at the opposite side of the lens which have applications in planar switching of light [50, 51].

Here we consider nanostructuring a SOI slab waveguide by cylindrical inclusions to realize graded index structure for Lüneburg Lens. This pattern is composed of either rods or holes within air or silicon respectively as the host material. It must be noted that in both conditions lattice constant must be chosen sub-wavelength to prevent Bragg scatterings.

In both structures, core patterning resembles a 2D photonic crystal because of periodicity in x and z direction. However, since the holes and rods are not infinite and substrate and upper cladding impose asymmetry to the waveguide, hence the structure must be considered as a 3D photonic crystal and analyzed accordingly. To do that, the 3D band diagram of the photonic crystal is computed by building a 3D unit cell from the 2D unit cell by having the finite rods surrounded by upper and lower claddings of air and silica

respectively [52]. Also in [53] another approach is taken and the effective index is calculated by the reflection and refraction properties in one unit cell. These methods, although rigorous, they require 3D calculation which are time consuming and computationally expensive.

To find a way around going through complex 3D calculations, many researchers have been used effective index method [54-57]. Min Qiu [58] has tried to validate the results obatained by this method by comparing the result with rigorous 3D FTDT outcome. In his report, he has studied a 2D photonic crystal on a heterostructure slab waveguide. Inclusions in this photonic crystal are in shape of holes in all the layers of waveguide (core, upper and lower claddings). In the procedure studied, firstly an unperturbed slab waveguide will be considered and the effective refractive index realized by the fundamental mode will be extracted, n_{eff}. Then the heterostructure slab waveguide will be substituted by a dielectric medium with the calculated refractive index. As a result the structure will reduce to a 2D photonic crystal in a host with refractive index equal to n_{eff}. Assuming infinite height for inclusions the effective index for the media can be calculated by 2D computations.

Qui's method is generally suitable for structures with etched substrates. However in his approach the reduced structure involves a host with effective refractive index and holes with unmodified indices. The treatment given to host and inclusion is not symmetric which restricts the method to inclusions having small perturbations to the host and hence small fill factors. Also the use of unperturbed waveguide to estimate the effective index of the mode limits method applications to low contrast media so that the change in core effective media index had little effect on the effective index of the delocalized mode.

On the other hand, Gao [59] proposes an approach for abstraction the properties of a 2D photonic crystal. In his approach an ad hoc structure for Lüneburg lens is studied which involves cylindrical silicon rods on a square lattice. In this method the effective refractive index of the rods will be calculated using second-order effective medium theory, assuming infinite height for inclusions. Then they incorporate a slab waveguide with calculated n_{eff}, sandwiched between semi-infinite spaces of air above and glass below.

The approach Gao is suggesting is reported to have comparable results to rigorous 3D calculations. However, since they are using the 2D extended effective index theory for lamellar gratings, this approach mainly limits to metamaterials with square lattice.

In the next section a new approach to homogenization of metamaterials, confinement corrected 2D method, will be introduced that not only proposes a fast computation compared to 3D methods, it can also be applied to metamaterial structures with rods or holes on any kind of lattice. The results will be compared to 3D calculations which show a good agreement. Also the approach introduced is rigorous, as the 2D band diagram calculations is used in this method and no approximations is assumed.

2.4.1. Confinement Corrected 2D method

Earlier we discussed how metamaterials can be used for refractive index engineering applicable in different devices such as Lüneburg lens. To be able to find local effective refractive index of metamaterials in such applications, a faster and more rigorous method compared to existing ones is required. This approach must summarize the nanostructure part of the metamaterial and replace it by some effective media in which the larger scale behavior of wave propagation in metamaterial is preserved. In this chapter we discuss a fast and rigorous homogenization method for metamaterials used in Lüneburg lens.

The structure considered here is a 2D lattice in shape of finite-height inclusions of rods or holes in a host of silicon or air, surrounded by air and silica as upper and lower claddings. According to standard SOI technology, a silicon layer of 220 nm was selected. For fabrication easement, the cylindrical shaped atoms were used to realize 2D photonic crystal on a lattice constant of 250 nm which falls into the range for fabrication using deep UV lithography. Based on the type of lattice, different ranges of fill factors can be obtained from silicon rods. The hexagonal lattice offers higher packing densities than other plane lattices. For a hexagonal lattice of pitch p, composed of cylinders of diameter d, the fill factor will be computed as:[60]

$$f = \frac{\pi}{2\sqrt{3}} . \frac{d^2}{p^2} \leq 0.9$$

Equation 2.47

Where this equation will be as below in case of a square lattice:

$$f = \frac{\pi}{4}.\frac{d^2}{p^2} \leq 0.79$$

Equation 2.48

Hence hexagonal lattice providing higher fill factors is more appropriate to be used.

This structure although contains a 2D photonic crystal, since has a finite-height surrounded by upper and lower claddings has an extra asymmetry in y direction and must be analyzed as a 3D structure. For sake of homogenization, cylindrical rods will be assumed infinite initially to be able to use 2D techniques to deal with them. The effective refractive index of the 2D photonic crystal can be derived from the corresponding 2D band diagram. Calculating the corresponding n_{eff}, the nanostructure core of the slab waveguide will be replaced by a homogenous layer with refractive index equal to n_{eff}. Fig.2.13 below well illustrated the procedures taken for homogenization by this method.

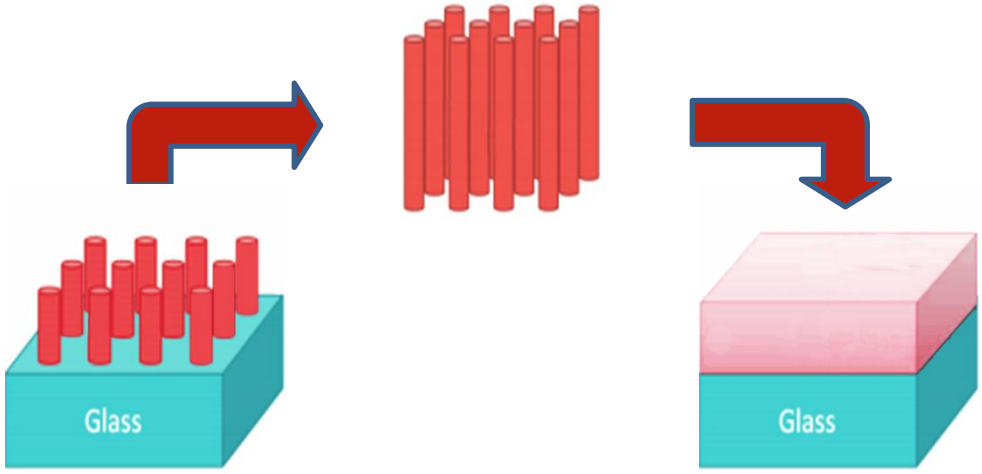

Fig. 2.13. Schematic of the proposed homogenization method; initially cylindrical rods are assumed infinite and the effective refractive index is derived from 2D band diagram, then the nanostructured core will be replaced by a homogenous layer having the calculated effective refractive index.

CrystalWave package of Photon Design Suite was used to achieve the 2D band diagram and hence the effective refractive index corresponding to the structure. First we consider silicon rods having a diameter of 230 nm in an air host. A 2D unit cell of this structure designed in CrystalWave can be seen in Fig.2.14. The $\Gamma MK\Gamma$ path also is defined as in

Fig.2.15 for the selected unit cell. The cross section of the structure is indicated in Fig.2.16.

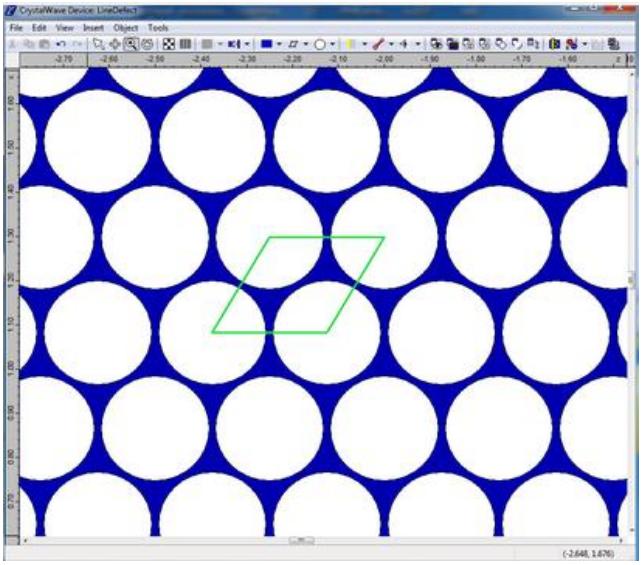

Fig. 2.14. A unit cell for a structure composed of silicon rods of diameter 230 nm mounted in air host on a hexagonal lattice with a lattice constant of 250 nm.

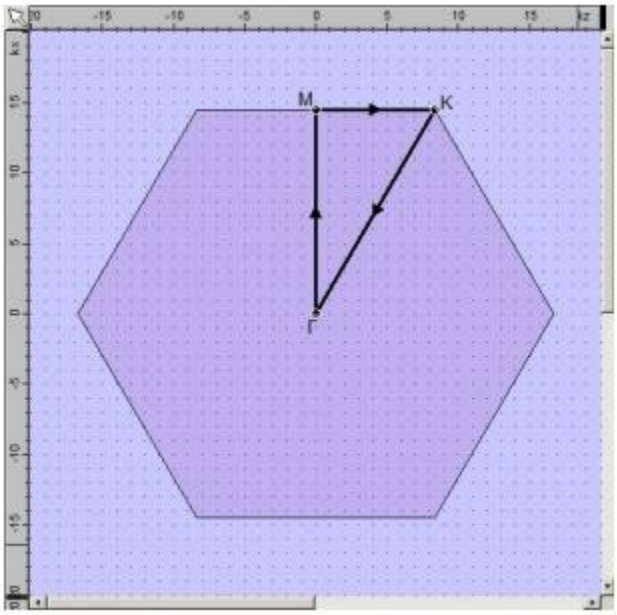

Fig. 2.15. The k-space diagram of the ΓMKΓ path for cell for a structure composed of silicon rods of diameter 230 nm mounted in air host on a hexagonal lattice with a lattice constant of 250 nm.

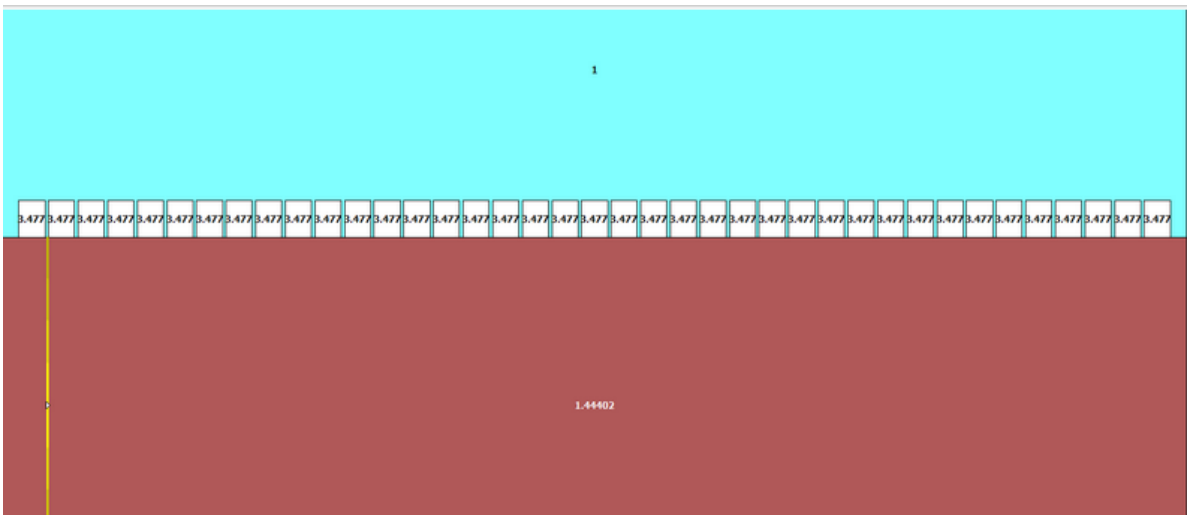

Fig. 2.16. Cross sectional view of the structure; 230 nm silicon rods in air with a lattice constant of 250 nm.

Fig.2.17 is the 2D band diagram for TE modes, calculated by CrystalWave for this structure,

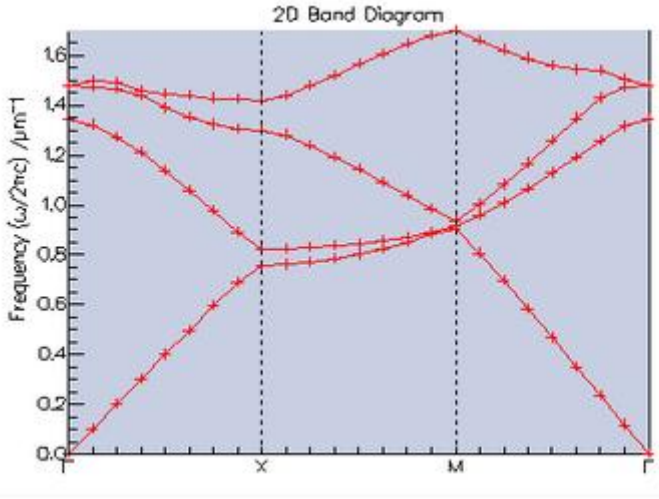

Fig. 2.17. The 2D photonic band diagram for TE polarization for the structure composed of 230 nm silicon rods in air with lattice constant of 250 nm.

As discussed earlier in section 2-2, to have the photonic crystal behaving as a homogenous medium and propagate light with no scattering we have to operate at wavelengths that fall into the lower band near linear section of the band diagram. The operating vacuum wavelength of $\lambda_0 = 1550\,nm$ corresponding to 0.6451 μm^{-1} is of interest in this structure which is slightly deviated from the linear long-wavelength asymptote in calculated band diagram.

For deriving the effective refractive index in the desired wavelength, since reading the n_{eff} from the diagram is not possible for a specific frequency, approximations have been undertaken. In this experiment three nearest point to the desired frequency and corresponding n_{eff}s are found. Then using a cubic spline method, the hypothetical relation between different points is obtained which later on is used to find the fourth point, n_{eff} in wavelength of 1550.

To compare the results from proposed approach to 3D analysis, 3D band solver for 2D structures was used in CrystalWave. This solver considers periodic conditions in the plane having a silicon layer patterned by 2D lattice. Then it replicates the whole structure out of the place to find a 3D unit cell having 3D boundary conditions. However in our case the structure does not have periodicity out of the plane and the tool is making an approximation in this regard. Fig.2.18 is the 3D band diagram calculated by the tool. In this figure red lines correspond to the TE modes that we are interested in this experiment.

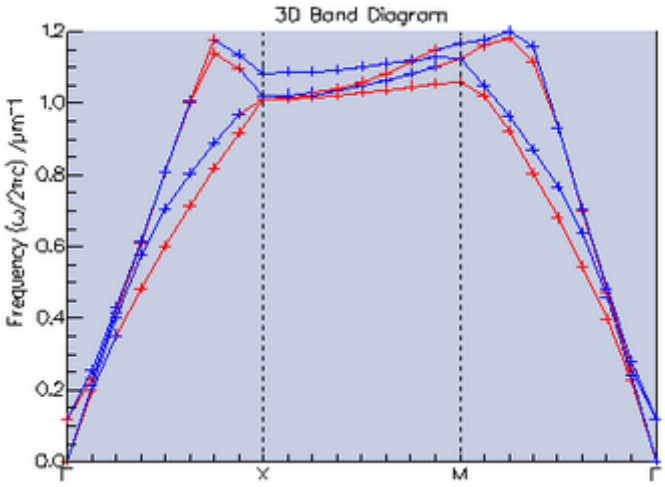

Fig. 2.18. The 3D photonic band diagram for TE polarization (red lines) and TM polarization (blue lines) for a structure composed of 230 nm silicon rods in air with lattice constant of 250 nm.

It must be noted that for sake of light confinement, there will be a limit to the effective refractive indices reached for silicon rods or air holes as inclusions. For air holes the highest effective index would be the refractive index of silicon n_{si}=3.47772 for holes of diameter zero and minimum refractive index would be equal to refractive index of air n_{air}=1. This also is the case for silicon rods in air. However, the effective refractive index of the core cannot be lower than the highest index of the claddings. Having a substrate of

silica, this kind of metamaterial permits diameter of holes to a maximum of 240 nm and diameter of rods to a minimum of 180 nm so that the effective index will remain higher than n_{SiO2}=1.44402. That is why for the case of rods studied here 190 nm is chosen as the minimum diameter of rods to ensure light confinement.

Fig.2.19 represents a comparison between results from 3D calculations and confinement corrected 2D calculations for cylindrical rods in a hexagonal lattice with diameters varying from 190 nm to 220 nm. As can be seen an excellent agreement is achieved (<1.5 % error)

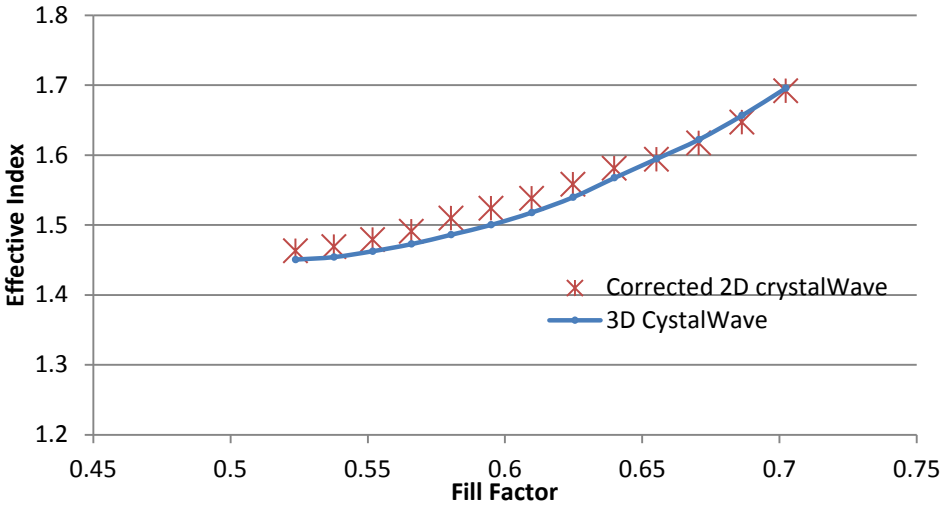

Fig. 2.19. The effective index of the fundamental mode for a structure including silicon cylindrical rods with thickness of 220 nm in air host with hexagonal lattice constant of 250 nm; calculated by corrected 2D method and 3D band solver.

This approach also can be applied to the case of metamaterials composed of holes in a silicon core. Fig.2.20 shows the comparison of the analytical method and 3D numerical method for circular holes of diameter 0 to 220 nm in a silicon host with a lattice constant of 250 nm. In this structure also a good agreement is achieved. (<4 % error) .

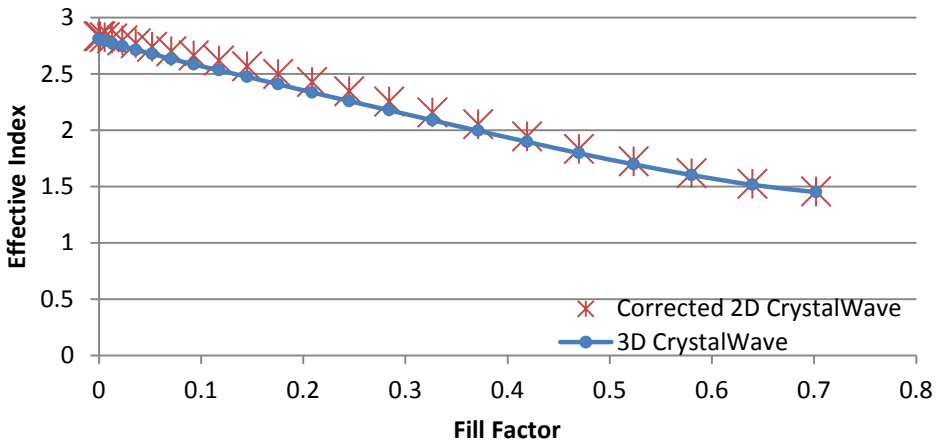

Fig. 2.20. The effective index of the fundamental mode for a structure including cylindrical holes in silicon with 220 nm thickness with hexagonal lattice constant of 250 nm; calculated by corrected 2D method and 3D band solver.

It must be noted that the errors can be considerably reduced by increasing the computational grid resolution in the simulation tool. The settings used here are chosen in a trade-off between time consumption and accuracy.

To indicated validity of the approach for all shapes of holes or cylinders on any kind of lattice, same approach has been taken to compare results for square rods in a square lattice for a core of thickness 300 nm for rods of diameter 170 nm to 210 nm. As it is indicated in Fig.2.21 very good agreement is achieved. (<2 % error)

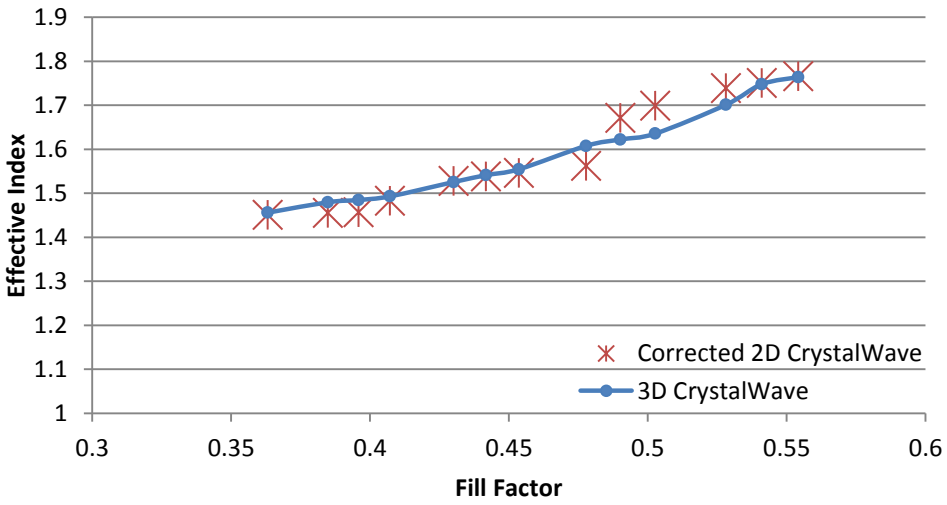

Fig. 2.21. The effective index of the fundamental mode for a structure including square rods with 300 nm thickness in air with square lattice constant of 250 nm; calculated by corrected 2D method and 3D band solver.

2.5. Summary

In this chapter photonic crystals were introduced as semiconductors of optical world presenting frequency band gaps. Different operational regimes of these structures were analyzed and properties and application of each was discussed. 1D lamellar gratings for application in grating couplers and 2D metamaterials for applications in Lüneburg Lenses were introduced as examples of photonic components based on photonic crystals in non-resonant regime.

For case of 1D lamellar gratings an extension to conventional PWE method was proposed to analyze light propagation in such structures when there is an out of plane exterior incident light having an angle to the normal of the surface. This numerical method was verified by an analytical approach, Kronig-Penney, which also was adapted to this specific problem. Comparisons indicate excellent agreement which proves validity of proposed approach.

Also in case of 2D metamaterials, their application in refractive index engineering and specifically in Lüneburg lens was discussed. Due to complex 3D calculations required to analyze the metamaterials used in Lüneburg lens, an abstraction procedure was proposed to reduce the structure to a 2D case and do the analysis in the new condition. This method is rigorous compared to current methods and unlike its counterparts is applicable to any kind of structures with different inclusions and different lattice properties. Results were compared to 3D calculations and good agreement was achieved.

Chapter 3. Homogenization Near Resonance

3.1. Introduction

Earlier we discussed how photonic crystals present a band gap in their dispersion diagram preventing light with some wavelengths passing through and providing standing waves going forward and reflected back continuously. This property of such structures which enables wavelength selectivity is exploited by researchers to many applications including semiconductor lasers called Laterally Coupled Distributed Feedback Lasers (LC-DFB).

Due to the complex structure and large lengths of this semiconductor lasers, numerical methods used to analyze designs and find different properties of the device are rather time consuming. Hence an analytical method is desired to summarize main properties of the device into simpler structure and solve the structure in less time and using less memory resources.

In this chapter first we will discuss the structure of LC-DFB lasers and how they work. Then we will introduce the proposed analytical approach for homogenization of such devices. The analytical results will be compared to numerical ones for verification.

3.2. Structure of Distributed Feedback Lasers

As discussed in chapter 3 photonic crystals prevent waves having wavelengths that fall into their bandgap, from travelling through the medium. W.H. and W.L. Bragg [61] were the first to describe this wavelength filtering property of photonic crystals. The structure proposed by this father and son was composed of parallel layers having alternative refractive indices of n_1 and n_2, making a 1D photonic crystal. Light propagation in such medium, called Bragg gratings, are explained using Huygens's principle. Christian Huygens in 1670 was the first to explain the laws of optics using wave theory. Huygens's principle states that every point on the wavefront of the diffracted lights can be considered as a secondary point source of a spherical wave which

travels in the forward direction with the same speed. Summation of these point sources indicates the overall effect of the diffractive material and in this case, the Bragg gratings.

In such structures at each junction with different refractive indices, propagating light with wavelengths in bandgap region is reflected. This reflection effect will be accumulated by reflection at each period. Constructive or destructive interference of these reflected waves depends on their relative phase which is determined by the relation between the period of modulation and light wavelength. At a particular wavelength, constructive interference of reflected waves will take place and a backward scattering wave is observed. This means any forward propagating wave will produce a backward propagating wave. Along the length of the grating the energy will be exchanged between waves propagating in these two different directions. As a result no light having those specific wavelengths will be able to pass through the medium and will create a standing wave resonating through the gratings.

However the reflected waves of light with other wavelengths are cancelled out as a result of being out of phase and hence those waves will be transmitted along the grating. This results in wavelength selectivity in such structures that only specific wavelength will experience resonance. Based on the dispersion curve (Fig.2.6 in chapter 2) in order to have a resonance at wavelength λ, the pitch of the periodic layers of Bragg gratings must be chosen to be $\Lambda \sim m\lambda/2$, m being an integer. Or in another words a photonic crystal with a period of Λ will experience resonance at wavelengths equal to $\lambda \sim 2\,\Lambda/m$. This means in such structure acquiring those wavelengths we will have operation states at the bandgap regions in different Brillouin zones (base on the value of m).

The wavelength filtering of Bragg gratings has been studied to be exploited in many applications including Distributed Feedback Lasers (DFB). This kind of semiconductor lasers uses Bragg gratings as a laser cavity which only resonates specific wavelengths. The gratings in such lasers reflect back the forward propagating light with particular wavelengths at each abrupt junction and in overall provides a feedback effect exploited for lasing a coherent light.

DFB lasers offer a narrow linewidth and also a great control over the laser wavelength compared to earlier kinds of semiconductor lasers, Fabry-Perots (FP). FP lasers provide the required feedback for lasing using cleaved facets at the end of the laser cavity having an interface between air and semiconductor that is naturally partially reflective. Figure 3.1 is to compare the optical spectrum of these two kinds of semiconductor lasers. As it is clear DFB lasers offer an improvement on spectral purity over those of FP lasers. [62]

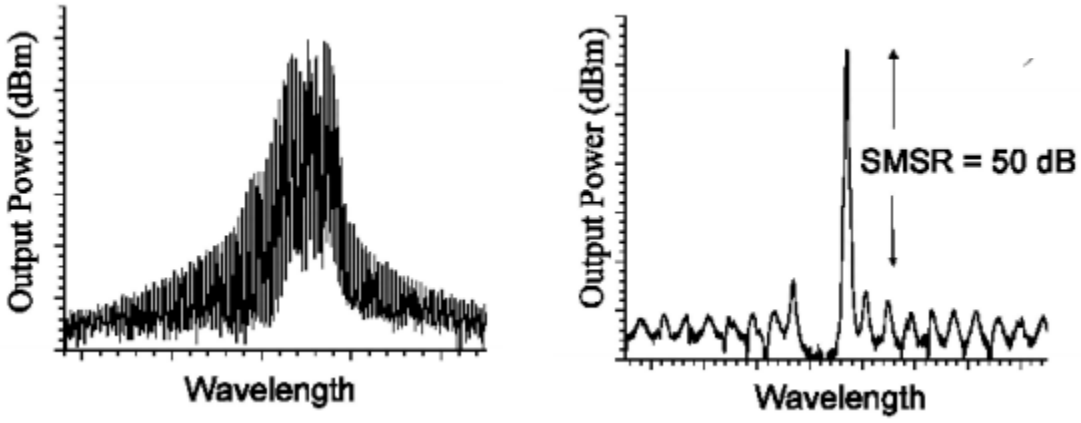

Fig. 3.1. Optical spectrum of a Fabry-Perot laser (left) and a DFB laser (right) [62]

Fig.3.2 shows a schematic of a standard DFB laser. The process for fabrication of a standard DFB laser includes epitaxial growth on the substrate, defining grating using holographic techniques for etching and growing upper claddings. At the end a ridge waveguide is defined on top of the claddings. This fabrication process for the case of FP lasers is reduced to only a single growth and etch step. Therefore the additional fabrication steps required for standard DFB lasers makes DFB lasers less attractive compared to FP structured counterparts.

To overcome the fabrication complexity of DFB lasers, Laterally Coupled Distributed Feedback (LC-DFB) Lasers are introduced. LC-DFB lasers were first fabricated by Miller et al. in the University of Illinois in 1991 [63]. In this structure the epitaxial growth steps is eliminated by incorporating the grating structure to the ridge waveguide itself. In LC-DFB lasers by modulating the width of the ridge waveguide along the light propagation, we therefor are changing the effective refractive index realized by the fundamental mode along the way. Hence the light will experience a Bragg scattering

through the medium. In this case the optical mode will be evanescently coupled to the grating. Fig.3.2 indicates a schematic of both discussed structures.

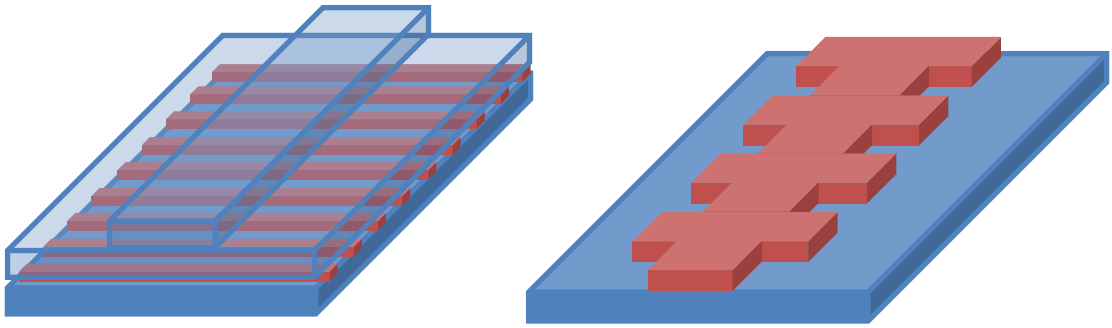

Fig. 3.2. Schematic of a standard DFB laser (left) and a LC-DFB laser (right)

Although LCDFB lasers offer lower fabrication steps but desire smaller feature sizes compared to standard DFB lasers. Nowadays first-order Bragg gratings for applications in DFB lasers can be defined in a standard process using holography in UV lithography. However defining first-order gratings for a LC-DFB laser is not as simple. Gratings used for this kind of laser require stringent specifications. Sidewalls of the gratings in such structures must be sufficiently deep so that the evanescent modes would make a strong coupling, yet smooth and vertical enough to minimize scattering losses. They also must be finely-spaced to make the backward Bragg scattering in the correct wavelength. That is why fabrication of LC-DFBs mostly rely on electron-beam lithography rather than standard optical lithography [63,64]. In electron-beam lithography (e-beam) using special electro-sensitive resists, high resolution gratings can be defined having very precise grating structures. Although this kind of lithography allows great control over grating parameters, this technique is slower and more expensive compared to standard optical lithography which prevents LC-DFBs to be a good substituent for their counterparts. In this chapter we discuss how by facing a trade-off between optical loss and easement of fabrication, this problem is tackled.

Also as mentioned before, the gratings defined on the semiconductor in DFB based lasers must have specific physical conditions so a Bragg resonance at desired wavelengths can

be observed. In the next section we will discuss the structure required for these gratings and conditions required for operating at the bandgap region.

3.3. Bragg Gratings in a DFB Laser

Fig.3.3 presents a schematic of a Bragg gratings embedded in a semiconductor. In this structure the modulation of refractive indices between n_1 and n_2 in grating region will compose a 1D photonic crystal capable of Bragg resonance at specific wavelengths. Assume a plane wave with wavelength λ is incident on a Bragg grating structure with pitch Λ at an angle, θ_i. This plane wave will be reflected with an angle equal to θ_d.

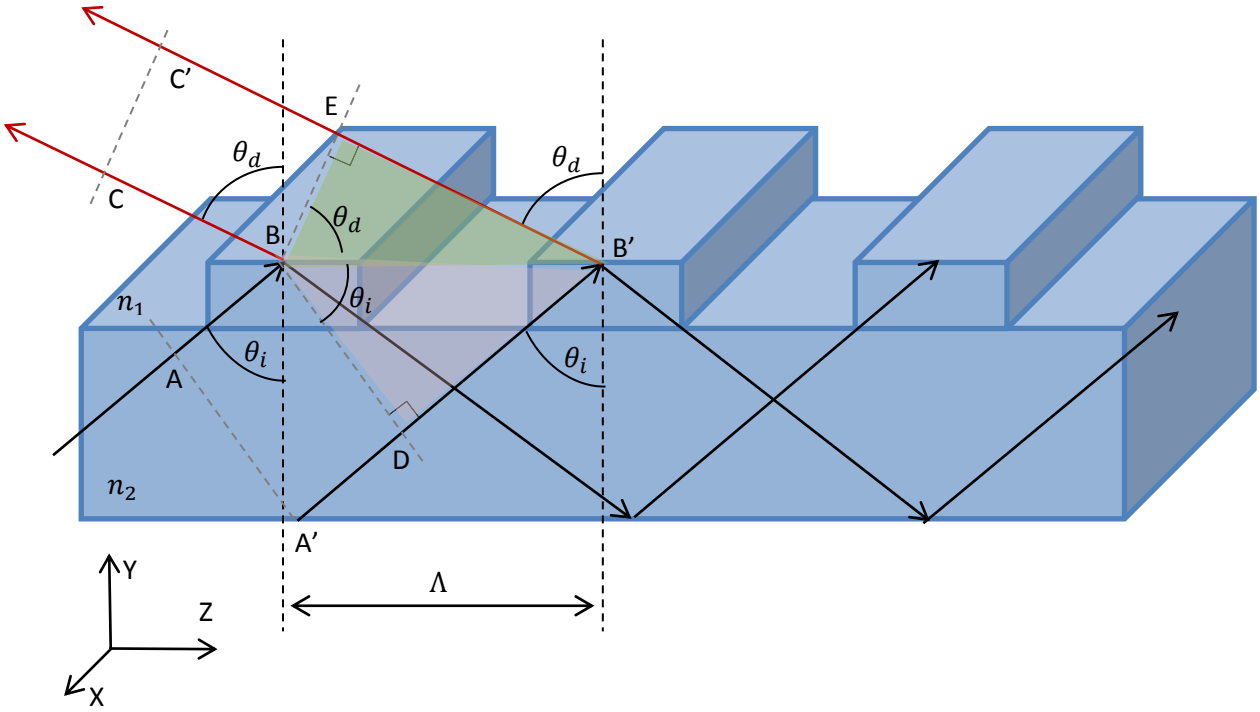

Fig. 3.3. Schematic of a Bragg gratings structure embedded in a semiconductor with pitch Λ. A plane wave with wavelength λ is incident at an angle θ_i.

Due to the periodic structure of the gratings, set of plane waves separated by one period will experience identical reflection and diffraction. Therefore, consider two rays each starting and ending at the same wavefronts which are separated by one period. One of the plane waves travels a distance of L_{ABC}, and the other one a distance of $L_{A'B'C'}$ before arriving at the same wavefront. To realize resonance in such structure, constructive

interference must be of the case for these two defined sets of rays. To have that, every periodically spaced rays should be in-phase with each other at the output wavefront (C - C'). We know that the phase of a plane wave at each point along the path can be calculated by the equation below:

$$\varphi = \frac{2\pi nL}{\lambda}$$

Equation 3.1

where n is the refractive index of the medium, and L is the distance traveled. Hence the two plane waves described here, will be in-phase with each other when:

$$\frac{2\pi n}{\lambda}(L_{ABC}) = \frac{2\pi n}{\lambda}(L_{A'B'C'}) + 2\pi M$$

Equation 3.2

where M is an integer. This equation shows that the relative difference of two path lengths is important to make a constructive interference. From Fig.3.3 it is clear that the path A'B'C' is longer than the ABC path by the length of DB' and B'E. Hence Equation 3.2 can be rewritten as:

$$\frac{n}{\lambda}(L_{A'B'C'} - L_{ABC}) = \frac{n_2 L_{DB'}}{\lambda} + \frac{n_1 L_{B'E}}{\lambda} = M$$

Equation 3.3

M in Equation 3.3 is a positive or negative integer and is defined as the diffraction order. Using sinusoidal relations in highlighted right-angle triangles in Fig.3.3, we obtain:

$$\frac{n_1 \Lambda sin\Theta_d}{\lambda} + \frac{n_2 \Lambda sin\Theta_i}{\lambda} = M$$

Equation 3.4

Since M in equation above is an integer, to achieve a constructive interference of reflected lights only particular values of wavelength will satisfy the condition. Hence only particular wavelengths will be reflected strong enough for lasing purposes which again verifies the properties of resonant regime of photonic crystals.

Since the laser cavity designed for DFB lasers are an optical waveguide, it therefore should meet the light confinement restrictions. Assuming $n_2 > n_1$ and an angle of

incidence Θ_i, to permit total internal reflection at the interface between the two refractive indices from Snell's law we must have:

$$sin\,\Theta_i \geq \sin\Theta_d = \frac{n_1}{n_2}$$

Equation 3.5

Substituting this condition into Equation 3.4 we get:

$$\sin\Theta_d \geq \left(\frac{M\lambda}{\Lambda n_1} - 1\right) = \left(\frac{2M}{p} - 1\right),$$

Equation 3.6

where p is defined as below and is called the grating order:

$$p = \frac{2\Lambda n_1}{\lambda} \approx \frac{2\Lambda n_{eff}}{\lambda}$$

Equation 3.7

In Equation 3.7 we assume that the difference between the two refractive indices used in the gratings is negligibly different, such that n_1=n_2=n_{eff}. This approximation is suited in case of LC-DFB lasers where the Bragg gratings are defined by width modulation of a ridge waveguide which are only evanescently coupling the optical mode to the grating region. Hence the effective refractive index in the narrow and wide region is nearly identical.

To apply the generalized relations above to the Bragg gratings in a DFB laser we have to consider that an incident light travelling along the longitudinal (z) direction is desired which diffracts backwards along the direction of propagation (-z). To satisfy these conditions we have $\theta_d = \theta_i = \frac{\pi}{2}$. Substituting these values for incident and reflected angles into equation 4.6, we obtain $sin\theta_d = 1$ .Using the equality situation in the relation we will have the constructive interference condition of

$$\frac{M}{p} \geq 1 \Rightarrow p \geq M$$

Equation 3.8

As a result if we wish to provide feedback for light of wavelength λ_b, then from the definition of p in Equation 3.7 we should select a grating with a period of

$$\Lambda \geq \frac{M\lambda_B}{2n_{eff}}$$

Equation 3.9

According to Equation 3.9 choosing different integers for M, the grating period will have multiple solutions. If first order gratings is selected, p=1, then based on Equation 3.6 only two solutions is possible. The first solution is when M=0. In this case using the equality situation in the relation, $\sin\theta_d = -1$, or $\theta_d = -\frac{\pi}{2}$. Hence the light experiencing zero order diffraction, M=0, propagates along the direction of propagation. M=1 provides a second solution and we obtain $\sin\theta_d = 1$, or $\theta_d = \frac{\pi}{2}$. In this case the light coupled to the first diffraction order produces a backward scattering wave from the initial direction of propagation, providing a feed-back effect.

Although the condition described above for the first order gratings is very close to conditions desired for a laser cavity with plane waves propagating forward and backward, higher order gratings can be of interest too. From Equation 3.7 clearly by choosing larger integers for p we can obtain larger values for the pitch, Λ. Since industrial lithography techniques have limitations in terms of the minimum features they can define, realizing Bragg gratings with larger dimensions will allow easier and more relax fabrication; However operating at larger grating orders results in diffraction orders in unwanted directions causing loss of energy as will be discussed later on.

Selecting a second order grating, p=2, the feed-forward and feedback solutions occur for M=0 and M=2 respectively. In this case an additional diffraction angle is introduced by having M=1. From Equation 3.6 this diffraction order results in $\sin\theta_d = 0$, or $\theta_d = 0$. The physical interpretation of this solution is a reflected wave perpendicular to the propagation. These set of plane waves will radiate away from the cavity and contribute to the loss of the device. However this phenomenon can be exploited in surface-emitting lasers [65]. Similarly in case of a third order gratings with p=3, in addition to the feed-forward and feedback solutions, selecting M=1 and M=2 results in plane waves diffracted at angles of $\theta_d = \pm sin^{-1}(\frac{1}{3})$. Although optical loss is increased in case of third order gratings with unwanted diffraction orders, considering the larger periods of structures in this case standard optical lithography (i-line stepper) can be used for

fabrication instead of e-beam lithography. This matter leads to more compatibility with CMOS technology and easier and cheaper fabrication leading to more manufacturing through-put. That is why third order Bragg gratings are attracting attentions for fabricating LC-DFBs.

Different modes with different directions in a Bragg medium will have interactions with each other which cause energy to be exchanged from one mode to another. That is why due to the interaction between higher order diffraction modes and the principal forward and backward modes, resonance frequency will be changed. Coupled-mode theory is developed to analyze these interactions between different modes in a medium. In the next section we will discuss this theory and how it fits to the problem concerned in this chapter.

3.4. Coupled Mode Theory

In section before we discussed how Bragg gratings can be applied to build DFB lasers that provide higher spectrum purity than FP lasers. Operation of these types of lasers relies on backward Bragg scatterings when operating at wavelengths in the bandgap region of the structure. To evaluate the performance of such structures different methods has been introduced [66-68]. Coupled-mode theory was the first method used to analyze and model DFB lasers by Kogelnik and Shank in 1972 [69]. In this section we look over details of this method and its application in modeling DFB lasers.

Coupled mode theory in general is developed to treat problems involving energy exchange between different modes. Consider two eigen modes of an unperturbed medium with different frequencies and complex amplitudes of A and B having propagating disturbances of

$$a(z,x,t) = Ae^{i(\omega_a t \pm \beta_a z)} f_a(x),$$

$$b(z,x,t) = Be^{i(\omega_b t \pm \beta_b z)} f_b(x)$$

Equation 3.10

Where $f_a(x)$ and $f_b(x)$ are the transverse mode profiles. Based on coupled-mode theory, in presence of a perturbation such as periodic electric field, sound wave or surface corrugation, power is exchanged between these two modes and complex amplitudes A

and B will no longer be constant. In this case the amplitudes will be a function of z, the propagation axis. It is shown by Yariv[70], that the complex amplitudes will obey relations of the form below:

$$\frac{d\,A}{dz} = \kappa_{ab} B e^{-i\delta z}$$

$$\frac{d\,B}{dz} = \kappa_{ba} A e^{+i\delta z}$$

Equation 3.11

In equation above δ is a phase mismatch depending on propagating constants defined as [69]:

$$\delta \equiv \frac{\beta^2 - \beta_0^2}{2\beta} \approx \beta - \beta_0 = n(\omega - \omega_0)/c$$

Equation 3.12

δ indicates the deviation from the oscillation frequency ω from the Bragg frequency ω_0, hence at the Bragg condition we have δ = 0. In equation above since the frequency deviations are assumed to be small, we have set β / $\beta_0 \approx 1$. κ_{ab} and κ_{ba} also are coupling coefficients which are determined by the physical situation of the propagation medium under consideration.

Kogelink [69] extends this approach to periodic structures of first-order Bragg gratings to analyze the feedback mechanism in DFB lasers. This method will provide the energy exchanged between the contra-directional modes: forward propagating light and the modes coupled to the first order diffraction and hence propagating backward. In this case the electric filed will be in the form of:

$$\mathrm{E(x)} = A e^{i(\omega_a t + \beta_a z)} f_a(x) + B e^{i(\omega_b t - \beta_b z)} f_b(x)$$

Equation 3.13

Coupled-mode model for these two sets of modes is derived where α is the modal gain:

$$-\frac{d\,A(z)}{dz} + (\alpha - j\delta)A(z) = j\kappa_{ab} B(z)$$

$$\frac{d\,B(z)}{dz} + (\alpha - j\delta)B(z) = j\kappa_{ba} A(z)$$

Equation 3.14

This equation reveals how amplitude of both forward and backward propagating waves is slowly changing depending on the value of the other ray's amplitude. This relation between two contra-directional waves is depicted in Fig.3.4. Coupling coefficients in this relation determine how strongly these backward and forward propagating rays are related to each other. These coefficients depend on the physical situation under consideration. It is also important to notice in Fig.3.4 that coupled-mode theory models the resonant medium as if it were homogenous and scatters continuously along its length rather than discretely at each abrupt junction of the gratings.

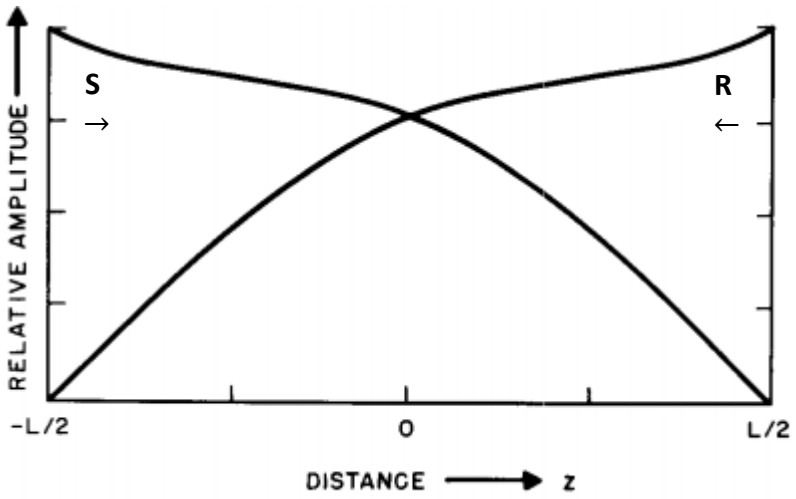

Fig. 3.4. Amplitudes of forward and backward propagating waves in a Bragg grating structure.(Copyright AIP 1971, reproduced with permission after reference [69])

Theories discussed above study the coupling of two modes and the special case of first order Bragg gratings with two forward and backward plane waves. Streifer [71] on the other hand, develops coupled-mode model to account for the effects of radiation loss and other partial wave coupling. This problem is formulated in such a way that these additional effects are included in the coupled-mode equations by the inclusion of three constants, ζ_1, ζ_2 and ζ_4 in addition to the usual coupling coefficients κ_{ab}. The modified coupled wave equations are

$$\frac{d\,A(z)}{dz} + (-\alpha - j\delta - j\zeta_1)A(z) = j(\kappa_{ab} + \zeta_2)B(z)$$

$$-\frac{d\,B(z)}{dz}+(-\alpha-j\delta-j\zeta_3)B(z)=j(\kappa_{ba}+\zeta_4)A(z)$$

Equation 3.15

Where

$$\zeta_1=\sum_{\substack{q=-\infty\\ q\neq 0.-p}}^{\infty}\eta_{q,-q}^{(0)}$$

$$\zeta_2=\sum_{\substack{q=-\infty\\ q\neq 0.-p}}^{\infty}\eta_{q,-q}^{(p)}$$

$$\zeta_3=\sum_{\substack{q=-\infty\\ q\neq 0.p}}^{\infty}\eta_{q,p-q}^{(p)}$$

$$\zeta_4=\sum_{\substack{q=-\infty\\ q\neq 0.p}}^{\infty}\eta_{q,p-q}^{(0)}$$

Equation 3.16

Where

$$\eta_{r,s}^{(i)}=\frac{k_0^2}{2\beta_0 P}\iint_G A_r(x)\varepsilon_0(x)\varepsilon_s^{(i)}(x)dx$$

Equation 3.17

In Equation 3.17, P is the total power, $A_r(x)$ is the Fourier coefficient of the grating, $\varepsilon_0(x)$ is the transverse fundamental mode profile and $\varepsilon_s^{(i)}(x)$ is the solution for the partial waves where the one with i= 0 is generated by the wave in +z direction and i=p corresponds to the wave generated by the wave in –z direction.

The theory discussed in this chapter for gratings in DFB lasers, can be applied to LC-DFB lasers as well. In the next section we discuss how this coupled mode theory can be exploited in analyzing and further, homogenization of LC-DFBs near resonant. Homogenization that will be discussed in next section will reveal the need for complex

calculations or time consuming simulations to find characteristics of a LC-DFB laser including coupling coefficients, resonance frequency, etc.

3.5. Analyzing LC-DFB lasers

Earlier we discussed how resonance at Bragg gratings can be exploited to make DFB lasers. Also we introduced coupled mode theory as a technique to analyze these structures. The noticeable feature considered in this theory was pointed out to be that it does not deal with reflection and diffraction at each abrupt junction but considers the wave scattering continuously in the medium.

Also we introduced LC-DFB lasers as an enhancement on DFB lasers which offer easier and cheaper fabrication process. However the more complex grating structure introduces complexity in analyzing the device and finding the coupling coefficient and resonance frequency. Here we introduce a homogenization approach where simply by knowing basic physical characteristics of a LC-DFB laser we can find the relevant laser properties.

In the proposed approach the LC-DFB structure will be approximated to a stack of dielectric layers. Having simplified the structure the transmission and scattering matrix of the device will be defined. Coupled-mode theory will be applied to the new definitions of the gratings and reflection and transmission coefficients will be derived from obtained relations. Scanning these coefficients over ranges of wavelengths, the resonance frequency and coupling coefficients will be determined. Following we will discuss each step in depth.

3.5.1 Matrix definition of the structure

To simplify the structure as the first step to homogenization, we consider each single period of gratings operating as the system in Fig.3.5:

Fig. 3.5. Schematic of a 4-port system.

Here a_1 and a_2 are the right going and left going plane waves respectively and b_1 and b_2 are their associated reflected waves. As discussed in chapter 2, Yeh and Yariv [40] have offered a transmission matrix relating all the four ports of this system as below:

$$\begin{bmatrix} b_2 \\ a_2 \end{bmatrix} = \mathrm{T} \begin{bmatrix} a_1 \\ b_1 \end{bmatrix}$$

Equation 3.18

Finding the T matrix of a single grating can lead to the definition of the whole device by multiplication of T matrices of each scattering element:

$$\mathrm{T(n)} = \mathrm{T}_n \dots \mathrm{T}_3 \mathrm{T}_2 \mathrm{T}_1$$

Equation 3.19

And in case they are identical as in LC-DFB lasers we have:

$$\mathrm{T(n)} = \mathrm{T}^n$$

Equation 3.20

On the other hand, lowery [67] has offered another approach to the system above consisting of a single period of grating, defining a scattering matrix. A scattering matrix for the system in the Fig.3.5 is defined as below:

$$\begin{bmatrix} b_1 \\ b_2 \end{bmatrix} = \mathrm{S} \begin{bmatrix} a_1 \\ a_2 \end{bmatrix}$$

Equation 3.21

Having S matrix of one period of a certain structure, the definition of the whole system consisting of n periods can be found by an S matrix calculated using Redheffer star

product to multiply S matrices of each section. This product is defined as in Equation 3.22 assuming matrix C to be the Redheffer star product of matrix A and B:

$$C = A \otimes B = \begin{bmatrix} a_{11} + a_{12}(I - b_{11}a_{22})^{-1}b_{11}a_{21} & a_{12}(I - b_{11}a_{22})^{-1}b_{12} \\ b_{21}(I - a_{22}b_{11})^{-1}a_{21} & b_{22} + b_{21}(I - a_{22}b_{11})^{-1}a_{22}b_{12} \end{bmatrix}$$

Equation 3.22

The T matrix is a complete description of a linear scattering system equivalent to the S matrix and vice versa. The elements of the T (S) matrix may therefore be found from the S (T) matrix. Relations below show how these two matrices can be derived from each other for any system:

$$\begin{bmatrix} b_2 \\ a_2 \end{bmatrix} = \mathrm{T} \begin{bmatrix} a_1 \\ b_1 \end{bmatrix} = \begin{bmatrix} s_{12} - s_{22}s_{12}^{-1}s_{11} & s_{22}s_{12}^{-1} \\ -s_{12}^{-1}s_{11} & s_{12}^{-1} \end{bmatrix} \begin{bmatrix} a_1 \\ b_1 \end{bmatrix},$$

$$\begin{bmatrix} b_1 \\ b_2 \end{bmatrix} = \mathrm{S} \begin{bmatrix} a_1 \\ a_2 \end{bmatrix} = \begin{bmatrix} -t_{22}^{-1}t_{21} & t_{22}^{-1} \\ t_{11} - t_{12}t_{22}^{-1}t_{21} & t_{12}t_{22}^{-1} \end{bmatrix} \begin{bmatrix} a_1 \\ a_2 \end{bmatrix}$$

Equation 3.23

Hence having a definition for transmission matrix of a system, we can derive the associate scattering matrix using relations above. The transmission matrix for a single period consisting of two layers with different refractive indices is derived by Yeh and yariv [40] to be:

$$\Gamma = \begin{bmatrix} \left[\cos(k_1 d_1) + i\frac{1}{2}(\chi^{-1} + \chi)\sin(k_1 d_1)\right]\exp(i\,k_2 d_2) & -i\frac{1}{2}(\chi^{-1} - \chi)\sin(k_1 d_1)\exp(i\,k_2 d_2) \\ -i\frac{1}{2}(\chi^{-1} - \chi)\sin(k_1 d_1)\exp(-i\,k_2 d_2) & \left[\cos(k_1 d_1) - i\frac{1}{2}(\chi^{-1} + \chi)\sin(k_1 d_1)\right]\exp(-i\,k_2 d_2) \end{bmatrix}$$

Equation 3.24

Where

$$\chi = \eta\frac{k_1}{k_2} \quad , \quad \eta = \begin{cases} 1 & TE \\ \frac{n_2^2}{n_1^2} & TM \end{cases}$$

Equation 3.25

Assuming waves propagating in direction z, $k_1$and k_2 are the wave numbers in layers with refractive index of n_1 and n_2 respectively so:

$$k_1 = \frac{2\pi n_1}{\lambda_0} \ ,$$

$$k_2 = \frac{2\pi n_2}{\lambda_0}$$

Equation 3.26

Knowing that, Equation 43.25 will reduce to:

$$\chi = \begin{cases} \frac{n_1}{n_2} & TE \\ \frac{n_2}{n_1} & TM \end{cases}$$

Equation 3.27

From description above, it is clear that by knowing the basic physical parameters of a single grating including refractive index and thickness of each layer the T matrix can be derived leading to describing the whole device.

Before applying relations derived above to the case of LC-DFB lasers and find the T matrix, it must be considered that in such devices the gratings are incorporated to the ridge waveguide. Although DFB lasers are designed using multilayer stack of dielectrics under the layer where ridge waveguide is embedded, in LC-DFB structures the width of ridge waveguide is modulated to periodically change the effective index realized by the fundamental mode. Hence to apply the matrix definitions discussed above to this kind of structures, first the fundamental mode effective index in ridge waveguide with different widths must be found.

Here by taking a Quantum Dot (QD) LC-DFB as an example, we find the effective index of narrow and wide ridge using different numerical methods using simulation tools. The values derived will be compared and then applied to define descriptive matrices. The QD LC-DFB laser taken as an example here has a structure summarized in table 3.1.

Table 3.1. Structural details of the studied QD LC-DFB laser

Layer No	Material Composition	Band gap Wavelength (nm)	Thickness (nm)	Doping level (cm^{-3})	Layer specific comments
10	$Ga_{0.47}In_{0.53}As$	1660	100	Zn:1.50E+19	p-contact
9	InP	919	1000	Zn:1.00E+18	Ridge
8	$Ga_{0.265}In_{0.735}As_{0.61}P_{0.425}$	1300	10	Zn:5.00E+17	Etch stop
7	InP	919	150	Zn:5.00E+17	SCH upper cladding
6	$Ga_{0.173}In_{0.827}As_{0.41}P_{0.622}$	1150	100	undoped	Quantum dot active region
5	Third Party Recipe	1500	70		
3	$Ga_{0.205}In_{0.795}As_{0.48}P_{0.553}$	1200	80		
2	InP	919	200	Si:5.00E+17	SCH lower cladding
1	InP	919	400	Si:1.00E+18	Buffer
0	InP	-	-	-	Substrate

In order to be able to simulate the structure composed of materials above, the refractive index of each layer must be determined. This structure is composed of GaInAsP layers each having different As fractions and hence different bandgap wavelengths. There are numerous methods to obtain refractive index of such materials knowing the As fraction or bandgap wavelength. Table below gives a summary, comparing results from different numerical methods proposed by Adachi [72], Broberg [73] and Webar [74]. Also FimmWave simulation tool can be used to find the refractive indices. In this software this value can be obtained from bandgap wavelength and also from the As fraction. Results derived from both methods are compared with other results in table 3.2.

Table 3.2. Comparison of the calculated refractive index of InGaAsP using different methods

Bandgap wavelength (nm)	As fraction	Adachi	Broberg	Webar	Fimmwave (As fraction)	Fimmwave (Bandgap wavelength)
1050	0.25	3.2604	3.2543	3.2637	3.2628414	3.2622422
1100	0.33	3.2907	3.2829	3.2910	3.2900443	3.290292
1150	0.41	3.3220	3.3121	3.3190	3.3180205	3.317433
1200	0.48	3.3504	3.3382	3.3444	3.3433685	3.3439661
1300	0.61	3.4077	3.3877	3.3951	3.3938199	3.3966243
1500	0.85	3.5951	3.4887	3.5292	3.5250235	3.5256889
1550	0.9	3.6278	3.5333	3.6331	3.6044203	3.6338947

As it is clear in table 3.2 although all results are in a good agreement, last three methods including FIMMWAVE techniques and Webar offer the closest and hence more accurate results. We use the refractive index calculated by FIMMWAVE from bandgap wavelength henceforth.

Having comprehensive epitaxial details of the structure we are able to find the effective index of the fundamental mode in narrow and wide ridge. Two different numerical methods is used here and compared; FDM using FimmWave and FEM by Comsol Multiphysics.

Fig.3.6 indicates the simulated results of the cross section of the QD LC-DFB in wide ridge and narrow ridge in Comsol. The fundamental mode at each width and their associated refractive index is derived. It is important to notice that in this structure the modes are sitting high enough so they can realize the modulation in the gratings and hence a good lasing performance. Based on this result the refractive index at narrow ridge is equal to n_1=3.207146 and for wide ridge we have n_2= 3.216815.

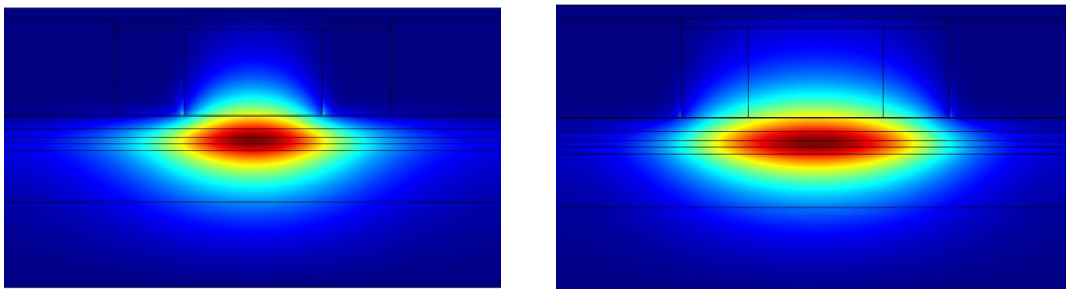

Fig. 3.6. Mode profiles at the narrow (left) and wide (right) ridge of the QD LC-DFB laser structure under study, simulated by FEM.

Same procedure has been performed to find effective refractive index realized by the fundamental mode by FDM method from FimmWave. Fig.3.7 and Fig.3.8 show the results obtained from this experiment. As can be seen here the refractive index of narrow ridge is calculated to be n_1=3.207482 and for the wide ridge we have n_2= 3.21699. Comparing these values to the results from FEM simulations of Comsol, we see that there is a good agreement for these two different methods.

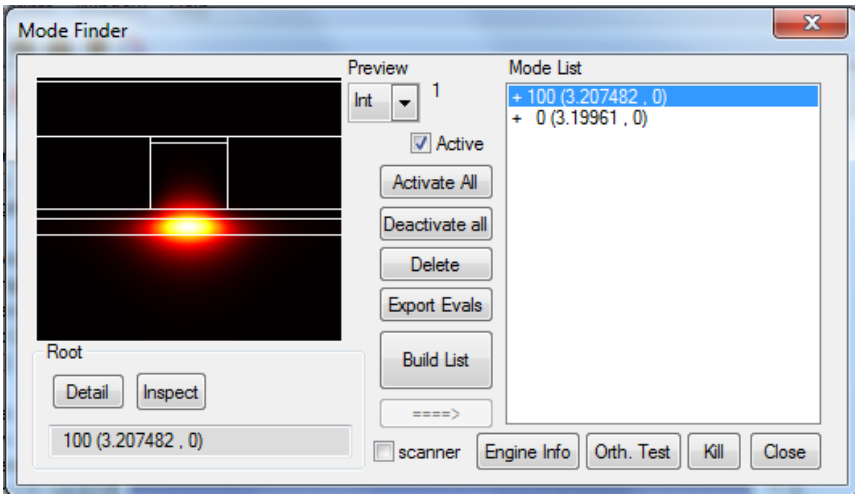

Fig. 3.7. Mode profile at the narrow ridge of the QD LC-DFB laser structure under study, simulated by FDM.

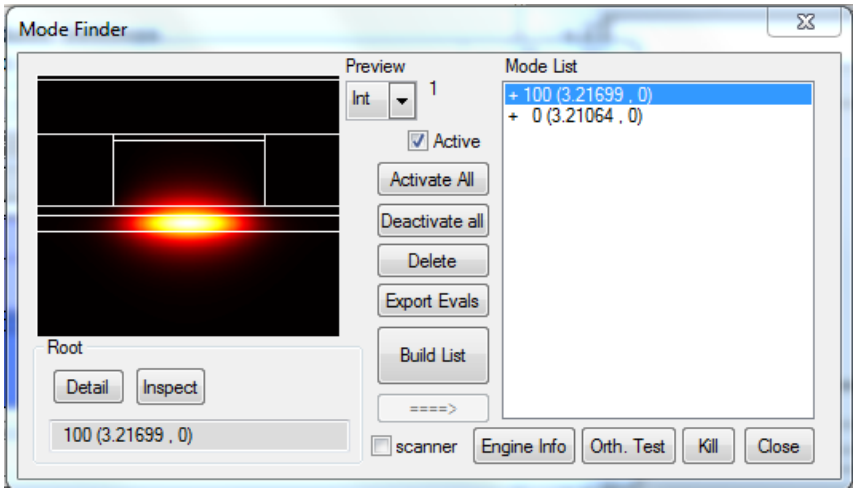

Fig. 3.8. Mode profile at the wide ridge of the QD LC-DFB laser structure under study, simulated by FDM.

Having calculated the effective refractive indices in narrow and wide ridge now we are able to simplify the LC-DFB structure analytically. In this regard we will replace the ridge waveguide with modulated width, with multilayer stack of dielectrics with alternating refractive indices of calculated n_1 and n_2. Fig.3.9 shows this simplification. Therefore the matrix definition discussed earlier can be applied to the simplified structure and T and S matrices can be described. It must be noted that although the effective indices calculated will be different in different wavelengths but considering the T matrix definition, we will see that it only depends on the ratio of narrow and wide ridge effective index and variation in their absolute value will not cause a noticeable change to the overall matrix.

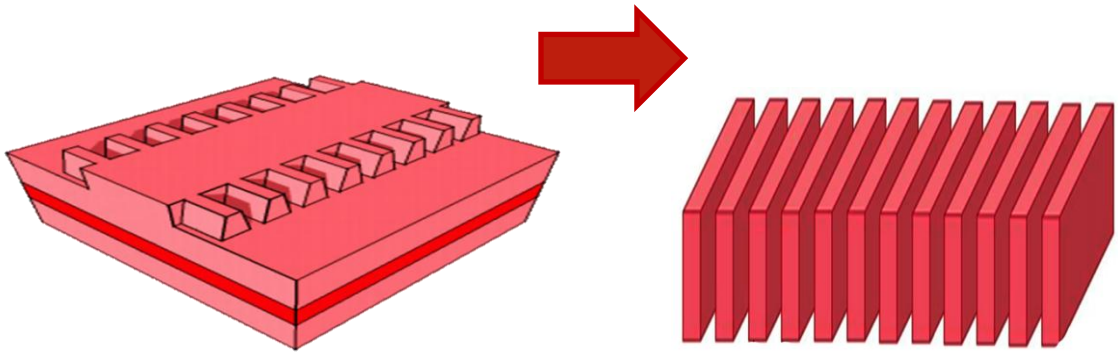

Fig. 3.9. Simplification of a LC-DFB laser to a Bragg gratings.

3.5.2. Coupled-Mode model of descriptive matrices

So far we have proposed a simplified structure for LC-DFB laser, so we can describe the device by its associate T and S matrix. In order to analyze the Bragg resonance in the structure and find out how the energy is exchanged between forward and backward propagating wave, we have to apply the coupled-mode theory to the matrix description of the device.

Equation 3.11 describing the Coupled-mode model of the modes in a medium can be rewritten as below for a single gating system of Fig. 3.5:

$$\mathbf{J}\frac{d\boldsymbol{A}}{dz} = i\boldsymbol{\mathcal{K}}\boldsymbol{A}$$

Equation 3.28

Where A is the matrix consisting of forward and backward propagating waves, K is the coupling coefficient matrix and J is a matrix defined as below:

$$\boldsymbol{A} = \begin{bmatrix} a_1 \\ a_2 \end{bmatrix},$$
$$\boldsymbol{J} = \begin{bmatrix} 1 & 0 \\ 0 & -1 \end{bmatrix},$$
$$\boldsymbol{\mathcal{K}} = \begin{bmatrix} 0 & \kappa^* \\ \kappa & 0 \end{bmatrix}$$

Equation 3.29

Substituting these definitions, the differential equation 3.28 has a solution of:

$$\boldsymbol{\mathcal{V}}(z) = exp(iz\mathbf{J}\boldsymbol{\mathcal{K}})$$

Equation 3.30

From equation above it can be deducted that:

$$\boldsymbol{\mathcal{V}}(z+\Lambda) = \exp(i(z+\Lambda)\mathbf{J}\boldsymbol{\mathcal{K}}) = exp(i\Lambda\mathbf{J}\boldsymbol{\mathcal{K}})\boldsymbol{\mathcal{V}}(z)$$

Equation 3.31

And more generally:

$$\boldsymbol{\mathcal{V}}(z+n\Lambda) = exp(in\Lambda\mathbf{J}\boldsymbol{\mathcal{K}})\boldsymbol{\mathcal{V}}(z) = [exp(i\Lambda\mathbf{J}\boldsymbol{\mathcal{K}})]^n\,\boldsymbol{\mathcal{V}}(z)$$

Equation 3.32

Hence considering the definition of T matrix in equation 3.18, the term $\exp(iz\boldsymbol{J}\boldsymbol{\mathcal{K}})$ is equal to transmission matrix for a single grating:

$$T = exp(i\Lambda\mathbf{J}\boldsymbol{\mathcal{K}})$$

Equation 3.33

Where $\boldsymbol{J}\boldsymbol{\mathcal{K}}$ can be calculated to be :

$$\boldsymbol{J}\boldsymbol{\mathcal{K}} = \begin{bmatrix} 0 & \kappa^* \\ -\kappa & 0 \end{bmatrix}$$

Equation 3.34

Since the eigen values of $\boldsymbol{J}\boldsymbol{\mathcal{K}}$ are $\pm|\kappa|$, substituting the coupling coefficient matrix into Equation 3.34, we obtain:

$$exp(i\Lambda\mathbf{J}\boldsymbol{\mathcal{K}}) = \cosh(|\kappa|z)\,\boldsymbol{I} + \sinh(|\kappa|z)\frac{i\boldsymbol{J}\boldsymbol{\mathcal{K}}}{|\kappa|}$$

Equation 3.35

And therefore:

$$T = exp(i\Lambda\mathbf{J}\boldsymbol{\mathcal{K}}) = \begin{bmatrix} \cosh(|\kappa|\Lambda) & \frac{i\kappa^*}{|\kappa|}\sinh(|\kappa|\Lambda) \\ -\frac{i\kappa}{|\kappa|}\sinh(|\kappa|\Lambda) & \cosh(|\kappa|\Lambda) \end{bmatrix}$$

Equation 3.36

Also using the relations in Equation 3.23, the scattering matrix can also be defined in terms of coupling coefficient as:

$$S(z) = \begin{bmatrix} -t_{22}^{-1}t_{21} & t_{22}^{-1} \\ t_{11} - t_{12}t_{22}^{-1}t_{21} & t_{12}t_{22}^{-1} \end{bmatrix} = \begin{bmatrix} \frac{i\kappa}{|\kappa|}\tanh(|\kappa|z) & \frac{1}{\cosh(|\kappa|z)} \\ \frac{1}{\cosh(|\kappa|z)} & \frac{i\kappa^*}{|\kappa|}\tanh(|\kappa|z) \end{bmatrix}$$

Equation 3.37

Accordingly the relation between coupled mode theory and matrix definition is described. Next we will use these derived S and T matrices to find lasing characteristics of the structure, including coupling coefficient and resonance frequencies.

3.5.3. Deriving Coupling Coefficient and Resonance Frequency

Earlier we summarized the complex structure of LC-DFB into a simple multilayer stack of dielectrics with alternating refractive indices. Also the associated S and T matrix of the simplified structure was defined. For homogenization, we have to be able to find the properties of the laser including resonant frequency and coupling coefficient near Bragg resonant.

To find the lasing characteristics of the device, matrix description of the whole structure is required. As mentioned before multiplying the T matrix by n times will provide the description of a system consisting of n periods of Bragg gratings. However according to the report by Cao [75], it has been experimentally proved that although calculating the T-matrix of a cascaded system is simple but it is prone to numerical instability. Whereas the S matrix description is more involved but more numerically stable. Hence the approach taken here is first to derive the transmission matrix of the grating from equation 3.24, and then use the relations derived in 3.23 to build the associate scattering matrix. The scattering matrix calculated for each grating can be multiplied n times by Redheffer star product to find the S matrix of the cascaded gratings. According to the definition of scattering matrix the s_{12} will represent the reflection coefficient and s_{11} will indicate the transmission coefficient.

This procedure is performed for the described QD LC-DFB with a pitch of Λ=0.723 um and 1024 gratings with Matlab coding. Since the order of gratings is defined by the relations between the propagating light wavelength and the period of gratings (equation 43.7), here by having a constant pitch the wavelength will be scanned near first and third Brillouin zone bandgaps to evaluate the structure as if it was first order or third order Bragg gratings respectively.

Fig.3.10 and Fig.3.11 below are the wavelength scanning of the transmission and reflection coefficients of the structure near first and third order Bragg resonance of the grating. As can be seen near resonance the transmission coefficients reduce to near zero and reflection coefficients max up. The points where these coefficient peak up are considered to be the resonance wavelengths of the structure. From Fig.3.10 and Fig.3.11 we can conclude that the first order resonance happens for wavelength of $\lambda_1 = 1.446\ um$

and the third order resonance occurs at $\lambda_3 = 0.482\,um$. It is noticeable that $\lambda_1 = 3\lambda_3$ which is consistent to the Equation 3.7 defining orders of gratings.

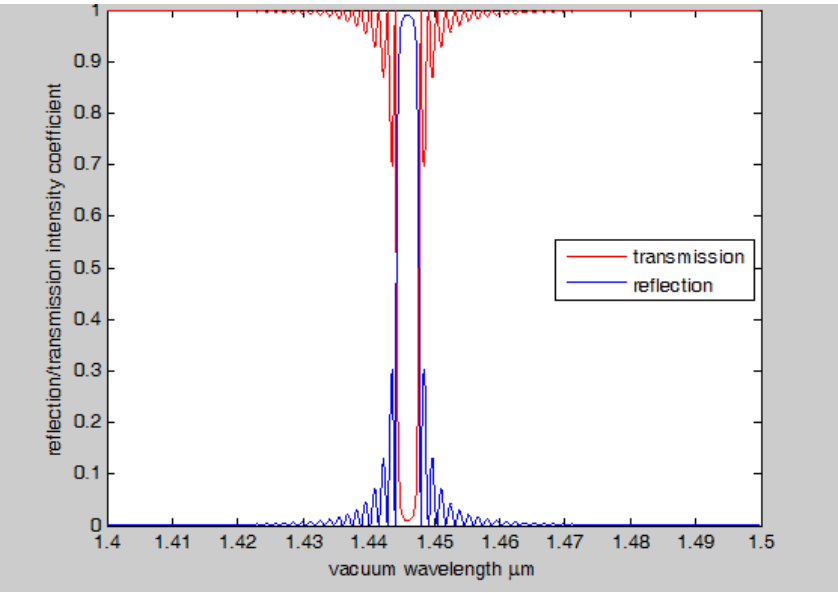

Fig. 3.10. Wavelength scanning of reflection and transmission coefficients of the structure in the first Brillouin zone, using the homogenization method.

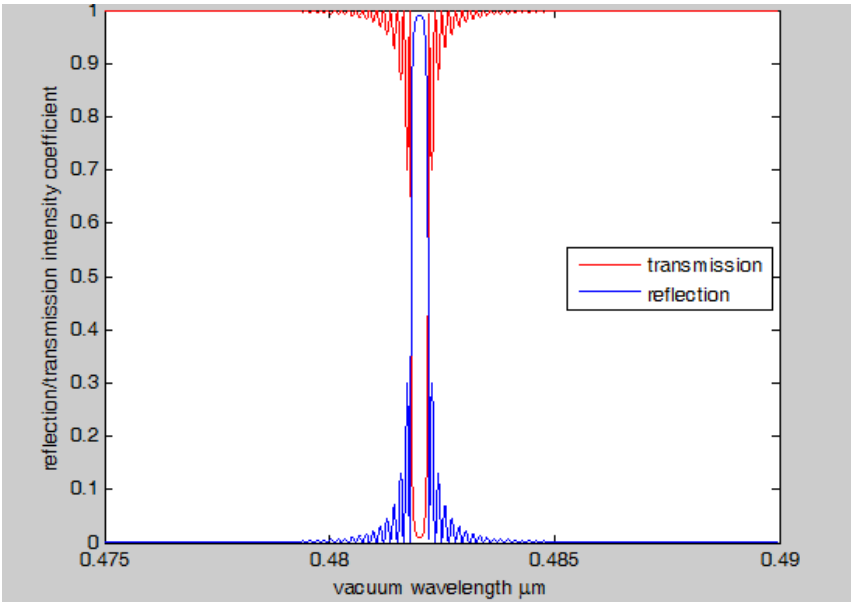

Fig. 3.11. Wavelength scanning of reflection and transmission coefficients of the structure in the third Brillouin zone, using the homogenization method.

It must be considered that the wavelengths found in this experiment are the wavelengths at the medium and equal to $\lambda = \lambda_0/n_{eff}$ where n_{eff} is the effective index of the medium and λ_0 is the vacuum wavelength.

The matrix definition of the gratings can also be used to estimate the coupling coefficients. For a single period it is expected that $|\kappa|\Lambda \ll 1$ due to the small propagating length. Hence considering the definition of transmission matrix in terms of coupling coefficient, Equation 3.36, we have following matrix indices near resonance:

$$|T| \approx \begin{bmatrix} 1 & |\kappa|\Lambda \\ |\kappa|\Lambda & 1 \end{bmatrix}$$

Equation 3.38

and based on 3.37 also we have:

$$|S| \approx \begin{bmatrix} |\kappa|\Lambda & 1 \\ 1 & |\kappa|\Lambda \end{bmatrix}$$

Equation 3.39

Considering the T matrix defined in Equation 3.24 and approximations derived above we can simply find the coupling coefficients for any kind of structure. It must be noted that this estimate takes account of the change in wave-vector across each interface but ignores the change in transverse profile and hence the coupling to and from higher order modes. The T matrix of Equation 3.24 is brought here for further considerations.

$$\Gamma = \begin{bmatrix} \left[\cos(k_1 d_1) + i\frac{1}{2}(\chi^{-1} + \chi)\sin(k_1 d_1)\right]\exp(i\,k_2 d_2) & i\frac{1}{2}(\chi^{-1} - \chi)\sin(k_1 d_1)\exp(i\,k_2 d_2) \\ -i\frac{1}{2}(\chi^{-1} - \chi)\sin(k_1 d_1)\exp(-i\,k_2 d_2) & \left[\cos(k_1 d_1) - i\frac{1}{2}(\chi^{-1} + \chi)\sin(k_1 d_1)\right]\exp(-i\,k_2 d_2) \end{bmatrix}$$

Equation 3.40

Assuming $n_1 \sim n_2$ in LC-DFB lasers, $\frac{1}{2}(\chi^{-1} + \chi)$ will be close to 1 and hence the diagonal elements will have a modulus close to unity as expected in equations 3.38. In the off diagonal elements, $\sin(k_1 d_1)$ is also close to unity near Bragg resonance. Knowing that, the relation between $\frac{1}{2}(\chi^{-1} - \chi)$ term and coupling coefficient is derived from below where in case of TE we have $\chi = n_1/n_2$:

$$t_{12} = t_{21} = \frac{1}{2}(\chi^{-1} - \chi) = \frac{n_2^2 - n_1^2}{2n_1 n_2} = \frac{(n_2 - n_1)(n_2 + n_1)}{2n_1 n_2}$$

Equation 3.41

Considering that n_a=$(n_2 + n_1)/2$ where $n_a$is defined as the average of refractive indices, it can be estimated that:

$$n_1 n_2 = n_a^2$$

Equation 3.42

Hence:

$$t_{12} = t_{21} = \frac{(n_2 - n_1)}{n_a} = \frac{2(n_2 - n_1)}{(n_2 + n_1)}$$

Equation 3.43

Therefor comparing to relations in Equation 3.38 we have an equation estimating the coupling coefficients near resonance:

$$|\kappa| = \frac{2(n_2 - n_1)}{\Lambda(n_2 + n_1)}$$

Equation 3.44

3.6. Verification

In the last section we used Matlab coding to find resonance frequency of the example QD LC-DFB laser in first and third Brillouin zone bandgaps after simplifying the structure and building its associate matrix definitions. To verify the analytical approach and the results derived by the proposed homogenization technique, the device was simulated by FimmWave and EME numerical method was used to find first and third order resonance at the structure defined earlier.

Fig.3.12 and fig.3.13 depict the results from scanning transmission and reflection of the device near first and third Brillouin zone bandgaps finding first and third order resonance wavelengths respectively. It must be noted that in this simulation tool the horizontal axes scans over vacuum wavelength. From diagrams in Fig.3.12 and Fig.3.13 it is deducted that first order resonance wavelength is equal to $\lambda_{0-1} = 4.555\, um$ and the third order resonance wavelength is $\lambda_{0-3} = 1.547\, um$.

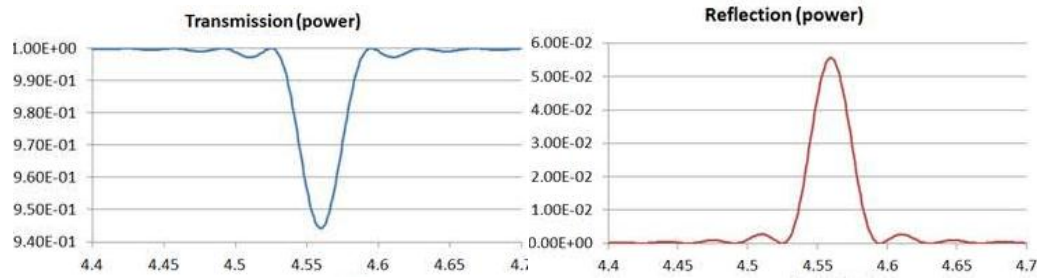

Fig. 3.12.Wavelength scanning of reflection and transmission coefficients of the structure in the first Brillouin zone, calculated by EME.

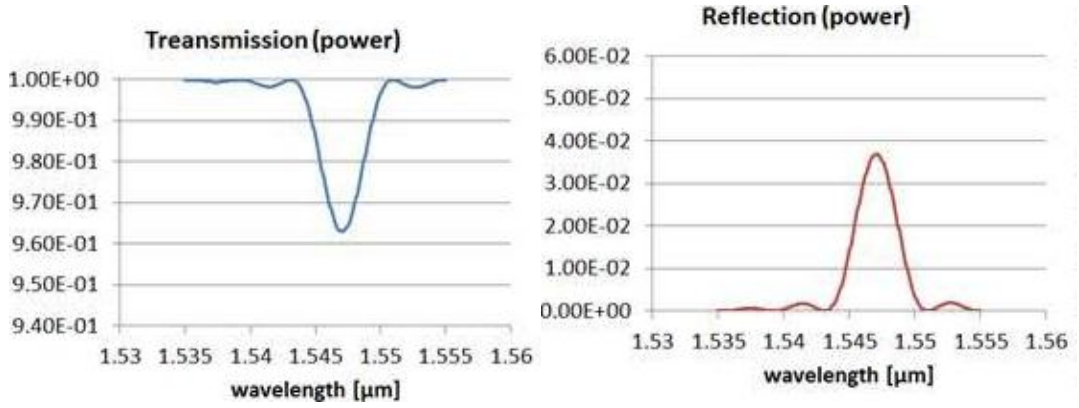

Fig. 3.13. Wavelength scanning of reflection and transmission coefficients of the structure in the third Brillouin zone, calculated by EME.

To be able to compare simulation results with the results from analytical approach we have to find the wavelength in the medium at vacuum wavelengths λ_{0-3} and λ_{0-1}. To do that n_{eff} at those specific wavelengths is required. The n_{eff} required must be an average of the narrow and wide ridge. Considering the cross sectional structure in Fig.3.14 designed in Comsol for a LC-DFB, the red highlighted rectangles will have refractive index of 3.18 (similar to that of the central rectangle) to define a wide ridge. While for the case of a narrow ridge, this refractive index will be set to 1.45 equal to the cladding refractive index (Silica).

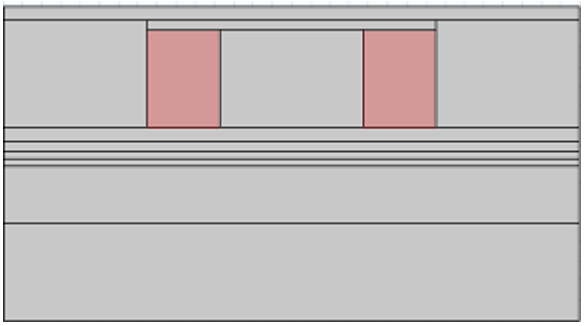

Fig. 3.14. The cross sectional structure; The red highlighted rectangles will have refractive index of (a) 3.18 to define a wide ridge, (b) 1.45 to define a narrow ridge and 1(c) 2.47 to define an average ridge.

To define an average cross section, the refractive index of highlighted areas can be set to the average of relative permittivities, derived from:

$$n_{av} = \sqrt{f n_{InP}^2 + (1-f) n_{Silica}^2}$$

Equation 3.45

Where f is the fill factor of the wide ridge which is assumed to be f=0.5 here. Hence n_{av} can be calculated to be 2.47. Using this refractive index to find n_{eff}, an effective index of 3.1312 and 3.2093 will be found at λ_{0-1} and λ_{0-3} respectively. Using these values in equation $\lambda = \lambda_0/n$, the wavelength in the medium will be derived to be 1.454 um and 0.481 um for the first order and third order resonance respectively.

As it is clear, the resonance wavelengths obtained from simulation tools is very close to the ones derived from the analytical approach (0.5% > error), which verifies accuracy and validity of the proposed approach.

3.7. Summary

In this chapter we introduced DFB lasers and more specifically LC-DFB lasers as an application of 1D photonic crystals in resonant region, called Bragg gratings. Details of resonance at this kind of gratings and their different operational modes called grating orders where introduced, where third order gratings where suggested for application in devices since they offer large enough grating periods that can be defined by optical

lithography used in CMOS technology, offering cheaper and more compatible fabrication process.

Then coupled-mode theory was discussed as a method to analyze the energy exchange between different modes in a medium. This theory's extension to the case of modes in DFB based lasers was introduced including devices using first order Bragg gratings with only two sets of modes and higher order Bragg gratings which also have modes coupled to higher order diffractions.

Considering the complex structure of LC-DFBs, a homogenization method was proposed for easier and less time consuming analysis of the structure. In this method the structure is first simplified to a stratified medium and the transmission matrix and scattering matrix are used to describe its properties. Using coupled-mode model, reflection and transmission coefficients are derived from the matrix definition of the system and an estimation of coupling coefficients is obtained. Scanning the reflection and transmission coefficients over wavelength the resonance frequency can be provided.

To verify the method EME simulation using FIMMWAVE was performed for the structure and resonance frequencies were calculated. Experimental results show a good agreement to the analytical results. (0.5% > error)

Chapter 4. Polarization Management

4.1. Introduction

The polarization of the light in traditional long distance fiber-optic signal transmission is not used and need not to be considered. In this case the polarization varies from input to output and consequently the output light is randomly polarized which does not harm the quality of the signal in this technology[1]. On the other hand, in the case of on-chip silicon photonics, polarization management is an important issue to deal with. Different polarization states possess different properties and there are integrated photonic devices that only support one kind of polarization mode. In the following chapter, firstly polarization states in planar waveguides will be introduced and the demand for polarization management for light-on- chip will be discussed thoroughly. Different approaches regarding polarization conversion will be introduced and recent advancements in this area will be critically analyzed.

4.2. Polarization States in Planar Waveguides

Maxwell's equations govern light propagation in planar waveguides. Eigen-solutions of Maxwell's equations under appropriate boundary conditions imposed by waveguide geometry, provide optical modes of the waveguide. Fig. 4.1 illustrates a three layer asymmetric dielectric slab waveguide consisting of a core layer, lower cladding and upper cladding which provide the boundary conditions for the solution of the wave equation.

[1] Installed optical fibers are nominally circularly symmetric in structure and isotropic. Environmental perturbations break these symmetries causing the polarization to evolve and hence the output state of polarization (SOP) of a long length of fiber can be anywhere on the Poincare sphere; Since the environmental perturbations are time-varying so the output SOP will move around on the Poincare sphere i.e. at any instant for a coherent source, the SOP at the output is definite but it can be anywhere on the Poincare sphere and follows a random path in time. This is different than de-polarized light which corresponds to an incoherent source.

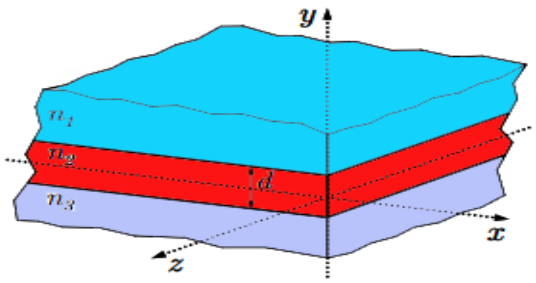

Fig. 4.1. A three layer asymmetric dielectric waveguide consisting of a core layer, lower cladding and upper cladding.

In this simple slab waveguide with just one dimensional confinement (in y direction), two orthogonally polarized modes can be supported: the Transverse Electric (TE) and the Transverse Magnetic mode (TM). In the TE mode the electric field is perpendicular to the propagation direction and lies in the plane of the core layer, $E_y = E_z = H_z = 0$.While in case of the TM mode the field distribution is such that the magnetic field is perpendicular to the propagation direction and lies in the plane of the core layer, $H_z = H_y = E_x = 0$.

Application of slab waveguides in integrated photonics is rare and two dimensional confined waveguides such as strip or ridge waveguides are commonly used. In such waveguides, depicted in Fig. 4.2, light is confined in both the x- and y-direction and is guided along the z direction. In this case since the propagating light must satisfy the boundary conditions imposed by the waveguide in both the x- and y-direction the requirement for the field components defined for the slab waveguides, either $E_y = E_z = H_z = 0$ for TE or $H_z = H_y = E_x = 0$ for TM, is no longer valid. In these waveguides although pure TE and TM modes cannot be defined, the term “TE-like mode” is used for hybrid modes in which E_x and H_y components dominate, and “TM like mode” is used for the mode in which E_y and H_x have the most power.

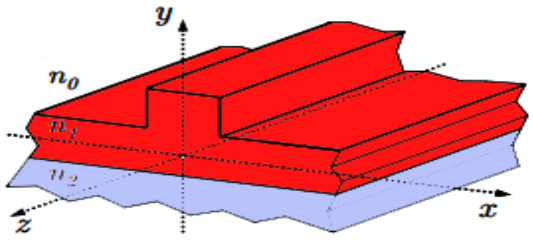

Fig. 4.2. A ridge waveguide in which light is confined in both the x and y direction and is guided along z direction.

A ridge waveguide typically is in a rectangular shape. For a perfectly symmetric waveguide, the propagation constants of the two orthogonal fundamental modes (TE and TM) are identical due to the identical boundary conditions imposed by the geometry. However, waveguides are rarely perfectly symmetric, and even in the case where the geometry is designed to be symmetric, external factors such as fabrication inaccuracies, temperature fluctuations, or stress cause the characteristics of the two modes to be generally different. In this case, TE and TM will realize quite different effective refractive indices, n_{eff}, which results in waveguide birefringence. For example, the index difference is nearly 0.7 for a silicon waveguide with a dimension of 450 nm and 220 nm (typical dimensions of a waveguide in SOI). Based on equation below for propagation constant where λ is the light wavelength,

$$\beta = n_{eff}\frac{2\pi}{\lambda}$$

Equation 4.1

The propagation constants of these two modes will be different and will travel along the waveguide with different speeds. Due to these different propagation properties, these two polarization modes will not be able to couple to each and develop a phase difference as they propagate, which alters the total polarization of the wave.

Consequently in an integrated photonic circuit, light at the input port of a photonic device, will not have a fixed polarization. Similarly in the case of light in an optical fiber, the polarization of light varies from input through output. Therefore the light coupled from a fiber to a PIC is randomly polarized. That is while most of the structures in silicon photonics, for example, on-chip lasers [76], modulators [77], filters [78] require a certain

polarization and polarization-dependent dispersion and polarization-dependent loss are important issues in photonic integrated circuits.

Geometrical anisotropy and fabrication inaccuracies, and also compatibility of polarization dependent PICs with traditional fiber optic systems, indicate the need for further polarization management on chip, such as rotating, splitting and combining different polarizations. Also recently, polarization division multiplexing (PDM) with coherent detection using silicon photonics has also attracted much attention. This trend further highlights the importance of polarization management in PICs to make full use of the transmission channel and obtain long-haul and high-speed optical communication. [79]

Following different approaches to polarization management, and efficient structures for polarization reported in literature will be introduced and reviewed.

4.3. Polarization Management

Earlier we discussed concerns on different polarizations existing in PICs and polarization dependent loss and dispersion in photonic devices. A general solution to overcome the polarization sensitivity of PIC is devices based on polarization-diversity technology [80,81]. In this technology the input light is separated by a polarization splitter and two polarized beams are obtained (i.e. TE and TM). Using a polarization rotator, one of them (e.g. TM) is converted into the orthogonal one (TE). Then the two beams with identical polarization enter two similar PICs separately and two identical outputs are expected. A second polarization rotator is used to convert one of the outputs to the other polarization state. Finally, two orthogonal beams are obtained and combined with a polarization beam combiner. This mechanism is illustrated in Fig. 4.3.

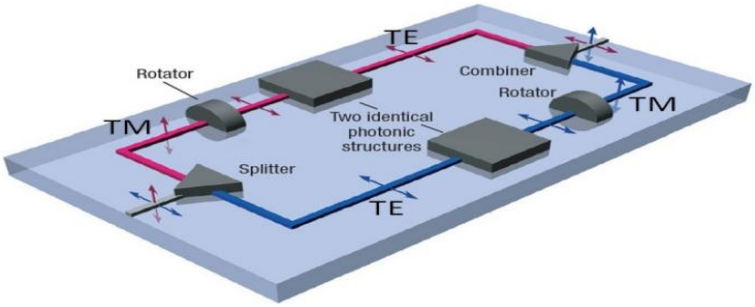

Fig. 4.3. A schematic of a polarization diversity system.(Copyright Nature Photonics, reproduce with permission after reference [82])

In polarization management systems, polarization rotators are the most important elements. As will be discussed more thoroughly in following section, polarization rotation is based on tilting the optical axis of the waveguide by introducing some kind of asymmetry and anisotropy. This tilt in optical axes will eventually cause a coupling between polarization states and changes the total polarization of the propagating light.

Polarization Rotators, PR[2], are categorized into active and passive devices. In active PRs, material anisotropy is introduced to induce coupling between different polarization modes. This is achieved by either electro-optic [83, 84] or photoelastic [85, 86] effects. On the other hand, passive PRs rely on asymmetric geometry. These components employ junctions, tapers, bends, steps or other discontinuities and asymmetries to eventuate power exchange between polarization states in the resulted hybrid mode [87]. Passive polarization rotators offer easier fabrication process compared with active ones and consequently have attracted more attention and are more commonly used.

Passive polarization rotation is either based on mode-coupling or mode-evolution. Mode-evolution devices use amorphous silicon or silicon nitride over layers to break the waveguide vertical symmetry [88-91]. In these devices the principal axis of the structure rotates together with the polarization state of the fundamental mode along the transition. These devices have widely attracted attention due to them allowing relaxed fabrication

[2] These devices basically perform a unitary transformation on Jonas space which contains rotations and much more. Although it can be considered to be a form of rotation on a complex 2D vector space as it preserves the inner product of any pair of vectors. A unitary transformation is equivalent to a rotation of the Stokes around Poincare sphere. Hence one can legitimately use the term “polarization rotator” in this context.

because of their robust fabrication tolerance and broad operation wavelength range. However, PRs based on mode-evolution are generally very long to be able to adiabatically couple modes and also require a rather complex fabrication.

Another category of PRs are mode-coupling structures. These devices are also fabricated such that they have tilted optical axes. Unlike mode evolution PRs, rotation between two polarization modes in this kind of PRs will happen after a significant length along the waveguide, which is determined by different parameters of waveguide geometry and light propagating through it. This will be discussed more thoroughly in following section. Therefore mode-coupling based structures are inherently wavelength dependent, and precisely tuned coupling and phase-matching are strongly sensitive to fabrication variations. The fact that makes these structures popular is that they are smaller compared to other types and are easier to fabricate. Here we concentrate on this kind of polarization rotators.

Different designs have been proposed to realize mode-coupling polarization rotation by introducing anisotropy in the waveguide geometry. Shani [92] was the first to report experimental demonstration of a PR using periodic asymmetric-loaded rib waveguides. Although at the time he could not give a rigorous explanation on why polarization rotates through the structure. Later on Haung and Mao[93] used coupled mode theory based on scalar modes to theoretically analyze the structure. They claimed the asymmetric loading of the waveguide in the design proposed, perturbs the axes of the primary waveguide. By alternating the loaded layer periodically in longitudinal direction, polarization rotation will be accumulated coherently until full conversion is achieved. Similarly cascaded bent sections [94,95] and periodic tilted waveguide sections [96] have been used for polarization rotation. However, due to the scattering and mode-mismatching at the junctions between sections the excess loss in these structures is large. Also, devices reported are too long and the design and fabrication are quite complex.

Recently, great efforts have been made to realize a simple polarization rotator with a single straight section [97–104]. In [97], a compact GaAs-AlGaAs polarization rotator is proposed using the reactive ion-etch lag effect. Angled InP-InGaAsIn waveguides also where used to design a polarization rotator (50 μm) with a low insertion loss (1 dB) [98].

In 2003 Chan and et al [102] introduced polarization rotation using SOI ridge waveguides with slanted sidewalls and several devices based on this structure were proposed [103,104]. However, they are as long as several hundred micrometers and the fabrication of such slanted side walls is obviously difficult [104].

The main property of single-section PRs is that in these structures, the asymmetric waveguide is optimized to have an optical axes tilted exactly 45°. Following we will discuss how this axis rotation yield to 90° rotation of polarization for TE-TM conversion in only one section.

4.4. Polarization Conversion

As discussed earlier TE and TM polarizations have different properties and several photonic systems are implemented to only operate in one polarization state. Therefor efficient TE-TM conversion is an essential requirement of PICs. Here we discuss the theory behind this conversion in single section mode- coupling based PRs.

Here a waveguide is assumed which has a geometrical anisotropy as it is in every passive polarization transformer structure. Different polarization states of the light travelling in such waveguide will realize different effective index as a result of propagating in a birefringent medium and hence will acquire different speeds. As a result of this difference, phases related to two orthogonal modes will evolve differently along the waveguide. Assuming the polarization of each wave to be along one of the principle directions of the medium, their polarization will not change during propagation. The difference in phase delay of the modes will be proportional to the propagation length, L, and to the difference propagation constants Δβ [105]

$$\Delta\varphi = \Delta\beta L$$

Equation 4.2

From this, it is anticipated that the phase relation between waves is restored after integer multiples of L_b the so-called polarization beat length:

$$L_b = \frac{2\pi}{(\beta_0 - \beta_1)}$$

Equation 4.3

Where β_0 and β_1 are the propagation constants of two modes. When the phase delay becomes ±180, the propagating distance is called the half-beat length, L_π which is:

$$L_\pi = \frac{L_b}{2} = \frac{\pi}{(\beta_0 - \beta_1)}$$

Equation 4.4

As illustrated in Fig. 4.4, a linearly-polarized light can be decomposed into two components along the fast & slow birefringence axes in the transverse plane. After the distance of a half-beat length, one component is out of phase by ±180 degrees compared to the other. Therefore, if a linearly-polarized light is launched into a longitudinally-invariant birefringent waveguide with an angle φ to one optical axis, after propagating a half-beat length, the output polarization makes an angle of $-\varphi$ with respect to the same axis,

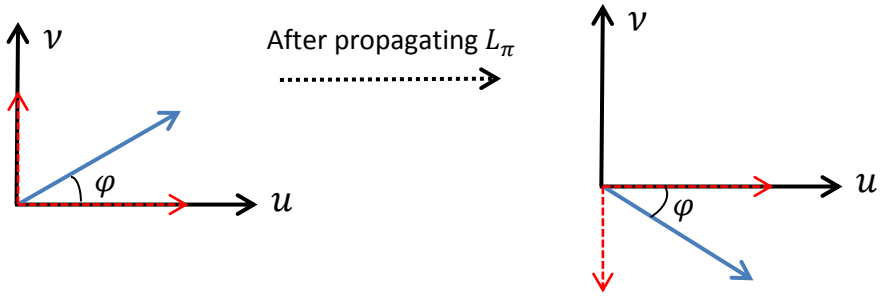

Fig. 4.4. Polarization conversion in a longitudinally- invariant birefringent waveguide after a half- beat length.

This property is used to convert two orthogonal modes into each other (e.g. TE and TM). In a structure with asymmetric cross section, the two lowest-order eigen-modes are hybridized and their electric and magnetic fields are tilted from the vertical axis due to the new boundary conditions in solving Maxwell's equations. For sake of simplicity we can also assume that the electric field of the TE and TM modes are still aligned in the x and y direction respectively but the optical axis has been rotated. In this case, with a proper optimization of the waveguide parameters and choosing the geometry and refractive index of the asymmetric waveguide, the optical axis can be tilted by ±45°.

Let us consider a light wave whose polarization is directed along the x-axis, i.e., TE mode, launched into the asymmetric waveguide section which is optimized to have an optical axis rotated 45° with respect to the x- and y- axis (x' and y'). Therefore the TE

mode will have an angle of $\varphi = 45°$ with respect to the optical axes. In this case, two eigen-modes are excited, and are propagated with different propagation constants, β1 and β2. After a propagation of a half beat-length, $L_\pi = \pi/(\beta 1-\beta 2)$, polarization will be rotated and the new angle will be equal to $\varphi = -45°$. Hence a total rotation of 90° is achieved, and thus the light polarization of output is along y- axis, i.e. TM mode. Fig. 4.5 illustrates this mechanism.

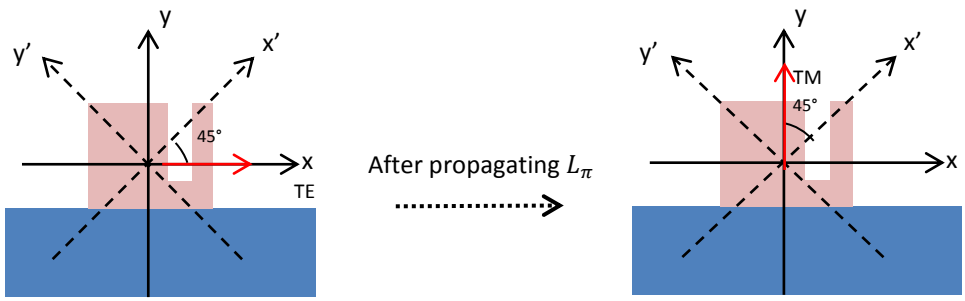

Fig. 4.5. TE to TM mode conversion in a longitudinally- invariant birefringent waveguide after a half- beat length.

In polarization rotation mechanisms, polarization conversion efficiency (PCE) is a crucial performance parameter which evaluates the efficiency of this phenomenon. For the TM to TE conversion, the polarization conversion efficiency can be defined as

$$PCE = \frac{P_{TE}^{out}}{P_{TM}^{out} + P_{TE}^{out}}$$

Equation 4.5

The extinction ratio also is expressed as:

$$ER = \frac{PCE}{1 - PCE}$$

Equation 4.6

Where P_{TM}^{out} and P_{TE}^{out} are the power of the output TM mode and the output TE, respectively, given a TM input.

So far we have discussed different approaches to polarization rotation in integrated photonic systems and introduced single section passive structures as the most promising design. Also the basics of polarization rotation in such structures were reviewed in depth.

Following the recent advancements in single section polarization transformers will be discussed which promise easy fabrication and high conversion efficiency.

4.5. Discussion

There has been much research around single section polarization rotators, but, as introduced earlier in this chapter, most of these reported polarization rotators use III–V semiconductors with thick substrates. As a result, the waveguide is single mode only over a small region of waveguide parameters and the radiation loss into the substrate is considerable resulting in significant coupling loss to singlemode fibers. In addition, in III–V technologies, because the waveguides lack very strong optical confinement, strong bending losses are expected which limits the minimum size of devices achievable and therefore restricts the component density in integrated platforms.

Silicon-on-Insulator (SOI) passive polarization rotators have been developed as an enhancement of this kind of devices. In this technology, a much stronger index contrast is used which leads to a decrease in the optical losses. Also, compared to III–V designs, SOI based polarization rotators provide less wavelength sensitivity as well as enhanced fabrication error tolerance [106]. Furthermore, they can be integrated with electronic components to enable large-scale, low-cost and high-density optoelectronic integrated circuits.

In 2008, Wang [107] proposed an ultra-small polarization rotator in order to achieve even higher integration density. This device is based on Si nanowires with an asymmetrical cross section with a cut corner which can be considered as a first order approximation of slanted walls already used in PRs. This design includes input and output sections based on a standard square SOI nanowire. In this design a vertical sidewall is used to make the asymmetry needed which can be fabricated by using simple dry etching process. Here the asymmetrical structure fully hybridizes the two lowest order modes, resulting in the high power conversion efficiency. Due to the specific asymmetry of the Si nanowire and strong confinement provided, the difference between propagation constant of these two modes is very large, which according to the equation for half-beat length, greatly reduce the conversion length.

$$L_\pi = \frac{2\pi}{(\beta_0 - \beta_1)}$$

Equation 4.7

Fig. 4.6 below shows the schematic of the reported polarization rotator including the standard rectangular Si nanowire as the input and output sections and the cross section of the nanowire, a corner of which is etched to provide the asymmetry for the purpose of polarization rotation.

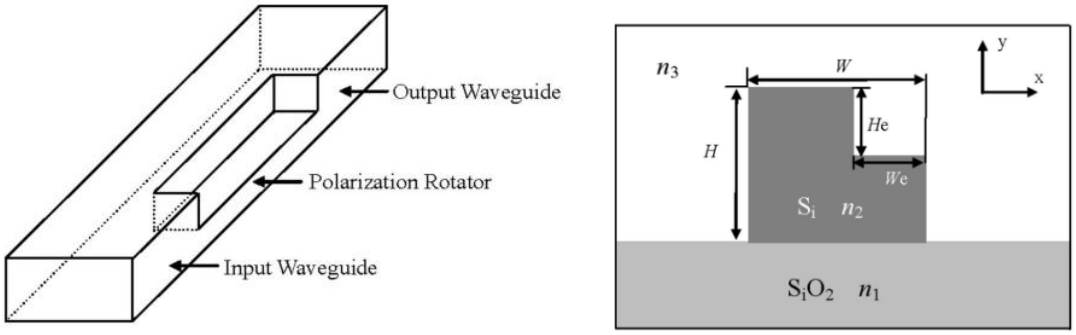

(a) (b)

Fig. 4.6. (a) Schematic of the reported polarization rotator. (b) Cross section of the polarization rotator section. (Copyright Optical Society of America 2008, reproduced with permission after reference [107])

Here we consider the case of the polarization conversion from TE to TM polarization. The PCE indicating the percentage of power transferred to the orthogonally polarized mode from the polarized input field can be expressed as follows for this asymmetric design [108]:

$$PCE = sin^2(2\theta) sin^2\left(\frac{\pi L}{2L_\pi}\right)$$

Equation 4.8

Where θ is the angle of optical axis rotation, L_π is the half-beat length and L is the actual length of the polarization rotation section. In a single-section rotator, the optical axis rotation angle must be equal to θ =45° in order to achieve a 100% polarization rotation after a length of L=L_π. Therefore the analysis of the optical axis and its rotation is very important for realizing a perfect polarization rotation. Several methods have been conducted to define the optical axes rotation angle, θ [109-111]. Here we use the following definition [109]

$$\tan(\theta) = R = \frac{\iint_{\Omega} n^2(x,y).H_x^2(x,y)dxdy}{\iint_{\Omega} n^2(x,y).H_y^2(x,y)dxdy}$$

Equation 4.9

Where R is the polarization rotation parameter, $H_x(x,y)$ and $H_y(x,y)$ are the transverse and horizontal components of an eigenmode respectively and n(x,y) is the refractive index distribution. Defining R_1 and R_2 as the rotation parameters for the two lowest order modes which are orthogonal it is easy to obtain,

$$\theta = tan^{-1}(R_1) = tan^{-1}\left(\frac{1}{R_2}\right)$$

Equation 4.10

By a careful choice of the waveguide parameters including the etching width W_e and etching height H_e, we can achieve R=1. Also appropriate refractive index of cladding must be chosen to achieve a larger difference $(\beta_0 - \beta_1)$ to have shorter conversion length. Here SiO2 cladding (n_3 =1.46) is used. Wang et al, have found the optimal etch parameters of We=240 nm and He=240 nm to have full conversion over a half-beat length of only 7.2 um. Our FDM calculations and retrieving the mode profile of the cross section verifies this claim.

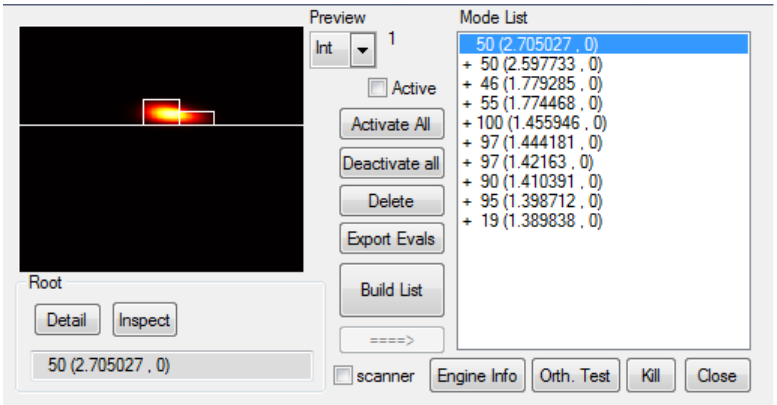

Fig. 4.7. Modes at the polarization conversion section in the Silicon nanowire, calculated by FDM

In the mode list provided by FimmWave for the asymmetric cross section, Fig. 4.7, one sees the properties of the first 10 modes calculated related to this design respectively from lowest order modes to the highest. Here the 0-100 numbers assigned to each mode provides a measure of their state of polarization, 0 being fully TM and 100 being full TE

polarized. Also values in parentheses represent the effective refractive index associate to the mode. As it can be seen, two fundamental modes calculated for the asymmetric section here have a polarization value of 50, showing a perfect hybridization of TE and TM mode for the geometrical parameters mentioned earlier.

The scattering matrix calculated for this design, allowing just two fundamental modes at the input, one TE and one TM, is:

$$\begin{bmatrix} TE_{in} \\ TM_{in} \end{bmatrix} = \begin{bmatrix} 0.003808281 & 0.69847 \\ 0.6983959 & 0.003986688 \end{bmatrix} \times \begin{bmatrix} TE_{out} \\ TM_{out} \end{bmatrix}$$

Which corresponds to a high PCE of 99.45 % for TE to TM conversion and 99.43% for TM to TE conversion.

However, the structure with parameters mentioned does not provide an acceptable fabrication tolerance due to the high index contrast of the cladding, SiO_2, and silicon. So another optimal design using SiN as the top cladding having larger refractive index, n_3=2.36 is proposed. Here, We=170 and He=280 nm is chosen not only to be the optimum etching profile to have an exact 45° rotation on optical axes but also to have a highest fabrication tolerance in such structures. Our mode calculation for this design, Fig 4.8, shows a perfect hybridization as well with fully hybridized fundamental modes.

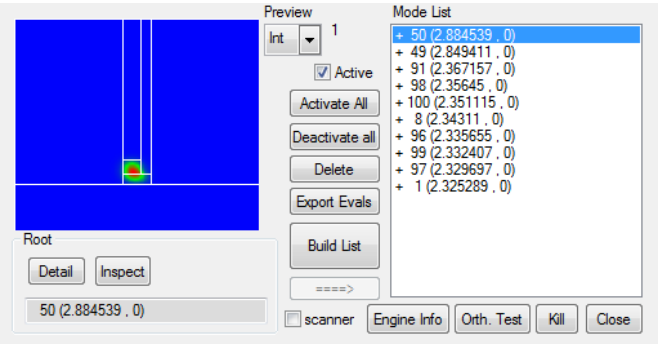

Fig. 4.8. Modes at the polarization conversion section in SiN nanowire, calculated by FDM.

The scattering matrix in this case is shown below which suggests a PCE of 99.98% for TE to TM conversion over a half-beat length of L_π=22.1um.

$$\begin{bmatrix} TE_{in} \\ TM_{in} \end{bmatrix} = \begin{bmatrix} 0.0001570853 & 0.8810423 \\ 0.8809698 & 0.000021626 \end{bmatrix} \times \begin{bmatrix} TE_{out} \\ TM_{out} \end{bmatrix}$$

Also 3D FTD is used to better show this conversion along the length of the device, Fig 4.9. At the input x-polarized beam is launched, TE, and y- polarized beam, TM, is produced over the length of the device.

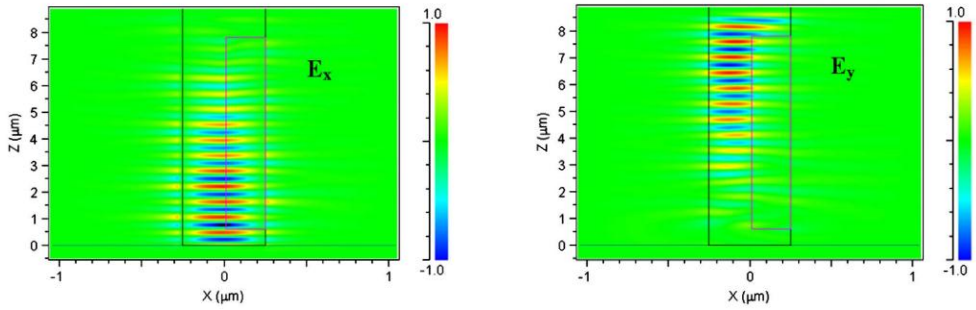

Fig. 4.9. E_x and E_y in the polarization conversion section. (Copyright Optical Society of America 2008, reproduced with permission after reference [107])

This successful and promising design for polarization rotator has attracted considerable attention. Alonso[112] in 2012 proposed a polarization rotator based on this stepped waveguide concept compatible with InP technology. The design proposed by Wang could not be directly applied to this technology due to high insertion loss produced by butt coupling between interconnection waveguides and the rotator section in InP substrates which is a result of the lower index contrast of this technology and its larger dimensions. Alonso proposed to implement an adiabatically transition between different sections using tapers to reduce insertion loss considerably. The complete device is shown in Fig. 4. 10, including the cross section views of all the waveguide.

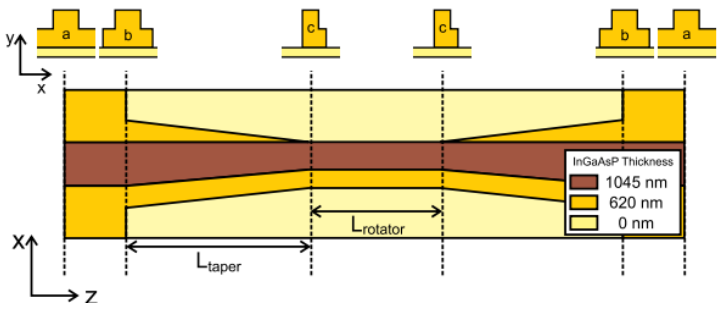

Fig. 4.10. Schematic of the InP based single section stepped waveguide, including cross section views of all the waveguide sections. (Copyright Optical Society of America 2012, reproduced with permission after reference [112])

The added tapers are to make the transition between two sections transparent to the fundamental mode of waveguide. They have to fulfill two different tasks: minimize insertion loss and make the rotation between the fundamental (TE or TM) modes to the hybrid modes in the stepped waveguide section. A taper length of L_{taper} =70μm is calculated to be enough to obtain the desired performance.

Polarization rotator proposed for compatibility with an InP based receiver [113] with H=1.45um and h=0.620 um has been found to have optimum dimensions of X_b =1220nm, X_c =530nm, $L_{rotator}$ =784μm, $L_{taper=}$70μm. Owing to the thick cladding and half-ridge structure, the modes travelling from the rotator section to the output, have large overlap with TE and TM modes of a symmetric ridge waveguide, which allows low-loss integration of the proposed structure into the standard ridge InP PIC.

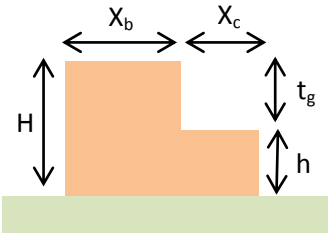

Fig. 4.11. The cross section of polarization conversion section.

It is also noted that in the tapers there will be small phase shift between hybrid modes which can be compensated by optimizing the length of the rotator waveguide. As a result the length of the rotator is slightly shorter than the half-beat. In this paper an ER of 40 dB corresponding to PCE of 97.5% is calculated with insertion loss of 0.04 dB at a wavelength of 1550 nm over a length of 924 um for the whole device.

I have tried to reproduce this proposed structure using FimmWave. The exact refractive indices are not mentioned in the paper hence InP and InGaAsP libraries of the simulation tool are used. Although an InP cladding layer is not mentioned in this paper, our results show that, without this layer this rotation is not possible. Our simulations with FimmWave show that without including the cladding layer hybridization of TE/TM does not happen. Here is the mode list for the structure with details provided in the paper,

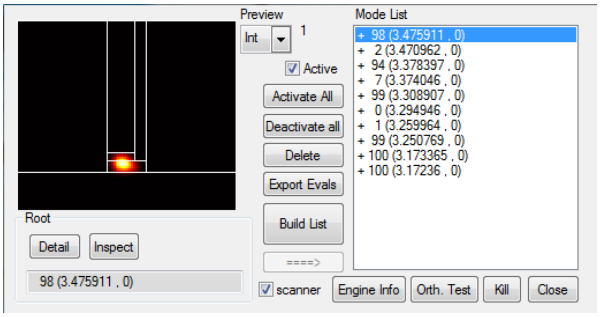

Fig. 4.12. Modes at the polarization conversion section of the InP based polarization rotator without an upper cladding, calculated by FDM.

which as can be seen, TE mode is dominant and hybrid mode is not achieved. While by including the upper cladding of InP a hybrid mode as below will be obtained:

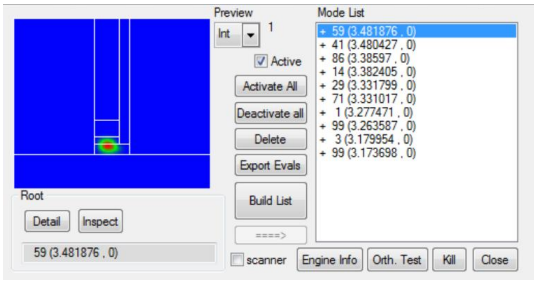

Fig. 4.13. Modes at the polarization conversion section of the InP based polarization rotator with an upper cladding, calculated by FDM.

In 2013 Tanemura et al[114], publish their experimental results from fabrication of a simple and compact InP polarization rotator based on a stepped-waveguide.

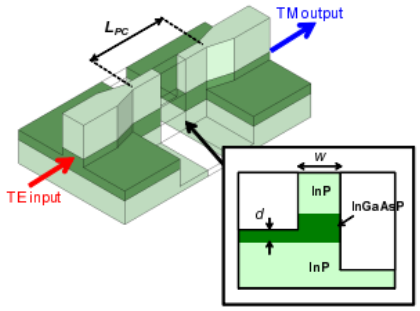

Fig. 4.14. Schematic of the reported compact polarization rotator structure on InP and the cross section view at the polarization rotation section. (Copyright Optical Society of America 2013, reproduced with permission after reference [114])

This structure has a shallow-etched ridge structure on the one side and a deep-etched high-mesa structure on the other. This design fabricated in 2013 promises a conversion of 96% over just 150 um long device. Here is the mode list of the rotator section based on the parameters presented by this paper:

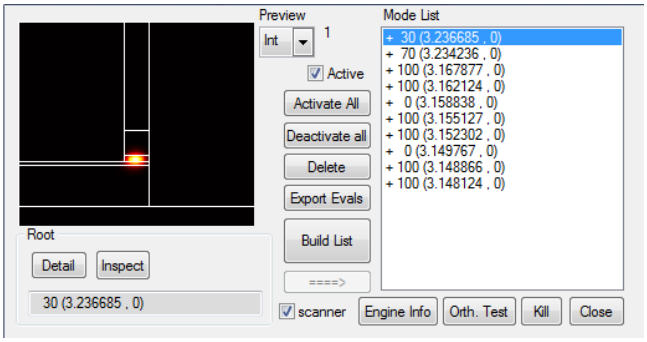

Fig. 4.15. Modes at the polarization rotation section of the InP based polarization rotator, calculated by FDM.

As can be seen, the hybridization cannot be observed with the design parameters and a perfectly etched corner waveguide as the polarization rotator. Based on the measurements and analysis performed on the fabricated device, it is reported that the shallow etching in the rotator section is not perfect and a residue will be remained acting like a slanted wall with an angle of 54.7°.

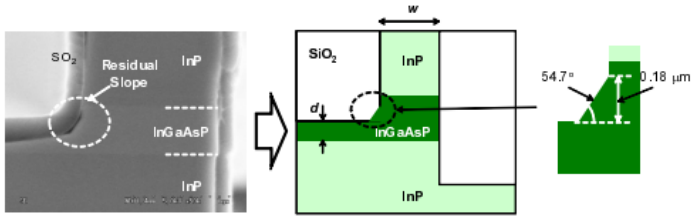

Fig. 4.16. Actual structure of the fabricated device (left) and the cross section view of the structure assumed in the simulation reflecting the actual structure (right). (Copyright Optical Society of America 2013, reproduced with permission after reference [114])

Adding this defect to the simulation structure one achieves a more promising mode list with modes closer to TE/TM hybrid modes.

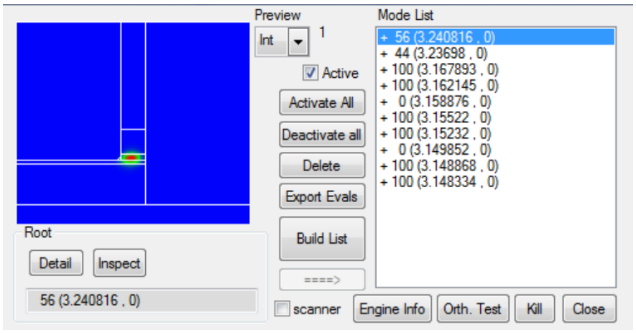

Fig. 4.17. Modes at the polarization rotation section of the InP based polarization rotator accounting for the fabrication defect, calculated by FDM.

This structure although promises a more compact device than Alonso's, but its functionality relies on a fabrication defect of arguable reproducibility.

Aside from PRs, polarization rotator and splitters (PSR) are also useful in photonic circuits. When a photonic chip which only supports one polarization, is coupled to a SMF fiber which does not have a certain polarization, a PSR is required to split TE modes from TM modes, and convert all the modes to the operating mode of the chip. Several PSRs have been reported, including structures based on multi-mode interference [115], directional couplers [116-119], and a polarization splitter followed by rotator [120].

Xiong[121] proposes a polarization rotator and splitter (PSR) based on tapered etched directional coupler. In his paper, Xiong proposes a fabrication tolerant and broadband structure based on mode-coupling mechanism. Fig 4.18 shows a schematic of the proposed design. It includes a silicon wire waveguide (A) having a width W and height H, adjacent to a taper-etched waveguide(B)with a width W_t, a ridge width W_e, a post-etch slab height H_e , a taper angle θ, and a gap between the waveguides D_{gap}. The coupling length L_{DC} is the taper length in the waveguide B, where

$$L_{DC} = \frac{W_t}{\tan(\theta)}$$

Equation 4.11

In the proposed design for a PSR the dimensions of the waveguide B have to meet two conditions. Firstly the index mismatch of TE-like mode for two waveguides must be large enough to guarantee that the TE mode in waveguide A will have minimal coupling to the waveguide B i.e. $n_{eff}^{B}(TE) < n_{eff}^{A}(TE)$. Secondly the phase matching condition of

$n_{eff}^{B}(TE) \sim n_{eff}^{A}(TM)$ must be met in order to have coupling between the TM-like mode injected waveguide A and TE-like mode of waveguide B. the hybrid mode supported in asymmetric tapered-etch waveguide B will facilitate this coupling process. If these conditions are met, a high TM to TE conversion can be achieved.

In the structure proposed, a silicon core refractive index of n_{si} = 3.476 and upper and lower SiO_2 cladding with a refractive index n_{SiO2}= 1.444 is assumed. The thickness and width of the waveguides are also similar to the standard silicon photonic feature size, H = 220nm and is W = 450 nm. Also the gap between two waveguides in the coupling section is D_{gap}= 200 nm.

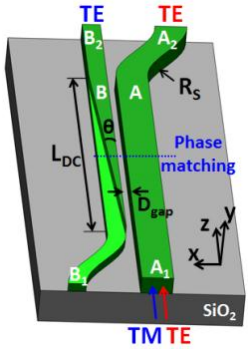

Fig. 4.18. Schematic of the proposed polarization splitter and rotator. (Copyright Optical Society of America 2013, reproduced with permission after reference [121])

Our FDM simulation of this structure agrees perfectly with 3D-FTDT simulations reported in the paper. As can be deducted from the scattering matrix calculated, when a TE mode is launched from port A_1, it will exit the same waveguide from port A_2 (98%) with minimal coupling to waveguide B. On the other hand, Fig 4.19 shows how the TM mode launched to waveguide A, will couple to the other waveguide in phase matching region and converted to TE mode by through the output port. Also from scattering matrix can be seen that the TM mode from port A_1 will end up exiting from as TE mode from B_2 (93%).

$$\begin{bmatrix} TE_{A1} \\ TM_{A1} \end{bmatrix} = \begin{bmatrix} 0.0017 & 3.9e-6 & 0.98 & 4.3e-6 \\ 0.93 & 0.0001 & 0.0001 & 0.01 \end{bmatrix} \times \begin{bmatrix} TE_{B2} \\ TM_{B2} \\ TE_{A2} \\ TM_{A2} \end{bmatrix}$$

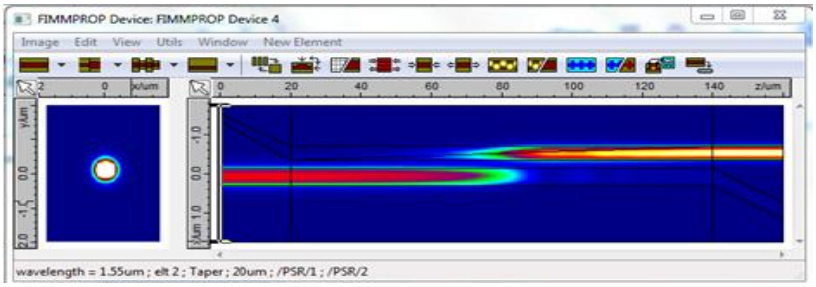

Fig. 4.19. TM-like mode propagation and conversion to TE-like along the proposed polarization splitter and rotator.

The performance of polarization rotators based on mode coupling highly depends on accurate geometrical dimensions and hence show poor robustness to fabrication inaccuracies. Xiong [121] , promises a large fabrication tolerance for this PSR based on mode coupling and has reported some experiments indicating this feature of the structure. Fig 4.20.a represents the dependency of conversion efficiency on the tip width, D_t, from 0 to 120 nm, showing a high fabrication tolerance for this design. Looking into this property of the design for height of 110 nm (green line in the reported diagram), one may change this D_t from 0 to its maximum which is half the width of the waveguide, 170 nm. Calculating conversion efficiency of the structure at each point, it is clear at Fig 4.20.b that the results are not as predicted as the reported figure. As it can be seen, unlike the interpretation one might get from the reported figure, after about 100 nm a drastic change in conversion efficiency will happen and therefore a lack of fabrication tolerance.

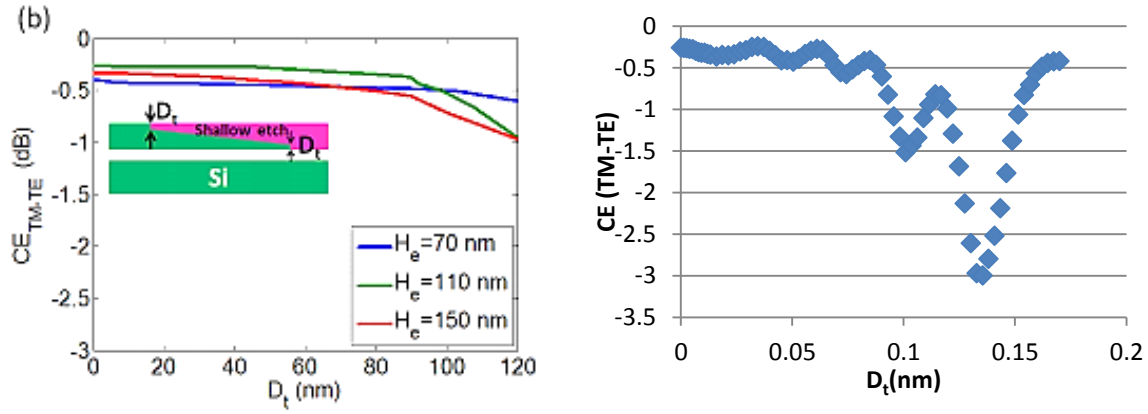

Fig. 4.20. Dependence of the polarization conversion efficiency on the taper tip width for H_e= 110 nm, calculated using the full-vectorial EME simulations. (Copyright Optical Society of America 2013, reproduced with permission after reference [121]) (left) and calculated using FimmWave (right)

4.6. Summary

In this chapter polarization management in photonic integrated circuits was discussed. Considering polarization sensitive PICs, the randomly polarized light from optical fibers or imperfectly fabricated ridge waveguides must go through polarization management systems first to be able to be further processed by other devices. Here polarization rotators as the essential elements of such systems were introduced and different categories were discussed. A critical appraisal of various approaches regarding design of such structures was presented along with validation of most promising methods by reproducing the results using simulation tools. Furthermore inaccuracy and incorrectness of some reported methods was pointed out and accordingly corrected.

Here, more specifically, Single- section PRs based on stepped waveguide was introduced as the most recent advancement in this area promising more compact devices with much easier fabrication and higher fabrication tolerance. Implementing these devices in SOI and InP technology was discussed and performance of the structures reported in literature was analyzed using FimmWave. Finally a polarization rotator and splitter based on the same concept was introduced. Performance of the design and fabrication tolerance of the reported structure was critically analyzed.

Chapter 5. Fiber to Chip Coupling

5.1. Introduction

Standard single mode strip waveguides on SOI are typically fabricated 500 nm wide and 220 nm thick. In such substrates the high refractive index contrast between silicon as the core and silica as the cladding provides strong light confinement in cores which have geometries that are in order of fractions of the propagating light wavelength. This tight confinement comes very beneficial, resulting in bending radiuses of a few microns which makes high integration density and ultimately lower costs possible.

On the other hand standard single mode optical fibers (SMF) currently used in the backbone of modern communication systems, have a much larger size compared to this nano-scaled waveguides. A typical core of a SMF has a diameter of 8 um and a cladding diameter of 125 um. Furthermore comparing to the high refractive index of the core and cladding of SOI waveguides, optical fibers have very low index different of only 0.01 which results in the bending radius of about several centimeters.

Fig. 5.1 well illustrates this difference in geometries of these two kinds of waveguide. The cross-section of an optical fiber is more than 100 times larger than that of a SOI nano-scaled waveguide. This difference will cause a huge mismatch between their guided mode profiles including their size, shape, and the velocity at which the modes propagate which makes coupling light from one to another a very challenging issue. Normally a direct butt coupling between a singlemode fiber and a nano-scaled waveguide leads to more than 20 dB insertion loss. This insertion loss is definitively a big obstacle to wide spread use of nano-photonic chips in communication systems since it is directly related to other performances such as the signaling rate, link reach, receiver sensitivity, etc. Hence much effort has been carried out to come up with a coupling structure to adapt the mode profiles of the SOI waveguides and optical fibers to improve this coupling loss.

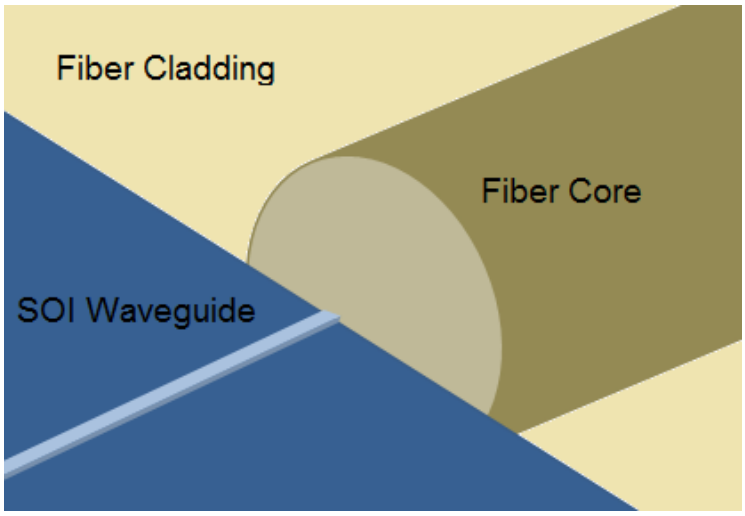

Fig. 5.1. Schematic of direct butt coupling of a nano-scaled waveguide to a standard single mode fiber.

In the following chapter, firstly different approaches towards solving the fiber-to-chip coupling will be discussed and advantage and disadvantage of each one will be argued. Then recent advances in this area will be reviewed which at last results in introducing a novel approach to handle this issue.

5.2. Fiber-to-chip coupling loss and solutions

Coupling loss can be theoretically calculated using overlap integrals of the fundamental mode profiles of two waveguides as below [122]:

$$L = -20\ log_{10} \frac{\iint_{-\infty}^{\infty} F_1 F_2 dxdy}{\sqrt{\iint_{-\infty}^{\infty} |F_1|^2 dxdy}\ \sqrt{\iint_{-\infty}^{\infty} |F_2|^2 dxdy}}$$

Equation 5.1

Where $F_1(x, y)$ and $F_2(x, y)$ are the fundamental mode profiles of the SOI waveguide and the optical fiber respectively. It must be noted that these mode profiles vary with wavelength, which at the end results in bandwidth limitation of fiber to chip coupling.

Considering many structures proposed to improve the fiber-to-chip coupling loss it is important to notice that a promising design must be compatible with FTTH or

wavelength division multiplexing (WDM) applications hence it is required for the coupler to be broadband and polarization insensitive. Also considering the cost, the footprint of a coupling design must be reasonably small and have an adequate alignment tolerance.

A common solution to the mode mismatch at fiber and chip interface is to use lensed [123-124] or tapered [125] fibers to reduce the spot size of the mode at the fiber front. Lensed optical fibers can focus light into smaller mode field diameters of about 2.5 um where this value is about 0.8 um in case of tapered fibers at wavelength of 1.55 um. However these types of fibers are not considered as standard and are not commonly used in mass telecommunication industry.

Alternatively much effort has been made to come up with designs to adapt the mode at the silicon waveguide front. To do that two main approaches have been presented in literature, depending on the direction in which the fiber is coupled to the chip; surface and edge coupling techniques. Following we will review each approach in depth and the theory behind each one of them and discuss pros and cons of each method when compared to each other.

5.3. Surface Coupling

In this type of coupling typically the fiber is embedded perpendicular or near perpendicular to the chip surface. On the surface of the chip optical gratings are used to diffract the out of the plane light injection from the optical fiber to in plane light propagation guided by the planar waveguide core. The gratings used follow the rules of lamellar gratings discussed in depth in chapter 2 and are responsible to convert the fiber modes to planar waveguide modes. A simple grating coupler, structured by periodic grooves etched onto a silicon waveguide, is shown schematically in Fig. 5.2.

As discussed in earlier chapters, the light injected from the optical fiber to the gratings will be diffracted by the grooves into all directions, but at certain directions the plane waves will add up constructively or destructively which leads to minimum and maximum diffraction intensities respectively. These diffractions can be tuned by controlling the periods of the gratings. When the second order gratings are considered light coming from

the waveguide towards the grating will be diffracted perpendicular to the chip surface as well as feed-forward and feed-back reflections. These reflections are unwanted and desired to be avoided. Hence instead of a perfectly perpendicular launching of light from the fiber, larger grating periods will be used so that the out-of-plane diffraction of light will have almost 10º with respect to the normal of the surface which at the end suppresses those unwanted reflections greatly.

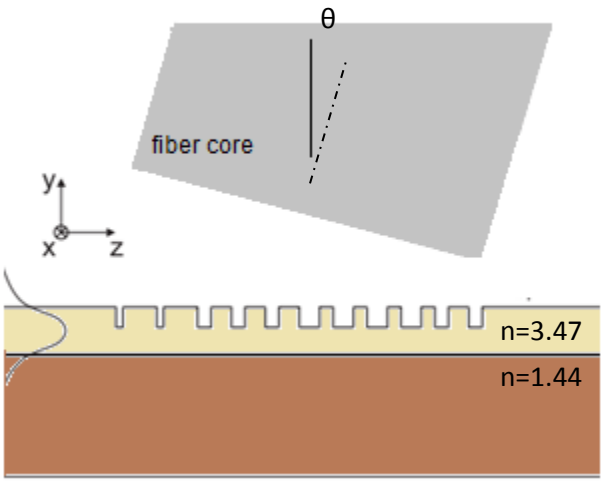

Fig. 5.2. Schematic of a simple surface coupler realized by gratings etched onto a silicon waveguide.

Grating couplers are typically followed by waveguide tapers to inject the light to the SOI waveguide [126] or are designed as self-focusing structure [127]. Although these both approaches have improved a lot during years to better efficiency and also easier fabrications [128-130], these designs still will not be considered as the ultimate choice as they have a very low bandwidth. As can be deducted by the basis of functionality of such structures, the grating periods are set to diffract certain wavelengths and will not work under different light waves with different wavelengths while wavelength transparency and insensitivity is desired in nowadays telecommunication to realize faster systems.

5.4. Edge Coupling

Another approach to coupling optical fibers to planar chips is through edge coupling. Here tapered or lensed fibers are coupled to the edge of the SOI chip, where the injected light to the silicon waveguide goes through spot size converters realized by different methods.

The coupling efficiency is formulated approximately as below [131]:

$$\eta = \left(\frac{2w_f w_w}{w_f^2 + w_w^2}\right)^2$$

Equation 5.2

Where w_f and w_w are the mode diameters of the fiber and the planar waveguide respectively. Clearly if these two values are equal we will have 100% efficiency. Hence a better coupling efficiency can be obtained when the mode diameters of both waveguides match regardless of the geometries of the physical waveguides which can be done by reducing the mode field diameter (MFD) of the modes at the fiber front e.g. using lensed and tapered fibers, or expanding the modes in non-scaled cores of the SOI waveguides.

Mode expansion at the planar waveguide can be done by means of varying the width of the waveguide in form of tapers [132-135] or inverse tapers [136-137]. In case of tapers, adiabatic broadening of the width of the waveguide results in higher effective index for the modes and hence flat expanded modes to match to the wide modes of the optical fiber with large diameters as in Fig 5.3.c. On the other hand, in invers tapers the width of the silicon waveguide is reduced gradually to sharp tips at the fiber interface to decrease the effective index of the mode close to the cladding index and at the end matching to the low effective refractive index realized by the mode at the optical fiber as shown in Fig 5.3.b.

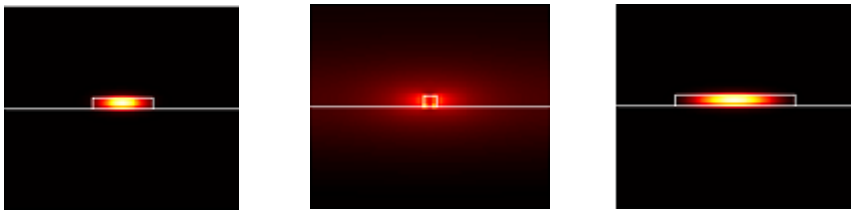

(a) (b) (c)

Fig. 5.3. The fundamental mode profiles at the silicon core, 220 nm thick and (a) 500 nm wide, (b) 100 nm wide and (c) 1 um wide.

It is important to notice that in both cases, the change to the width of the waveguide must be adiabatic. An adiabatic process is a process in which the variation is so slow that no transitions happen between energy levels. In an adiabatic inverse taper coupler as an

example, the change of the width is sufficiently gradual that the occupation of the modes do not change as the shape of the waveguide goes through changes and if only the fundamental mode is excited initially, all the power stays in the same mode while its shape keeps changing throughout the inverse taper and there will be no power coupled to other modes or radiated. This kind of couplers, as opposed to directional couplers working with half-beat lengths, discussed in chapter 4, do not need a critical length and have very low polarization and wavelength dependency. Although to achieve high efficiencies, these devices must be long enough which makes them longer than their counterparts.

In inverse tapers, due to the very narrow tips at the fiber interface the mode is released from the core and expands to the cladding. In such structures modes at the sharp tips are delocalized from the silicon core in lateral and vertical direction and thus produce a larger MFD. Hence another low index contrast waveguide must be embedded at the tip so it can capture the released and expanded mode. Typically it is realized by having a coating of polymer on top of the silicon core. [138-139] In this case when the light launches from the fiber to the silicon chip, it first will be virtually coupled to the intermediate waveguide with a mode size and refractive index matching that of the fiber. Then an inverse silicon taper will be introduced inside this low index waveguide which adiabatically widens till the fundamental mode is strongly confined inside the core.

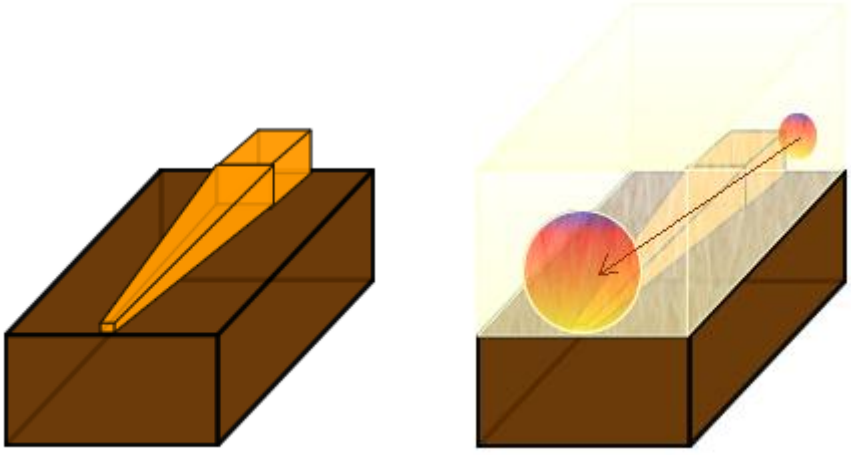

Fig. 5.4. Schematic of an inverse taper edge coupler and polymer top cladding to capture expanded low refractive index mode at the tip.

At the beginning inverse tapers were used for coupling light between semiconductor lasers and fibers [139], and later the same approach was exploited to Si waveguides [140-144]. Shoji et al [140] first achieved a coupling loss of 0.8 dB between a fiber with a mode diameter of 4.3um and a 0.3 × 0.3um silicon waveguide. Later on this loss was reported to be reduced to 0.5 dB by using a better material as the low index waveguide [141]. The total insertion loss of these devices was around 3.5 dB and were more than 200 um long. Then McNab et al [138] reported a coupling loss of more than 1 between a micro lensed fiber with 2.1um beam diameter and a 0.45x0.22 um Si waveguide which is closer to typical silicon waveguides geometry with 150um inverse taper length. It is also noticeable that the measurement uncertainty was reported to be 0.8dB. On the other hand Almeida et al [142] reported a compact 40um-long inverse taper with parabolic width profile which theoretically had coupling loss of about 0.5dB but only for the TE mode. In this case since the inverse taper did not have low index waveguide on top of the silicon core, high efficiency could not be achieved for TE and TM modes simultaneously. The insertion loss measured from experiments for a fiber with 5um MFD was 3.3dB for TE and 6.0dB for TM modes.

5.5. Comparison of edge and surface coupling

To be able to find an efficient approach towards the important issue of fiber-to-chip coupling it is important to compare the approaches in hand to evaluate their functionality in future systems. As discussed earlier although for the case of edge couplers typically a taper or lensed fiber is used, grating couplers are compatible with standard singlemode fibers so the loss of such non-standard fibers will be reduced. Also such kind of couplers do not require polished facets and they can be mounted in any arbitrary part of the chip and are suitable for wafer-scale testing and packaging which makes them a flexible and cheap choice. However, in case of edge couplers, the tapers or inverse tapers must terminate on diced and well-polished edges while generally the guard areas are reserved for possible damages to the integrated circuits on the die. This added process brings extra cost and complexity of testing and packaging. Also this extension of the waveguides all the way to the edge of the die introduces unnecessary propagation loss.

On the other hand, considering how diffracting grating couplers work and the relation between their period and the propagating light wavelength, these kinds of couplers are strongly wavelength dependent in a way that a 3dB bandwidth is only 50-60 nm, while a coupler covering the C-band is preferable. Edge coupling structures, on the other hand, present a much larger bandwidth, higher efficiencies and lower polarization dependent losses.

Taking advancements of edge couplers into consideration as the more promising approach, following the most efficient techniques to increase the efficiency of edge couplers and also decrease the fabrication complexity is discussed. Each method is simulated using simulation tools and reported results will be reproduced using FimmWave. At the end results of all approaches will be compared.

5.6. Discussion

The bottom line in inverse taper couplers is to reduce width of the waveguide gradually resulting in decreasing the effective index of the mode so that the effective area of the fundamental mode increases and matches that of the fiber. In an inverse taper, when the plane waves are propagated from the nano-scaled silicon waveguide, the area of the mode will expand gradually while it goes through width narrowing till it becomes very large and releases from the core. However the problem in fabrication these couplers is that to have a very low insertion loss we have to have very tiny waveguide tips below 100 nm at the interface of fiber and chip edge which is a very difficult task considering the imposed minimum features of fabrication tools. Although realizing such structures seems to be easy using e-beam lithography, but UV lithography which is already available for CMOS technology does not allow such tiny features. Several methods have been proposed to overcome these limitations and here we will review several of them.

5.6.1. Spacer layer

Beats et al in 2005 have tried to overcome the fabrication limitations of realizing tiny taper tips for inverse taper couplers [143]. In his paper he has made the low index waveguide spot size convertor concept compatible to conventional UV lithography by introducing a spacer layer between the taper and the polymer waveguide.

In this design the silicon core has a thickness of 220 nm and the polymer waveguide is realized by core dimensions of 3×3 um with a refractive index of 1.67. A top cladding of benzocyclobutene (BCB) with refractive index of 1.54 is also assumed. Here he suggests that adding a spacer layer from the low index BCB between the polymer waveguide and silicon core would increase the efficiency while the new structure is compatible with minimum features of 248 UV lithography.

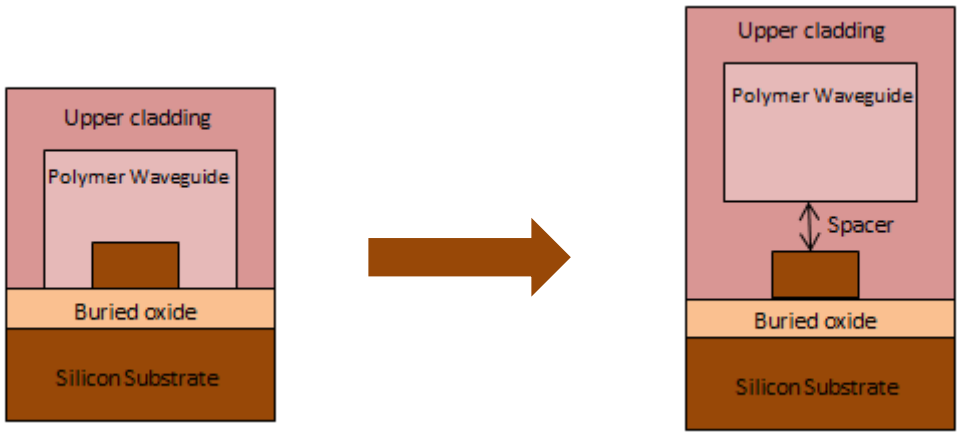

Fig. 5.5. Schematic of the cross-section of the modified structure including a spacer layer between core and polymer waveguide.

The device Baets proposes is shown in Fig.5.6. As can be seen we have 220 nm high core with a width of 590 nm buried in a BCB cladding of refractive index 1.54. The thick ness of the layer on top of the core is optimized to be equal to 200 nm. At the end on the top we will have a layer of doped BCB with refractive index of 1.64. Going through the inverse taper, the core size first reduces to 390 nm in 25 um and then goes from 390 to 175 nm in 175 um of length.

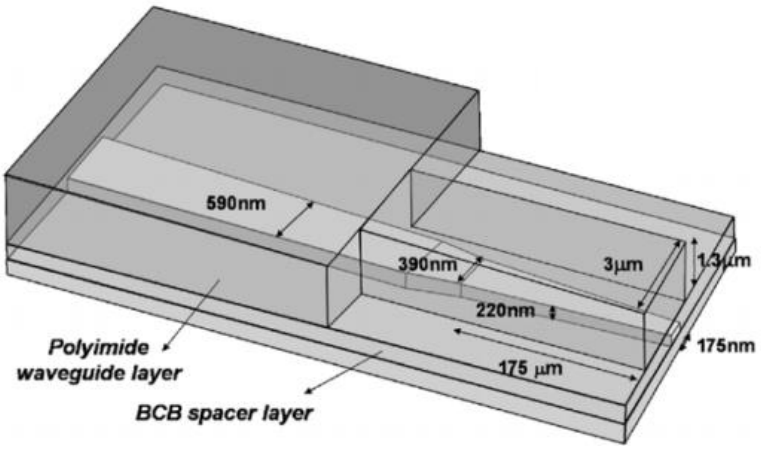

Fig. 5.6. Schematic of the proposed SOI spot size convertor for edge coupling. (Copyright IEEE 2005, reproduced with permission after reference [143])

Taking a look at the mode profiles at the two ends of the taper, it is explicit that the mode is strongly confined in the silicon core at one end but will gradually move up to the low index polymer waveguide at the other end which is the coupling edge to the lensed fiber, as can be seen in the mode profiles calculated by FimmWave. The effective refractive index of the mode in this structure will change from 2.57 to 1.62 through this transition.

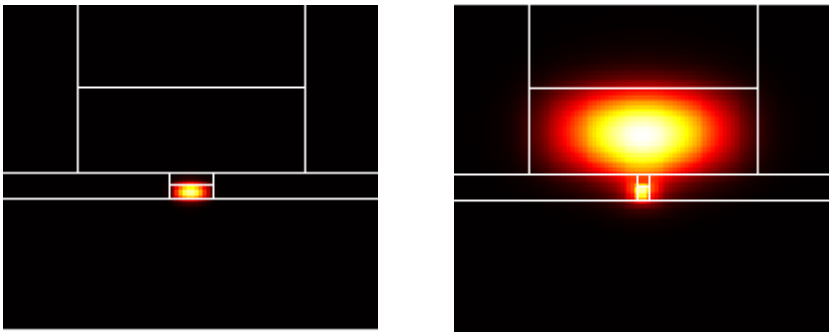

Fig. 5.7. Mode profiles of the taper at the silicon waveguide end (left) and at the fiber interface (right), simulated by Fimmwave.

Studying the light propagation through this structure and coupling to a lensed fiber with a Gaussian field diameter of 5 um as reported, following result is calculated by EME.

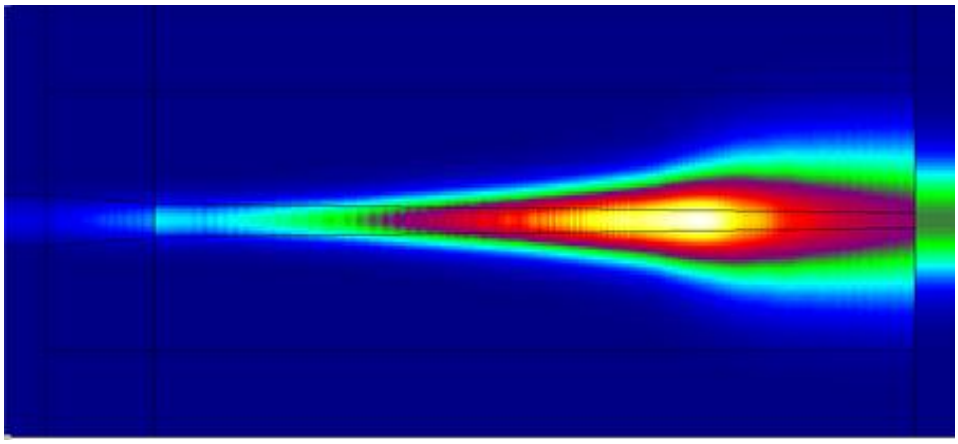

Fig. 5.8. Light propagation in the spot size converter proposed by Baets simulated by FimmProp.

As can be seen the mode expands gradually as the core width decreases and the mode moves up to the low index polymer waveguide and at the end goes through the lensed fiber. The scattering matrix calculated by EME method is as follows.

$$\begin{bmatrix} TE_{in} \\ TM_{in} \end{bmatrix} = \begin{bmatrix} 0 & 0 \\ 0.722 & 0 \end{bmatrix} \times \begin{bmatrix} TE_{out} \\ TM_{out} \end{bmatrix}$$

It is obvious that 72% of the TE mode is transferred from the waveguide to the lensed fiber which corresponds to a insersion loss of about 1.4 dB. But also it must be considered that lensed fibers have a 0.5 dB inherent loss which brings the whole device insertionl loss to around 1.9 dB which matches the value reported by Baets.

In the meanwhile no TM mode coupling is witnessed through this structure. Since edge couplers require very narrow taper tips for TM cupling, this structure is only optimizaed for TE coupling. Realizing very narrow taper tips is a difficult task; first of all it cannot be performed by UV lithography and also it will be very fragile due to its high aspect ratio. However many devices perform more efficiently under TM polarization and even some of them only work for TM mode [144-146]. So it is necessary to come up with a solution that shows good efficiencies for both polarizations.

5.6.2. Thermal Oxidization

Pu et al in 2010, on the other hand introduced a fabrication trick to be able to obtain very tiny (down to 10 um) waveguide tips [147]. In this paper, such an inverted taper coupler is optimized for both TM and TE modes.

In this report, an inverse taper starting form 480 nm with a reasonably narrow tip of 40 nm is first fabricated using e-beam lithography. The silicon thickness and taper length is considered to be 250 nm and 300 um respectively. Then the tip width is reduced by thermal oxidation. In this process of thermal oxidization, a 30 nm thick silicon dioxide layer is formed around the silicon core which means decreasing the dimensions of the core to a width of about 452 to 12 nm and thickness of 238 nm. In this way not only a very narrow taper tip is realized but also the silica cladding layer grown at this stage protects the tip during post fabrication processes. The structure is at last coated with a top cladding of SU8 with a cross section matching the access fiber.

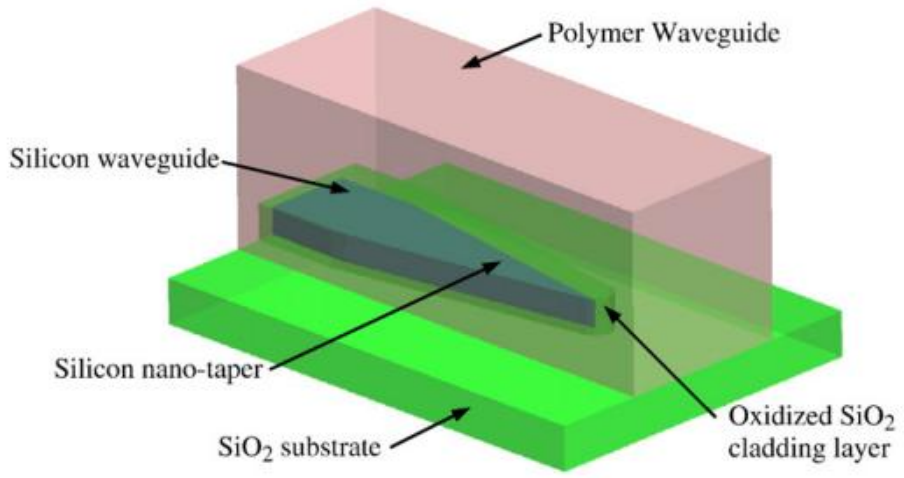

Fig. 5.9. Schematic of the device proposed by Pu for edge coupling. (Copyright Elsevier B.V. 2010, reproduced with permission after reference [147])

Studying this structure using FimmWave simulation tool, following results are obtained for the mode profiles at two ends of the taper. As predicted the mode is strongly confined in the silicon core at the beginning but it has moved up to the polymer waveguide near the fiber interface. The refractive index of the mode has gradually decreased from 2.52 to 1.53 through 300 um of adiabatic tapering.

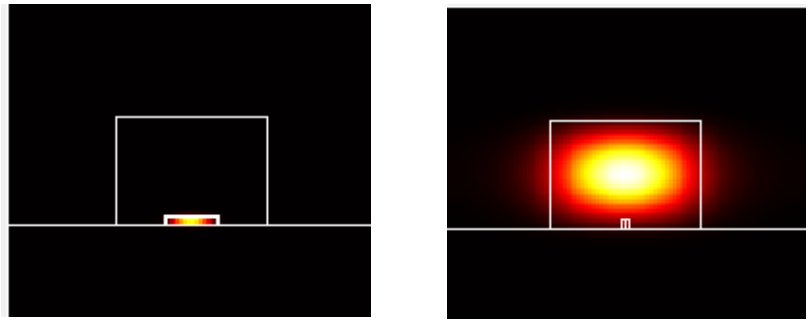

Fig. 5.10. Mode profiles of the inverse taper proposed by Pu at the silicon waveguide end (left) and at the fiber interface (right), Simulated with Fimmwave.

Also simulating the light propagation in such structure, and coupling to a fiber with MFD of 2.9 um following scattering matrix is calculated:

$$\begin{bmatrix} TE_{in} \\ TM_{in} \end{bmatrix} = \begin{bmatrix} 0 & 0.77 \\ 0.73 & 0 \end{bmatrix} \times \begin{bmatrix} TE_{out} \\ TM_{out} \end{bmatrix}$$

As can be seen there is a coupling loss of 1.2 dB for TE and 1.1 dB for TM in this device. Although this structure seems to be very promising but still it only can be realized with e-beam lithography and lensed fibers and cannot be considered in mass production using typical CMOS technology fabrication instruments.

5.6.3. Sub-wavelength gratings

Cheben et al on the other hand offers a totally different approach to go around the fabrication restrictions in case of fiber to chip coupling [148]. He suggests a structure that not only relies on decreasing the width of the waveguide for reducing the refractive index, but also introducing sub-wavelength grating so that based on effective medium theory [149] the effective refractive index realized by the mode can be changed by changing different properties of such structures such as the duty cycle or the pitch. In this design the period of the gratings must be chosen smaller than a half of effective wavelength to stay in the sub-wavelength domain. A SEM image of the structure fabricated can be seen in Fig.5.11. By this approach and mixing refractive indices of Si and SU-8 upper cladding at the sub-wavelength scale, the effective refractive index of the core can be varied in a range of 1.6 to 3.5.

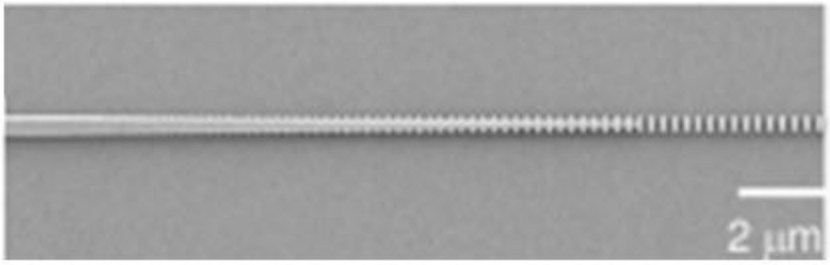

Fig. 5.11. SEM image of the edge coupler based on sub-wavelength gratings proposed by Cheben. (Copyright Optical Society of America 2010, reproduced with permission after reference [148])

This structure is comprised of arrays of rectangular 260 nm thick silicon segments etched onto a SOI wafer. The effective refractive index of the mode is gradually changed by linearly changing the grating period from 400nm at the silicon waveguide edge to200nm at the fiber interface. The width of the waveguide also is tapered from 350 nm to 450 nm simultaneously.

Measuring the fabricated device, the total fiber to waveguide insertion loss was measured to be −0.9dB for TE and−1.2dB for TM polarizations. This is a very promising efficiency with minimal wavelength and polarization dependence over only 50 um length. Although in this experiment e-beam lithography has been used and also the waveguide is only coupled to a lensed fiber with MFD of 2 um.

5.6.4. Buried Silica as the Low Index Waveguide

In 2007, Galan et al suggest a novel approach that not only does not require e-beam lithography but also exempt the need for extra polymer cladding to realize a low index waveguide polarization [150]. He suggests using the buried silica in standard SOI wafers as the ultimate low index core at the coupling edge. He suggests the low index difference of air and silica will confine light in 3 um thick buried silica layer at the fiber front while having the mode expanded enough to couple to optical fiber. In this design the silica at the coupling edge has a width of 8 um and the silicon core is tapered down from 500 nm to a taper tip of 200 um which can be realized by UV lithography. The schematic of the proposed structure is depicted in Fig.5.12.

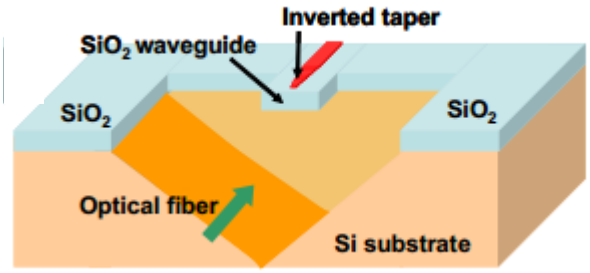

Fig. 5.12. Schematic of the device proposed by Galan for edge coupling. (Copyright Optical Society of America 2007, reproduced with permission after reference [150])

Using FimmWave the modes at two ends of the taper have been studied. Below are the results of FDM calculations. As can be seen at the silicon waveguide end, the mode is strongly confined in the high index core but as the taper tip becomes narrower, the mode moves down to the silica layer and expands up.

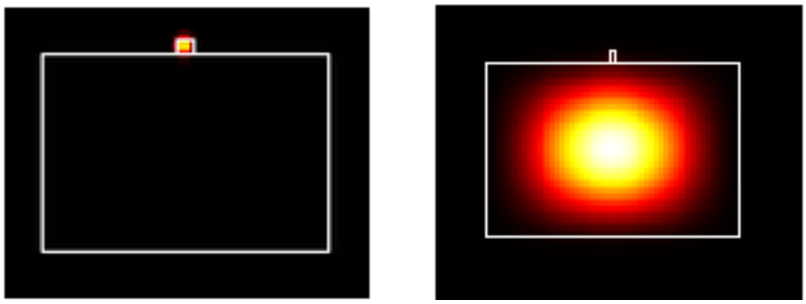

Fig. 5.13. Mode profiles of the taper at the silicon waveguide end (left) and at the fiber interface (right), simulated by Fimmwave.

Also using EME calculations to study the light propagation in such design, following scattering matrix is obtained.

$$\begin{bmatrix} TE_{in} \\ TM_{in} \end{bmatrix} = \begin{bmatrix} 0 & 0.55 \\ 0.58 & 0 \end{bmatrix} \times \begin{bmatrix} TE_{out} \\ TM_{out} \end{bmatrix}$$

Which corresponds to -2.3 dB for TE and -2.6 dB for TM polarizations. Although at first glance this value seems to be higher than other proposed methods, but it must be taken into consideration that here the device is assumed to be coupled to a standard single mode fiber with a MFD of 8 um which is compatible with current telecommunication systems.

Having discussed the most promising approaches towards edge coupling fibers to SOI chips, table below well-illustrates the main properties of each approach making it simpler to compare methods together.

Table 5.1. Different edge coupling methods and their properties.

Source	Architecture	Implementation	Length (um)	Taper tip (nm)	Insertion Loss (dB)	Fiber MFD (um)	Lithography
Shoji[140]	Polymer waveguide at fiber interface	Fabrication	> 200	60	3.5 TE	4.3 um	e-Beam
Baets[143]	Spacer layer btw core and polymer	Fabrication	> 175	175	1.9 TE	5 um	UV
Galan[150]	Buried silica as the low index waveguide	BPM	> 400	200	3.5 TE 3.7 TM	8 um	UV
Pu[147]	tiny taper end by thermal oxidization	Fabrication	> 300	12	2.03 TM 2.6 TE	2.9 um	e-Beam
Cheben[148]	sub-wavelength gratings	Fabrication	>50	350	0.9 TE 1.2 TM	4 um	e-Beam

As can be deducted from the table the structure proposed by Galan has two main advantages comparing to other methods. First is that the structure can easily be realized by standard UV lithography and the second one is that it has reasonable loss for both polarizations when coupling to a standard fiber which in overall makes this structure promising for use in standard optical communication systems. However silica layer hanging in air in the grooved section might be considered as fragile when simply butt coupled to fiber.

Here we suggest another approach to exploit this structure. Considering the tip of the structure hanging on air, it is proposed to have this part embedded in a fiber that has hollow core at the beginning accordingly. In this case the hanging tip of the chip will be protected from external effects and makes a more stable platform. In the meanwhile it is

possible to exploit the advantages this structure brings as discussed earlier. This platform schematically is shown in Fig.5.14:

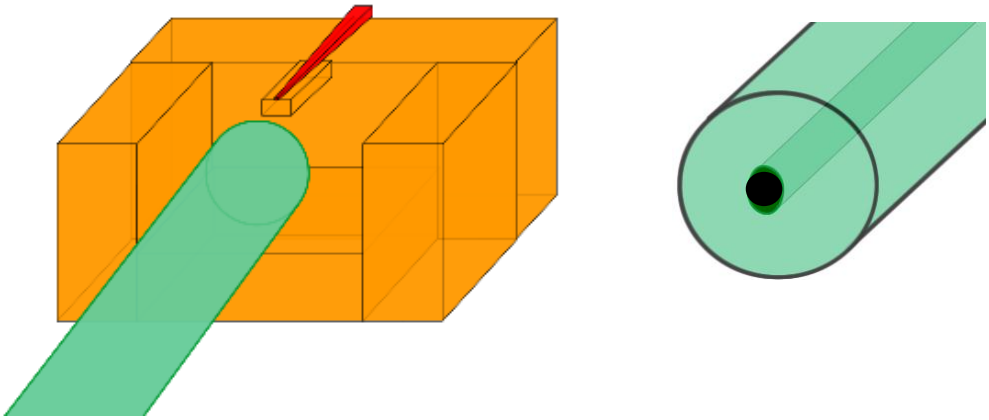

Fig. 5.14. Platform proposed for edge coupling a fiber with a hole at the tip (right) and Galan's proposed structure.

5.7. Summary

In this chapter coupling light from optical fibers to silicon planar waveguides was discussed. Because of the huge mismatch of the geometries of these two types of light carriers, coupling light between them for sake of developing silicon photonics for communication systems is a considerable issue. Here different approaches towards solving this problem and enhancing coupling losses were discussed and a critical appraisal of reviewed methods was offered. At the end, the most promising structure in regards of fabrication complexity and coupling efficiency was pointed out to be Galan's design which used buried silica in SOI wafers as the low index waveguide at the fiber interface. At the end a novel approach towards exploiting this structure was demonstrated offering low coupling efficiency, compatibility with other standard devices and easement of usage.

Chapter 6. Conclusion

6.1. Summary and Conclusion

In this thesis several concerns in integrated photonics which are considered as obstacles towards wide-spread use of this technology in every-day optical communications were discussed. Simulation tools and their limitations to face different problems in nowadays expanded integrated photonic technology was one of these concerns. Photonic crystals in both resonant and non-resonant regimes are specifically challenging problems in this regards due to very fine structural details which cause difficulties for simulation; Either the tool cannot develop an accurate enough result or in some cases any result, or the processing time is more than tolerable. In this regard analytical approach and homogenization methods are proposed for both regimes that a photonic crystal can perform which by simplifying the detailed structure allow faster and more accurate analysis. The structures under study are all chosen from different components in integrated photonics; lamellar gratings as grating couplers, metamaterials for Lüneburg Lens and Bragg gratings in LC-DFB laser structures. In all cases the results from homogenization method was in excellent agreement with the results from numerical methods.

On the other hand, integrating and nano-scaling photonic components on a single chip to increase the yield and lower the costs of their fabrication is an important issue to be able to consider the photonic technology a good substituent to their counterparts in electronic regime; However this miniaturization brings several other issues that must be addressed. Two of the most important issues are polarization management and fiber-to-chip coupling that was discussed in this thesis. A critical appraisal on recent advancements on both fields was offered along with reproduction of most promising proposed structures and also correction of some inaccuracies in literature. In polarization management front, stepped waveguide approach was introduced to be the most efficient structure and designs based on this approach in different substrates were reviewed. In case of fiber-to-

chip coupling, comparison of different methods led to introducing the most promising approach and also a novel platform for exploiting the design was proposed. This platform consists of the buried silica in the SOI wafer as the edge coupler with a tip hanging on air and a fiber with a hollow core at the tip to sit on a groove and enfolding the silica tip. This platform allows for edge coupling a SOI waveguide to a SMF freely sat on a groove etched for this purpose with minimal insertion loss for both polarizations, 2.3 for TE and 2.1 for TM.

The new methods and approaches proposed in this thesis along with the critical appraisals of methods already in literature can be exploited to develop more efficient and easily fabricated integrated systems based on photonic technology which at the end makes this technology suitable and also affordable for mass production and wide spread use in every day communications.

6.2. Future Work

The methods and approaches discussed in this thesis have proved encouraging for future work. Some possible directions of where the continuation of this research might involve are as follows:

1. Simulations of the coupling structure proposed by Galan [150] showed very encouraging results and combined with the proposed platform in this thesis, would make an efficient fiber-to-chip structure. In spite of the fact that through the design, considerations have been taken to reduce fabrication challenges but fabrication of such structure of course will have its own difficulties to be addressed. Hence fabrication of the proposed component is of course on of the priorities to prove the functionality of the proposed structure.
2. Since the stepped waveguide approach towards polarization rotation has proved to be promising in silicon and III-V substrate, it is desired to see if this approach can be exploited in other substrates to work along other components. For example VOA (variable optical attenuators) fabricated in silica-on-silicon substrates suffer from a huge insertion loss in very attenuated states which is contributed mostly by polarization dependent loss (PDL).Hence it is desirable to exploit the stepped

waveguide approach to realize polarization management components in such low refractive index substrates. The challenge in this kind of substrates is that because of the low refractive index, the birefringence required for polarization rotation must be induced externally.

3. In case of homogenization of gratings in a LC-DFB laser, although in a third order Bragg gratings there are rays diffracted in other directions than forward and backward, in the method proposed here they have been assumed negligible. It is desired to map this power loss due to these unwanted diffractions called Streifer's effect to the matrix definitions of the system so that by calculating T matrix or S matrix of the device, optical loss due to this effect can be estimated along with other data discussed in this thesis, and hence more accurate information can be obtained.

References

[1] K. C. Kao and G. A. Hockham, “Dielectric-fiber surface waveguides for optical frequencies,”Proc. IEE, vol. 113, pp. 1151–1158, 1966

[2] W. A. Gambling, “The Rise and Rise of Optical Fibers,” IEEE J. Sel. Topics in Quantum Electron., vol. 6, pp. 1084–1093, 2000

[3] G.J. Parker, M.D.B. Charlton: Photonic crystals, Phys. World13, 29 (2000)

[4] R. Dingle :proc. 13th Int’l Conf, on Physics of Semiconductor .F.G. Fumi (ed.) (North Holland. Amsterdam 1976

[5] A.F. Harvey. Periodic and Guiding Structures at Microwave Frequencies. IEEE Transactions on Microwave Theory and Techniques, 8(1):30–61, January 1960

[6] Heinz Raether. Surface plasmons on smooth and rough surfaces and on gratings, Volume 111. Springer, 1988

[7] C. Pollock and M. Lipson, Integrated Photonics. Springer, 2003

[8] B. Jalali, M. Paniccia, and G. Reed, “Silicon Photonics,” IEEE Microwave Magazine, 2006

[9] K. Uomi, S. Sasaki, T. Tsuchiya, H. Nakano, and N. Chinoe, “Ultralow Chirp and High-speed 1.55μm Multiquantum Wellλ4-Shifted DFB Lasers, ”IEEE Photon. Technol. Lett., vol. 2, pp. 229–230, 1990

[10] B. Jalali and S. Fathpour, “Silicon Photonics,” IEEE J. Lightw. Technol., vol. 24, pp. 4600–4615, 2006

[11] R. Soref, “The past, present, and future of silicon photonics," IEEE Journal of Selected Topics in Quantum Electronics, vol. 12, no. 6, pp. 1678-1687, 2006

[12] M. Paniccia and N. Photonics, “Integrating silicon photonics," Nature Photonics, vol. 4, pp. 498-499, Aug. 2010

[13] W. N. Ye and Y. Xiong, “Review of silicon photonics: history and recent advances," Journal of Modern Optics, vol. 60, pp. 1299-1320, Sept. 2013

[14] W. Bogaerts, R. Baets, and P. Dumon, “Nanophotonic waveguides in silicon-oninsulator fabricated with CMOS technology," Journal of Lightwave Technology, vol. 23, no. 1, pp. 401-412, 2005

[15] A. Densmore, D. Xu, P. Waldron, S. Janz, P. Cheben, J. Lapointe, A. Delage, B. Lamontagne, J. H. Schmid, and E. Post, \A silicon-on-insulator photonic wire based evanescent field sensor," IEEE Photonics Technology Letters, vol. 18, no. 23, pp. 2520-2522, 2006

[16] F. P. Payne and J. P. R. Lacey, "A theoretical analysis of scattering loss from planar optical waveguides, "Opt. and Quant. Electron. 26, 977-986 (1994)

[17] R. Pafchek, R. Tummidi, J. Li, M. A. Webster, E. Chen and T. L. Koch, "Low-loss silicon-on-insulator shallow-ridge TE and TM waveguides formed using thermal oxidation," Appl. Opt. 48, 958-963 (2009)

[18] F. Grillot, L. Vivien, S. Laval, D. Pascal and E. Cassan, "Size influence on the propagation loss induced by sidewall roughness in ultrasmall SOI waveguides," IEEE Photon. Technol. Lett. 16, 1661-1663 (2004)

[19] J. H. Schmid, A. Delâge, B. Lamontagne, J. Lapointe, S. Janz, P. Cheben, A. Densmore, P. Waldron, D.-X. Xu and K.-P. Yap, "Interference effect in scattering loss of high-index-contrast planar waveguides caused by boundary reflections," Opt. Lett. 33, 1479-1481 (2008)

[20] T. G. Nguyen, R. S. Tummidi, T. L. Koch and A. Mitchell, "Lateral leakage of TM-like mode in thin ridge Silicon-on-Insulator bent waveguides and ring resonators," Opt. Express 18, 7243-7252 (2010)

[21] J. D. Joannopoulos, S. G. Johnson, J. N. Winn, and R. D. Meade, Photonic Crystals: Molding the Flow of Light. Princeton University Press, 2 ed., 2008

[22] D. Leuenberger, Experimental and numerical investigation of two-dimensional photonic crystals applications in integrated optics. PhD thesis, Ecole Polytechnique Fédérale de Lausanne (EPFL), 2004

[23] D. Prather, S. Shi, J. Murakowski, G. Schneider, A. Sharkawy, C. Chen, and B. Miao, "Photonic crystal structures and applications: Perspective, overview, and development ,"IEEE J. Sel. Top. Quant. Electron., vol. 12, pp. 1416 –1437, 2006

[24] V. P. Bykov, "Spontaneous emission in a periodic structure," Soviet Journal of Experimental and Theoretical Physics, vol. 35, pp. 269–273, 1972

[25] Corning. (2011, July) Corning SMF-28e+ Optical Fiber. [Online].

http://www.corning.com/WorkArea/showcontent.aspx?id=40723

[26] D. Dai, L. Liu, S. Gao, D.-X. Xu, and S. He, "Polarization management for silicon photonic integrated circuits," Laser and Photonics Reviews, vol. 7, pp. 303-328, May 2013

[27] D. Gallagher, Photonic Cad matures, IEEE LEOS Newsletter, 8-14, February 2008

[28] Van Roey, J., J. van der Donk, and P. E. Lagasse. 'Beam-Propagation Method: Analysis And Assessment'. Journal of the Optical Society of America 71.7 (1981): 803.

[29] D. F.G. Gallagher, T. P. Felici, 'Eigenmode Expansion Methods for Simulation ofOptical Propagation in Photonics - Pros and Cons', Photonics West, San Jose, 2003, Proc. SPIE, 4987, 2003, art. 4987-10, pp. 69-82

[30] I. Tsukerman, 'Computational Methods for Nanoscale Applications : Particles, Plasmons and Waves', (Springer, 2008).

[31] Strang, Gilbert, and George J Fix. An Analysis Of The Finite Element Method. Englewood Cliffs, N.J.: Prentice-Hall, 1973.

[32] J. W. S. Rayleigh (1888), "On the remarkable phenomenon of crystalline reflexion described by Prof. Stokes" (PDF), *Phil. Mag* 26: 256–265,doi:10.1080/14786448808628259

[33] E. Yablonovitch (1987), "Inhibited Spontaneous Emission in Solid-State Physics and Electronics" (PDF), *Physical Review Letters* 58 (20): 2059–2062.

[34] S. John, "Strong Localization of Photons in Certain Disordered Dielectric Superlattices," Phys. Rev. Lett. 58, 2486 (1987)

[35] G. Floquet, *Ann. Sci. Ecole Norm. Sup.* , 12 : 2 (1883) pp. 47–88

[36] Felix Bloch (1928). "Über die Quantenmechanik der Elektronen in Kristallgittern". *Z.* Physik 52: 555–600

[37] E. Yablonovitch, "Photonic Crystals: Semiconductors of Light," *Scientific American*, vol. 285, no. 6, pp. 47-55, Dec. 2001.

[38] Tuck C. Choy, 'Effective Medium Theory: Principles and Applications', (Oxford University Press,1999).

[39] Mishra, Subodha, and S. Satpathy. 'One-Dimensional Photonic Crystal: The Kronig-Penney Model'. *Physical Review B* 68.4 (2003): n. pag. Web. 24 June 2015.

[40] Yeh, Pochi, Amnon Yariv, and Chi-Shain Hong. 'Electromagnetic Propagation In Periodic Stratified Media I General Theory'. *J. Opt. Soc. Am.* 67.4 (1977): 423. Web.

[41] R. M. Walser (2001), "Electromagnetic metamaterials,"Proc. SPIE 4467, 1-15.

[42] 'Metamaterials: Characteristics, Process and Applications'. *Research India Publications* 4.ISSN 2231-1297 (2014): 97-106.

[43] Y. Jiao, S. Fan, and D. A. B. Miller, "Designing for beam propagation in periodic and nonperiodic photonicnanostructures: Extended Hamiltonian method," Phys. Rev. E70,036612 (2004)

[44] P. S. J. Russel, and T. A. Birks, “Hamiltonian optics of nonuniform photonic crystals,” J. Lightwave Technol.17,1982–1988 (1999). [13]4 eg

[45] J. B. Pendry, D. Schurig, and D. R. Smith, “Controlling electromagnetic fields,” Science312,1780–1782 (2006)

[46] J. Valentine, J. Li, T. Zentgraf, G. Bartal, and X. Zhang, “An optical cloak made of dielectrics,” Nat. Mater.8,568 (2009)

[47] D. H. Spadoti, L. H. Gabrielli, C. B. Poitras, and M. Lipson, “Focusing light in a curved-space,” Opt. Express18,3181–3186 (2010)

[48] B. Vasi´ c, G. Isi´ c, R. Gaji´ c, and K. Hingerl, “Controlling electromagnetic fields with graded photonic crystals inmetamaterial regime,” Opt. Express18,20321–20333 (2010)

[49] J. E. Eaton,An Extension of the Lüneburg–Type Lenses(Rep. No. 4110, Naval Res. Lab., 1953

[50] R. K. L¨ uneburg,Mathematical Theory of Optics(Brown U. P., 1944)

[51] A. Vakil, and N. Engheta, “Transformation optics using graphene,” Science332,1291–1294 (2011).

[52] J. D. Joannopoulos, S. G. Johnson, J. N. Winn, and R. D. Meade,Photonic Crystals: Molding the Flow of Light,(2nd ed.) (Princeton U. P., 2008)

[53] X. Chen, T. M. Grzegorczyk, B. I. Wu, J. Pacheco Jr, and J. A. Kong, “Robust method to retrieve the constitutiveeffective parameters of metamaterials,” Phys. Rev. E70,016608 (2004)

[54] T. F. Krauss, R. M. De La Rue, and S. Brand, Nature (London) 383,699 (996)

[55] H. Benisty, C. Weisbuch, D. Labilloy, M. Rattier, C. J. M. Smith, T. F.Krauss, R. M. De la Rue, R. Houdre´, U. Oesterle, C. Jouanin, and D.Cassagne, J. Lightwave Technol.17, 2063 (1999)

[56] M. Qiu, K. Azizi, A. Karlsson, M. Swillo, and B. Jaskorzynska, Phys. Rev. B64, 155113 (2001)

[57] S. Olivier, H. Benisty, M. Rattier, C. Weisbuch, M. Qiu, A. Karlsson, C. J.M. Smith, R. Houdre´, and U. Oesterle, Appl. Phys. Lett. 79, 2514 (2001)

[58] Qiu, Min. 'Effective Index Method For Heterostructure-Slab-Waveguide-Based Two-Dimensional Photonic Crystals'. Applied Physics Letters 81.7 (2002): 1163. Web. 24 June 2015.

[59] Gao, Hanhong et al. 'Design Of Thin–Film Photonic Metamaterial Lüneburg Lens Using Analytical Approach'. Opt. Express 20.2 (2012): 1617. Web.

[60] H. Nikkhah, ‘Optical Switch on a Chip: The Talbot Effect, Lüneburg Lenses & Metamaterials’,Thesis, University of Ottawa, Canada, 2013.

[61] W.H. Bragg and W.L. Bragg, X-rays and crystal structure, G. Bell, London, UK, 1915.

[62] R. Millett, 'Modeling, Fabrication and Measurement of Laterally-Coupled Distributed Feedback Lasers',Thesis, University of Ottawa, Canada, 2009.

[63] L.M. Miller, J.T. Verdeyen, J.J. Coleman, R.P. Bryan, J.J. Alwan, K.J. Beernink, J.S. Hughes, and T.M. Cockerill, "A Distributed Feedback Ridge Waveguide Quantum Well Heterostructure Laser," IEEE Photon. Tech. Lett., vol. 3, pp. 6-8, Jan. 1991.

[64] J. Wiedmann, H.-C. Kim, K. Ebihara, B. Chen, M. Ohta, S. Tamura, J.-I. Shim, and S. Arai, "GaInAsP/InP Distributed Reflector Lasers Consisting of Deeply Etched Vertical Gratings," Jpn. J. Appl. Phys., vol. 40, pp. 6845-6851, Dec. 2001.

[65] S. Li, G. Witjaksono, S. Macomber, and D. Botez, "Analysis of surface -emitting second-order distributed feedback lasers with a central grating phaseshift," IEEE J. Quantum Electron., vol. 9, pp. 1153-1165, Sept./Oct. 2003.

[66] T. Makino, "Threshold Condition of DFB Semiconductor Lasers by the LocalNormal-Mode Transfer Matrix Method: Correspondence to the Coupled-Wave Method," J. Lightwave Technol., vol. 12, pp. 2092-2099, Dec. 1994

[67] A.J. Lowery, "Transmission-line modeling of semiconductor lasers: The transmission-line laser model," Int. J. Numerical Model., vol. 2, pp. 249-265, 1989.

[68] A.M. Shams-Zadeh-Amiri, J.Hong, X. Li, and W.-P. Huang, "Second- and Higher Order Resonant Gratings with Gain or Loss-Part I: Green‟s Function Analysis," IEEE J. Quantum Electron., vol. 36, pp. 1421-1430, 2000

[69] H. Kogelnik and C.V. Shank, "Coupled-Wave Theory of Distributed Feedback Lasers," J. Appl. Phys., vol. 43, pp. 2327-2335, May 1972.

[70] Yariv, A. 'Coupled-Mode Theory For Guided-Wave Optics'. *IEEE J. Quantum Electron.* 9.9 (1973): 919-933. Web.

[71] Streifer, W., D. Scifres, and R. Burnham. 'Coupled Wave Analysis Of DFB And DBR Lasers'. *IEEE J. Quantum Electron.* 13.4 (1977): 134-141. Web.

[72] Adachi, Sadao. 'Refractive Indices Of III–V Compounds: Key Properties Of InGaAsP Relevant To Device Design'. *J. Appl. Phys.* 53.8 (1982): 5863. Web. 6 July 2015.

[73] Broberg, B., and S. Lindgren. 'Refractive Index Of In1−Xgaxasyp1−Y Layers And Inp In The Transparent Wavelength Region'. *J. Appl. Phys.* 55.9 (1984): 3376. Web.

[74] Weber, J.-P. 'Optimization Of The Carrier-Induced Effective Index Change In Ingaasp Waveguides-Application To Tunable Bragg Filters'. *IEEE J. Quantum Electron.* 30.8 (1994): 1801-1816. Web.

[75] Cao, Qing, Philippe Lalanne, and Jean-Paul Hugonin. 'Stable And Efficient Bloch-Mode Computational Method For One-Dimensional Grating Waveguides'. *J. Opt. Soc. Am. A* 19.2 (2002): 335. Web.

[76] Purnawirman, J Sun, T N Adam, G Leake, D Coolbaugh, J D B Bradley, E Shah Hosseini, and M R Watts. C- and L-band erbium-doped waveguide lasers withwafer-scale silicon nitride cavities. Optics letters, 38(11):1760, 2013.

[77] M R Watts, W A Zortman, D C Trotter, R W Young, and A L Lentine.Vertical junction silicon microdisk modulators and switches. Optics Express,19(22):21989-22003, October 2011.

[78] M A Popovid, T Barwicz, M R Watts, P T Rakich, L Socci, E P Ippen, F XKdrtner, and H I Smith. Multistage high-order microring-resonator add-dropfilters. Optics letters, 31(17):2571-2573, July 2006.

[79] D. Dai, L. Liu, S. Gao, D.-X. Xu, and S. He, \Polarization management for siliconphotonic integrated circuits," Laser and Photonics Reviews, vol. 7, pp. 303-328,May 2013.

[80] H. Fukuda, K. Yamada, T. Tsuchizawa, T. Watanabe, H. Shinojima, and S. Itabashi, Opt. Exp. 16, 4872 (2008)

[81] T. Barwicz, M. Watts, M. Popovic, P. Rakich, L. Socci,F. Kartner, E. Ippen, and H. Smith, Nature Photon. 1, 57(2007)

[82] T. Barwicz, M. R. Watts, M. A. Popovic, P. T. Rakich, L. Socci, F. X. Kartner,E. P. Ippen, and H. I. Smith,"Polarization-transparent microphotonic devices in the strong confinement limit," Nature Photonics, vol. 1, pp. 57-60, Jan. 2007.

[83] R. C. Alferness, \Guided-wave devices for optical communication (invited paper),"IEEE J. Quantum Electron., vol. QE-17, no. 6, pp. 946{959, June 1981.

[84] R. C. Alferness and L. L. Buhl, "Waveguide electro-optic polarization transformer,"Appl. Phys. Lett., vol. 38, no. 9, pp. 655-657, May 1981.

[85] K. Yamanouchi, K. Higuchi, and K. Shibayama, "TE-TM mode conversion by interaction between elastic surface waves and a laser beam on a metal-di®used opticalwaveguide," Appl. Phys. Lett., vol. 28, no. 2, pp. 75-77, Jan. 1976.

[86] K. Yamanouchi, K. Wakazono, and K. Shibayama, "Optical surface wave mode converters and modulators utilizing static strain-optical effects," IEEE J. Quantum Electron., vol. QE-16, no. 6, pp. 628-634, June 1980.

[87] H. Deng, 'Design and Characterization of Silicon on Isolator Passive Polarization Converter with Finite-Element Analysis', Thesis, University of Waterloo, Canada, 2005.

[88] H. Zhang, S. Das, Y. Huang, C. Li, S. Chen, H. Zhou, M. Yu, P. Guo-Qiang Lo, and J. T. L. Thong, "Efficient and broadband polarization rotator using horizontal slot waveguide for silicon photonics," Appl. Phys. Lett. 101(2), 021105 (2012).

[89] D. Vermeulen, S. Member, S. Selvaraja, P. Verheyen, P. Absil, W. Bogaerts, D. Van Thourhout, and G. Roelkens, "Silicon-on-insulator polarization rotator based on a symmetry breaking silicon overlay," IEEE Photon. Technol. Lett. 24(6), 482–484 (2012).

[90] Y. Xiong, D.-X. Xu, J. Schmid, P. Cheben, S. Janz, and W. Ye, "Robust silicon waveguide polarization rotator with an amorphous silicon overlayer," IEEE Photonics J. 6(2), 2200308 (2014).

[91] L. Chen, C. R. Doerr, and Y.-K. Chen, "Compact polarization rotator on silicon for polarization-diversified circuits," Opt. Lett. 36(4), 469–471 (2011).

[92] Y. Shani, R. Alferness, T. Koch, U. Koren, M. Oron, B. I. Miller, and M. G. Young,Polarization rotation in asymmetric periodic loaded rib waveguides," Appl. Phys.Lett., vol. 59, no. 11, pp. 1278{1280, Sept. 1991

[93] W.-P. Huang and Z. M. Mao, "Polarization rotation in periodic loaded rib waveguides," J. Lightwave Technol., vol. 10, pp. 1825-1831, Dec. 1992.

[94] S. S. A. Obayya, B. M. Azizur, K. T. V. Grattan, and H. A. ElMikati, IEEE Photon. Technol. Lett. 13, 681(2001).

[95] S. S. A. Obayya, B. M. A. Rahman, K. T. V. Grattan, and H. A. El-Mikati, Appl. Opt. 40, 5395 (2001).

[96] H. Heidrich, P. Albrecht, M. Hamacherm, H.-P. Nolting, H. Schroeter-Janssen, and C. M. Weinert, 'Passive mode converter with a periodically tilted InP/GaInAsP rib waveguide,' IEEE Photon. Technol. Lett. 4, 34-36 (1992).

[97] B. M. Holmes and D. C. Hutchings, IEEE Photon. Technol.Lett. 12, 43 (2006).

[98] D. M. Beggs, M. Midrio, and T. F. Krauss, Opt. Lett. 32,2176 (2007).

[99] M. Fontaine, J. Opt. Soc. Am. B 15, 964 (1998).

[100] Z. Huan, R. Scarmozzino, G. Nagy, J. Steel, and R. M. Osgood, Jr., IEEE Photon. Technol. Lett. 12, 317 (2000).

[101] H. Deng, D. O. Yevick, C. Brooks, and P. E. Jessop, IEEE J.Lightwave Technol. 23, 432 (2005).

[102] Chan, P. S., Tsang, H. K. & Shu, C. Mode conversion and birefringence adjustment by focused-ion-beam etching for slanted rib waveguide walls. *Opt. Lett.* **28**, 2109–2111 (2003).

[103] H. Deng, D. O. Yevick, C. Brooks, and P. E. Jessop, J. Opt.Soc. Am. A 23, 1741 (2006).

[104] C. Brooks, P. E. Jessop, H. Deng, D. O. Yevick, and G. Tarr,Opt. Eng. 45, 044603 (2006).

[105] V. N. Filippov *et al.*, "Measurement of polarisation beat length in single-mode optical fibres with a polarisation modulator", Electron. Lett. 26 (10), 658 (1990)

[106]. H. Deng, D. O. Yevick, C. Brooks, and P. E. Jessop, "Designrules for slanted-angle polarization rotators," J. LightwaveTechnol.23, 432–445 (2005).

[107] Z. Wang and D. Dai, J. Opt. Soc. Am. B 25, 747 (2008)

[108] H. Deng, D. O. Yevick, C. Brooks, and P. E. Jessop, "Design rules for slanted-angle polarization rotators," J. LightwaveTechnol.23, 432–445 (2005)

[109] J. Z. Huang, R. Scarmozzino, G. Nagy, M. J. Steel, and R.M. Osgood, Jr., "Realization of a compact and single-modeoptical passive polarization converter," IEEE Photon. Technol. Lett.12, 317–319 (2000).

[110] D. Correia, J. P. da Silva, and H. E. Hernandez-Figueroa,"Genetic algorithm and finite-element design of shortsingle-section passive polarization converter," IEEEPhoton. Technol. Lett.15, 915–917 (2003)

[111] T. Lu and D. Yevick, "A vectorial boundary element methodanalysis of integrated optical waveguides," J. LightwaveTechnol.21, 1793–1807 (2003).

[112] C. Alonso-Ramos, S. Romero-García, A. Ortega-Moñux, I. MolinaFernández, R. Zhang, H. G. Bach, and M. Schell, 'Polarization rotator for InP rib waveguide', Optics Letters, Vol. 37, pp. 335-337, 2012

[113] R. Kunkel, H. Bach, D. Hoffmann, C. Weinert, I. MolinaFernandez, and R. Halir, inIPRM International Conferenceon Indium Phosphide and Related Materials(IEEE, 2009),pp. 167–170

[114] M. Zaitsu, T. Tanemura, A. Higo, and Yoshiaki, "Experimental demonstration of self-aligned InP/InGaAsP polarization converter for polarization multiplexed photonic integrated circuits", Optics Express, Vol. 21, Issue 6, pp. 6910-6918, 2013

[115] Yunhong Ding, Haiyan Ou, C Optical Fiber Communication ConferencePeucheret, Exposition, and the National Fiber Optic Engineers ConferenceOFC/NFOEC 2013. Wide-band polarization splitter and rotator with large fabrication tolerance and simple fabrication process. Optics letters, 38:1227-1230,2013.

[116] L Liu, Y Ding, K Yvind, and J M Hvam. Silicon-on-insulator polarizationsplitting and rotating device for polarization diversity circuits. Optics Express,19(13):12646--12651, 2011.

[117] Wesley D Sacher, Tymon Barwicz, and Joyce K S Poon. Silicon-on-InsulatorPolarization Splitter-Rotator Based on TM0-TE1 Mode Conversion in a Bi-levelTaper. CLEO, pages 1-2, January 2013.

[118] D Dai and J E Bowers. Novel concept for ultracompact polarization splitterrotator based on silicon nanowires. Optics Express, 19(11):10940--10949, May2011.

[119] Yunhong Ding, Liu Liu, Christophe Peucheret, and Haiyan Ou. Fabricationtolerant polarization splitter and rotator based on a tapered directional coupler.Optics Express, 20(18):20021-20027, August 2012.

[120] Tymon Barwicz, Michael R Watts, Milos A Popovid, Peter T Rakich, LucianoSocci, Franz X Kdrtner, Erich P Ippen, and Henry I Smith. Polarizationtransparent microphotonic devices in the strong confinement limit. Nature Photonics, 1(1):57-60, January 2007.

[121] Y. Xiong, D. Xu, J. Schmid, P. Cheben, S. Janz and W. Ye, 'Fabrication tolerant and broadband polarization splitter and rotator based on a taperetched directional coupler, Opt.Express, vol. 22, , p. 17458, 2014.

[122] G. T. Reed, A. P. Knights, Silicon Photonics, an introduction (John Wiley & Sons, 2004).

[123] H. M. Presby, A. F. Benner, and C. A. Edwards, "Laser micromachining of efficient fiber microlenses," Appl. Opt. 1990, Vol. 29, pp. 2692-2695.

[124] G. Milton, Y. Gharbia, and J. Katupitiya, "Mechanical fabrication of precision microlenses on optical fiber endfaces," Opt. Eng. 2005, Vol. 44, p. 123402.

[125] T. Alder, A. Stohr, R. Heinzelmann, and D. Jager, "High-efficiency fiber-to-chip coupling using low-loss tapered single-mode fiber," IEEE Photon. Technol. Lett. 2000, Vol. 12, pp. 1013-1015.

[126] D. Taillaert, W. Bogaerts, P. Bienstman, T. F. Krauss, P. Van Daele, I. Moerman, S. Verstuyft, K. De Mesel, and R. Baets, "An out-of-plane grating coupler for efficient butt-coupling between compact planar waveguides and single-mode fibers," IEEE J. Quantum Electron. 2002, Vol. 38, pp. 949-955.

[127] F. Van Laere, W. Bogaerts, P. Dumon, G. Roelkens, D. Van Thourhout, and R. Baets, "Focusing polarization diversity grating couplers in silicon-on-insulator," J. Lightwave Technol. 2009, Vol. 27, pp. 612-618.

[128] G. Roelkens, D. Taillaert, F. Van Laere, D. Vermeulen, J. Schrauwen, S. Scheerlinck, T. Claes, W. Bogaerts, P. Dumon, S. Selvaraja, D. Van Thourhout, R. Baets, "Interfacing optical fibers and high refractive index contrast waveguide circuits using diffractive grating couplers," Proc. SPIE. 2009, Vol. 7218, p. 721808.

[129] G. Roelkens, D. Vermeulen, D. Van Thourhout, R. Baets, S. Brison, P. Lyan, P. Gautier, and J.-M. Fedeli, "High efficiency diffractive grating couplers for interfacing a single mode optical fiber with a nanophotonic silicon-on-insulator waveguide circuit," Appl. Phys. Lett. 2008, Vol. 92, p. 131101.

[130] G. Roelkens, D. Van Thourhout, and R. Baets, "High efficiency silicon-on-insulator grating coupler based on a poly-silicon overlay," Opt. Express. 2006, Vol. 14, pp. 11622-11630

[131] A. Melloni, R.Costca , " Waveguide index contrast: implications for passive integrated optical components", Fibres and Optical Passive Components, 2005
[132] D. X. Dai, S. L. He, and H.-K. Tsang, "Bilevel mode converter between a silicon nanowire waveguide and a larger waveguide," J. Lightwave Technol. 2006, Vol. 24, pp. 2428-2433

[133] J. K. Doylend, and A. P. Knights, "Design and simulation of an integrated fiber-tochip coupler for silicon-on-insulator waveguides," IEEE J. Sel. Top. Quantum Electron. 2006, Vol. 12, pp. 1363-1370.

[134] V. Nguyen, T. Montalbo, C. Manolatou, A Agarwal, C.-Y. Hong, J. Yasaitis, L. C. Kimerling, and J. Michel, "Silicon-based highly-efficient fiber-to-waveguide coupler for high index contrast systems," Appl. Phys. Lett. 2006, Vol. 88, p. 081112

[135] K. Shiraishi, H. Yoda, A. Oshima, H. Ikedo, and C. S. Tsai, "A silicon-based spotsize converter between single mode fibers and Si-wire waveguides using cascaded tapers," Appl. Phys. Lett. 2007, Vol. 91, p. 141120.

[136] T. Shoji, T. Tsuchizawa, T. Watanabe, K. Yamada, and H. Morita, "Low loss mode size converter from 0.3 μm square Si wire waveguides to singlemode fibers,"Electron. Lett. 2002, Vol. 38, pp. 1669-1670

[137] V. R. Almeida, R. R. Panepucci, and M. Lipson, "Nanotaper for compact mode conversion," Opt. Lett. 2003, Vol. 28, pp. 1302-1304.

[138] S. J. McNab, N. Moll, and Y. A. Vlasov,"Ultra-low loss photonic integrated circuit with membrane-type photonic crystal waveguides,"Opt Express, vol. 11, no. 22, pp. 2927–2937, Nov. 2003

[139] Y. Shani, C. H. Henry, R. C. Kistler, K. J. Orlowsky, and D. A. Ackerman, "Efficient coupling of a semiconductor laser to an optical fiber by means of a tapered waveguide on silicon," Appl. Phys. Lett. 55(23), 2389–2391 (1989).

[140] T. Shoji, T. Tsuchizawa, T. Watanabe, K. Yamada, and H. Morita,"Spotsize converter for low-loss coupling between 0.3 m square Si wirewaveguides and single modefibers,"inProc. 15th Annu. Meeting IEEE Lasers and Electro-Optics Society, vol. 1, 2002, pp. 289–290

[141] T. Tsuchizawa, K. Yamada, H. Fukuda, T. Watanabe, Jun-ichi Takahashi, M. Takahashi, T. Shoji, E. Tamechika, S. Itabashi, and H. Morita, "Microphotonics Devices Based on Silicon Microfabrication Technology," IEEE J. Sel. Top. Quantum Electron. 11(1), 232–240 (2005).

[142] V. R. Almeida, R. R. Panepucci, and M. Lipson, "Nanotaper for compact mode conversion," Opt. Lett. 28(15), 1302–1304 (2003).

[143] Roelkens, G. et al. 'Efficient Silicon-On-Insulator Fiber Coupler Fabricated Using 248-Nm-Deep UV Lithography'. *IEEE Photonics Technology Letters* 17.12 (2005): 2613-2615.

[144] W.D. Cort, J. Beeckman, R. James, F.A. Fernandez, R. Baets, K. Neyts, Opt. Lett. 34(2009) 2054.

[145] M.A. Foster, A.C. Turner, R. Salem, M. Lipson, A.L. Gaeta, Opt. Express 15 (2007)12949.

[146] T. Xu, N. Zhu, M.Y. Xu, L. Wosinski, J.S. Aitchison, H.E. Ruda, Opt. Express 18 (2010) 5420.

[147] Pu, Minhao et al. 'Ultra-Low-Loss Inverted Taper Coupler For Silicon-On-Insulator Ridge Waveguide'. *Optics Communications* 283.19 (2010): 3678-3682.

[148] Cheben, Pavel et al. 'Refractive Index Engineering With Subwavelength Gratings For Efficient Microphotonic Couplers And Planar Waveguide Multiplexers'. *Optics Letters* 35.15 (2010): 2526.

[149] P. Lalanne and J.-P. Hugonin, "High-order effective-medium theory of subwavelength gratings inclassical mounting: application to volume holograms," J. Opt. Soc. Am. A. 15, 1843-1851 (1998).

[150] Galán, J. V. et al. 'Polarization Insensitive Low-Loss Coupling Technique Between SOI Waveguides And High Mode Field Diameter Single-Mode Fibers'. *Opt. Express* 15.11 (2007): 7058.